EFFECTS OF ELECTRON-PHONON INTERACTION ON THE FLUORESCENCE SPECTRA OF $SrTiO_3:Cr^{3+}$

By

QUIESUP KIM

Bachelor of Science
Seoul National University
Seoul, Korea
1965

Master of Science
University of Oregon
Eugene, Oregon
1970

Submitted to the Faculty of the Graduate College
of the Oklahoma State University
in partial fulfillment of the requirements
for the Degree of
DOCTOR OF PHILOSOPHY
May, 1974

OKLAHOMA
STATE UNIVERSITY
LIBRARY

MAR 13 1975

EFFECTS OF ELECTRON-PHONON INTERACTION ON THE FLUORESCENCE SPECTRA OF $SrTiO_3:Cr^{3+}$

Thesis Approved:

Richard C. Powell
Thesis Adviser

William A. Sibley

George S. Dixon

Timothy M. Wilson

J Paul Devlin

D D Durham
Dean of the Graduate College

902121

ACKNOWLEDGMENTS

The author wishes to express his appreciation to his major advisers, R. C. Powell and T. M. Wilson for their suggestion of the problem and patient guidance throughout this study. Appreciation is also expressed to E. E. Lafon for many valuable discussions on some of the numerical integrals used in this work; to M. Mostoller and R. F. Wood of the Oak Ridge National Laboratory for permission to use the fitting program and helpful discussions and suggestions.

Thanks are also extended to C. T. Butler, S. I. Yun, M. J. Treadaway for their assistance during this work; to H. Hall and the staff of the Chemistry-Physics Machine Shop for the design and fabrication of the apparatus and to Mrs. Janet Sallee and Miss Becky Chapman for their excellence in typing the manuscript.

Finally, special gratitude is expressed to his family for their understanding and many sacrifices.

TABLE OF CONTENTS

Chapter Page

I. INTRODUCTION. 1

II. THEORY. 14

III. EXPERIMENTAL EQUIPMENTS AND SAMPLES 68

IV. RESULTS AND INTERPRETATION--VIBRONIC SPECTRA. 74

V. RESULTS AND INTERPRETATION--ZERO-PHONON LINES AND THE LOCAL MODE. 112

VI. SUMMARY AND CONCLUSIONS 148

REFERENCES. 152

APPENDIX. 156

LIST OF TABLES

Table Page

I. Spacial Symmetry of the Various Points in the Brillouin Zone of $SrTiO_3$ at Room Temperature and Irreducible Representations of the Vibrational Modes of $SrTiO_3$ at Various Points of the Brillouin Zone. 26

II. Modified Part of the Character of Various Operator at the Surface of the Brillouin Zone 28

III. Character Table of O_h and the Vibrational Modes at Γ Point 30

IV. Correlation Among Elements of O_h and Its Subgroup Presented by an Impurity Ion 32

V. Total Representations and Their Reductions on the Surface of the Brillouin Zone 33

VI. Allowed Vibrational Modes From ^2E_g by Electric Dipole Transition $\Gamma_r(T_{1u})$ in Various Point in the Brillouin Zone. 34

VII. Splittings of the Vibrational Modes of Cubic Symmetry Under the Distortion (B_{1u}) into Tetragonal Symmetry . . 37

VIII. Vibrational Modes of $SrTiO_3$ Appearing in Spectra of Vibronic, Infrared Absorption and Raman Spectra, and Neutron Scattering (Unit eV x 10^{-2}). 77

IX. Vibrational Normal Modes at 297°K for the Principal Symmetry Points Determined From Neutron Scattering and By a Rigid Shell Model 83

X. Low Frequency Vibrational Modes (eV From Zero-Phonon Lines) of Strontium Titanate. 107

XI. Widths of the Zero-Phonon Lines of $SrTiO_3:Cr^{3+}$ (0.02% Weight) at Various Temperatures 120

XII. Positions of the Zero-Phonon Lines of $SrTiO_3:Cr^{3+}$ (0.02% Weight) at Various Temperatures 121

LIST OF TABLES (Continued)

Table Page

XIII. Adjustible Parameters for the Fits of the Zero-Phonon Lines Widths and Line Shifts of $SrTiO_3:Cr^{3+}$ (0.02% Weight) 122

XIV. Temperature Dependence of Fluorescence Decay Time of the Zero-Phonon Line of $SrTiO_3:Cr^{3+}$ (0.02% Weight) and Ratio of Integrated Intensity With Respect to That of Total Sideband. 128

XV. Line Widths of the Local Mode in $SrTiO_3:Cr^{3+}$ (0.02% Weight) at Various Temperatures 133

XVI. Line Shifts of the Local Mode in $SrTiO_3:Cr^{3+}$ (0.02% Weight) at Various Temperatures 134

XVII. Ratio of the Integrated Intensity of the Local Mode With Respect to That of Sidebands of $SrTiO_3:Cr^{3+}$ (0.02% Weight) at Various Temperatures 135

XVIII. Adjustible Parameters for Fits of Line Widths and Positions of the Local Mode, and Integrated Ratio of the Local Mode With Respect to Total Sidebands in $SrTiO_3:Cr^{3+}$ (0.02% Weight). 142

LIST OF FIGURES

Figure		Page
1.	Diagrams of Vibronic and Radiative Transitions for Both Absorption (a) and in Emission (b) of Photons	3
2.	Three Types of Profiles Observed in Optical Spectra for Weak (a), Intermediate (b), and Strong (c) Electron-Phonon Interactions.	4
3.	Structure of $SrTiO_3$ in the Cubic Phase Showing Two Complete Unit Cells.	8
4.	Rotation of the Oxygen Octahedra in $SrTiO_3$ Giving Rise to the Cubic to Tetragonal Phase Transition Shown in a Two Dimensional Cross Section Perpendicular to the Tetragonal Axis.	10
5.	Feyman Diagrams of the Vibronic Process	16
6.	Unit Cell (a) and First Brillouin Zone of Strontium Titanate With Five Atoms of Which Coordinates are Sr(0,0,0); Ti(½,½,½); 01(½,0,½); 0_2(1,½,½); and 0_3(½,½,0) and the First Brillouin Zone (b) With the Points of High Symmetry Labeled	24
7.	Flow Chart of the Computer Program Used	63
8.	Block Diagram of the Continuous Fluorescence Measurement Apparatus	69
9.	Response of Luminescence Detection System as a Function of Photon Energy	71
10.	Block Diagram of the Fluorescence Decay Time Measurement Apparatus	72
11.	The Fluorescence Spectrum of $SrTiO_3:Cr^{3+}$ at About 8^oK and 150^oK	75
12.	Low Energy Vibronic Spectra at 8^oK in Comparison With Neutron Scattering Dispersion Curves of $SrTiO_3$ and Raman and Infrared Data	76

LIST OF FIGURES (Continued)

Figure Page

13. Measured and Calculated Broad Band Spectrum Using Huang-Rhys Factor S = 0.766 and an Estimated One-Phonon Spectrum 86

14. The Best Fit Between Observed and Predicted Vibronic Sideband Which was Obtained with α = 350 1/eV and S = 0.300. 89

15. First Nearest Neighbor Atoms of Bromine in Zinc Blende . . . 95

16. Density of Phonon States of the $SrTiO_3$ Calculated From Fitting a Rigid Shell Model to Neutron Scattering Data and Obtained From Vibronic Spectra 99

17. Intensity Change of the Vibronic Sideband Close to the Zero-Phonon Lines at 8°K 103

18. Low Frequency High Energy Vibronic Sidebands of $SrTiO_3:Cr^{3+}$ (0.02% Wt.) at 8°K, 40°K, and 110°K. 105

19. Line Widths of the Zero-Phonon Lines of $SrTiO_3:Cr^{3+}$ (0.02% Weight). 123

20. Line Shifts of the Zero-Phonon Lines of $SrTiO_3:Cr^{3+}$ (0.02% Wt.) 124

21. Temperature Dependence of the Decay Time of Cr^{3+} in $SrTiO_3$ 129

22. Vibronic Spectrum of $SrTiO_3:Cr^{3+}$ (0.02% Weight) in the Region of the Local Mode at 8 and 150°K. 136

23. Temperature Dependence of the Line Width of the Local Mode Vibronic Peak in $SrTiO_3:Cr^{3+}$ (0.02% Weight). 137

24. Temperature Dependence of the Position of the Local Mode Vibronic Peak. 138

25. Temperature Dependence of the Intensity of the Local Mode Vibronic Peak. 139

CHAPTER I

INTRODUCTION

Background

The development of laser action in crystals doped with magnetic ions has brought a great interest to the field of solid state spectroscopy. The knowledge of the energy levels and transitions of a fluorescent system can be expanded by spectroscopic research. Also the presence of lattice vibrations gives rise to temperature dependent effects in the observed spectra. Interpretation of these effects can yield information concerning the interaction of host lattice phonons with the electrons on the impurity ions.

An isolated impurity ion in an excited electronic state can decay by three kinds of processes: (1) radiative decay through an electronic transition giving rise to the emission of a photon; (2) radiationless decay through a vibrational transition giving rise to the emission of phonons; and (3) vibronic decay through a coupled vibrational-electronic transition giving rise to the absorption or emission of a phonon with the emission of a photon. The inverse of the fluorescence decay time of the excited state will be the sum of the decay probabilities of these three processes. Analogous processes occur in the absorption of light by the impurity ion. Electronic transitions provide information on the energy levels of the impurity ion while radiationless and vibronic transitions provide information on the electron-phonon interaction.

Radiative and vibronic transitions can be observed directly in optical spectra whereas radiationless transitions are observed only indirectly through the temperature dependence of spectroscopic data. Figure 1 shows a diagram of vibronic and radiative transitions in both absorption and emission. The radiative transitions give rise to zero-phonon lines in the spectra. Vibronic sidebands will appear on both the low energy and high energy side of these lines. In absorption spectra the low energy vibronics are due to the concurrent absorption of a photon and a phonon whereas in the fluorescence spectra the low energy vibronics are due to the concurrent emission of a photon and a phonon. Similarly, the high energy vibronics in absorption are due to the simultaneous absorption of a photon and emission of a phonon while in the fluorescence spectra they are due to the simultaneous emission of a photon and absorption of a phonon. Thus, the absorption and emission spectra should appear as mirror images on either side of the zero-phonon line. However, since the intensity of these sidebands is proportional to the probability of absorption or emission of phonons, the low energy absorption vibronics and high energy emission vibronics are generally not observed at low temperatures where few phonons are available for absorption.

Three types of spectral profiles can be observed depending on the strength of the electron-phonon interaction: These are shown in Figure 2 for typical fluorescence spectra. For weak electron-phonon interaction most of the emission occurs purely radiatively. This gives rise to a very intense zero-phonon line with a weak, structured vibronic sideband consisting mostly of one-phonon emission transitions. As the strength of the electron-phonon interaction increases more emission occurs in the vibronic sideband and less in the zero-phonon line. The vibronic bands

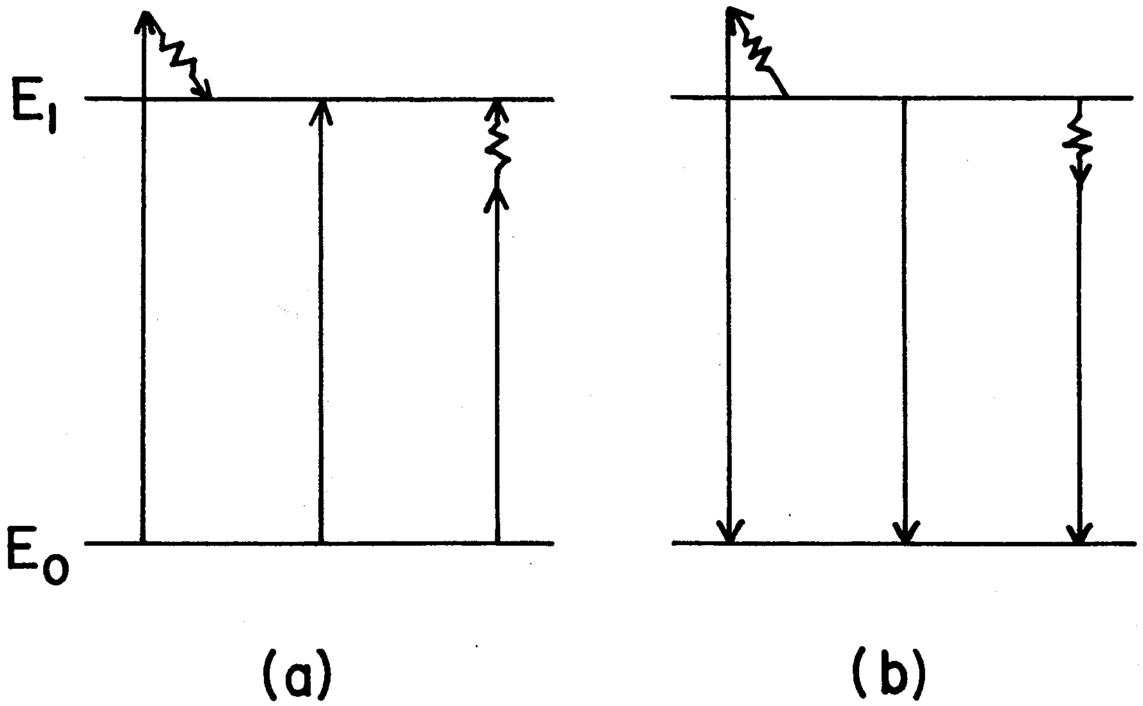

Figure 1. Diagrams of Vibronic and Radiative Transitions for Both Absorption (a) and in Emission (b) of Photons

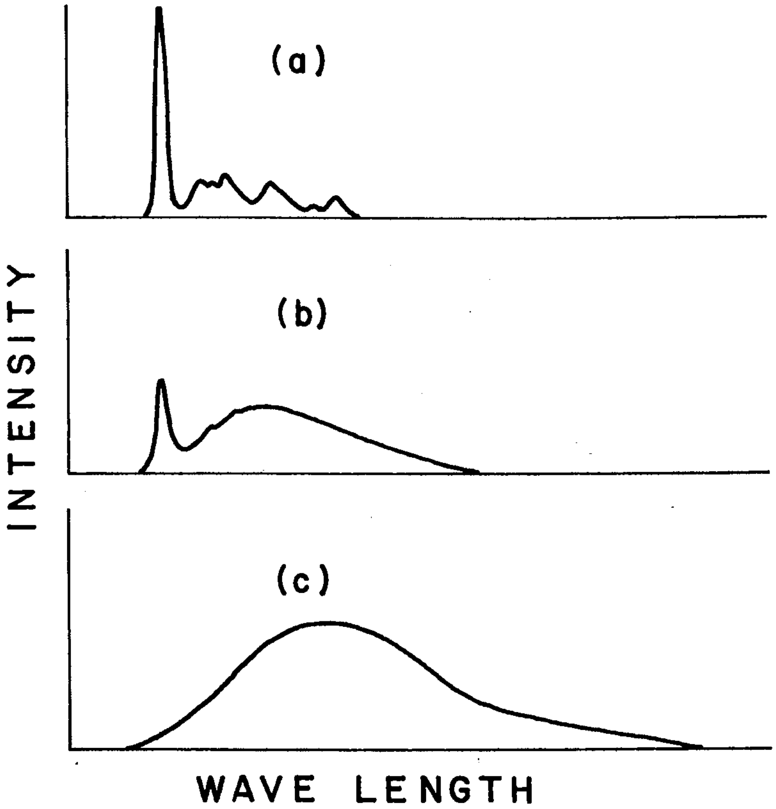

Figure 2. Three Types of Profiles Observed in Optical Spectra for Weak (a), Intermediate (b), and Strong (c) Electron-Phonon Interactions

can be much broader and less structured when multi-phonon transitions are important and in some cases the zero-phonon line is not observed at all. As temperature is increased the relative intensities and shape of the vibronic sidebands change due to the change in the probability of absorbing and emitting phonons. Phonon scattering and radiationless transitions also cause a change in the width and position of the zero-phonon line with temperature.

There are two purposes for studying the spectra of impurities in solids: to characterize and understand the optical properties of the system; and to obtain information on the phonons of the host crystal and how they interact with the electrons on the impurity. This work is concerned mainly with the latter purpose. This information on the lattice dynamics is interesting because of the important roll played by phonons in the thermal, electrical, and optical properties of solids.

The most powerful technique currently used for studying lattice vibrations is neutron scattering. Despite the wealth of information which has been obtained from this technique, it does have some limitations such as the need for expensive equipment, a relatively low resolution, and the fact some materials cannot be investigated because they have a low scattering cross section or high absorption cross section for neutrons. Infrared absorption and Raman and Brillouin light scattering provide complimentary techniques for investigating lattice vibrations. These methods have higher resolution than neutron scattering but first order phonon processes are limited to the center of Brillouin zone by momentum conservation. Second order processes are not subject to this restriction but it is usually quite difficult to unfold the combined density of phonon states. These techniques are also limited by rigorous selection rules.

Perhaps the most attractive feature of vibronic spectroscopy for investigating lattice vibrations is that, compared with the other methods, it is a very simple, inexpensive experimental technique. It also has been shown that information on phonon eigenvectors as well as eigenfrequencies can be obtained from vibronic studies which is not available by other methods (1). Phonons from all parts of the Brillouin zone may be active in vibronic transitions although they are subject to certain selection rules. These phonons can be identified even though it is sometimes quite complicated to do so. One of the major problems in using vibronic spectra is that the presence of an impurity center may perturbe the lattice modes or introduce local vibrational modes which must be distinguished from the normal lattice modes.

It is important to note that the structure observed in vibronic spectra represents an effective phonon distribution (weighted by the electron-phonon interaction) and not the actual phonon density of states of the crystal. This information is useful itself in understanding the absorption and luminescence properties of the systems and how they change with temperature. It is also possible to use this data to obtain information concerning the lattice dynamics of the host crystal. However, this involves determining the frequency dependence of the electron-phonon coupling parameters. Two methods have been used to do this: One is to assume a simple model for the coupling parameters and use the long wavelength limit of their frequency dependence (2). This factor can then be divided out of the measured effective phonon distribution leaving the phonon density of states of the pure crystal. The second method is to formulate from first principles a lattice dynamic model for the crystal with an impurity and from this calculate the predicted shape of the vibronic sidebands (1). This is by far the most elegant technique for interpreting vibronic spectra and using it makes vibronic spectroscopy the most powerful method for studying lattice dynamics. However, this is a very complicated procedure and to avoid the use of many adjustable parameters in the model it is necessary to have a significant amount of other experimental data available on the crystal. In many cases the first, simpler method gives a good approximation to the true phonon density of states. It should be noted that all of the information on lattice phonons is contained in the one-phonon sideband and in both techniques this must first be projected out of the total observed vibronic spectra.

Chromium Doped Strontium Titanate

This thesis deals with measuring the vibronic spectra of chromium doped strontium titanate and interpreting the results in terms of the host lattice phonons and their interaction with the electrons on the impurity atoms. $SrTiO_3$ was chosen as a host crystal because of its interesting structural, acoustical and electrical properties in which the lattice vibrations play an important roll. Chromium was chosen as the impurity ion because it is known to give rise to very distinct, structured vibronic bands.

$SrTiO_3$ is generally considered to have octahedral symmetry at room temperature although x-ray analysis indicates that it is not a perfect cubic perovskite structure (3). It has O_h^1 symmetry with one molecule per unit cell as shown in Figure 3 (4). A second (or higher) order phase transition takes places around $110^{o}K$ and the symmetry becomes tetragonal.

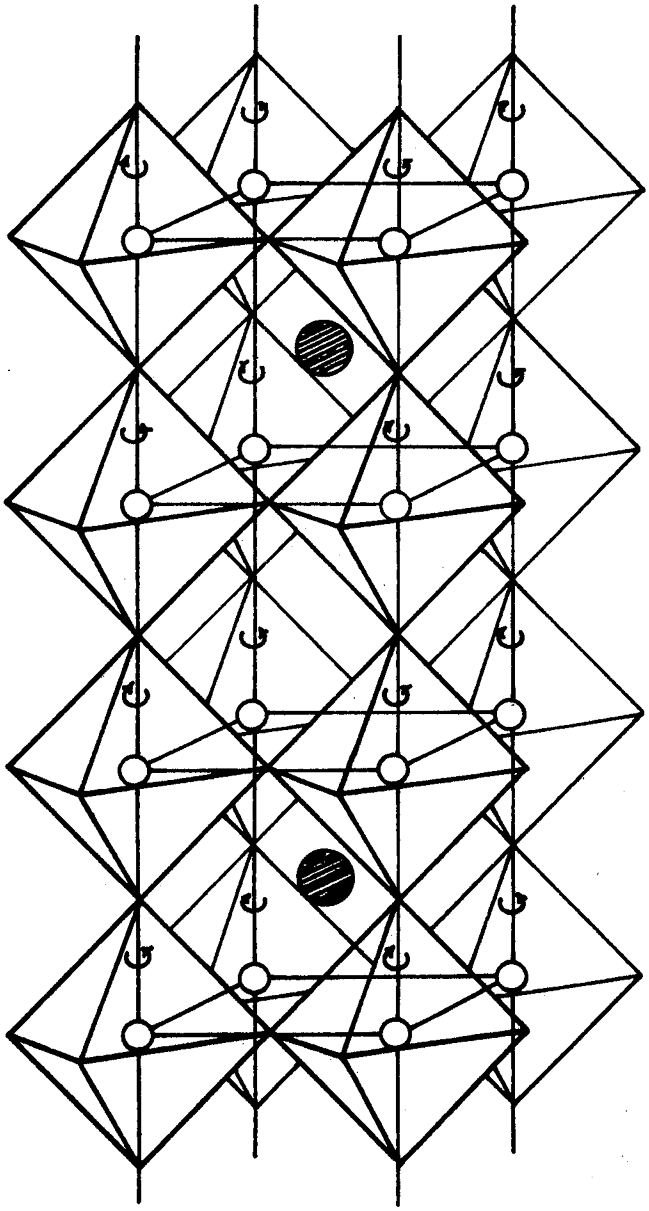

Figure 3. Structure of $SrTiO_3$ in the Cubic Phase Showing Two Complete Unit Cells (4). ▨ ; Ti, ○ ; Sr, and the oxygen atoms are located at the vertices of the octahedra surrounding the titanium atoms.

Below 35°K the symmetry is rhombohedral and there may be an intermediate orthorhombic phase between 65°K and 35°K (3). The 110°K phase transition is thought to be precipitated by the Γ_{25} soft transverse optic mode at the corner (R-point) of the Brillouin zone and the 35°K phase transition is associated with the Γ_{15} soft transverse optic mode at the center of the Brillouin zone (5). Several of the branches of the lowest TO mode in different symmetry directions have been found to be temperature dependent (6,7) and this makes it difficult to compare data on phonon frequencies obtained at different temperatures.

The lattice dynamics of strontium titanate have been extensively investigated both experimentally and theoretically (5-17). The lattice vibration theory of ferroelectricity (18,19) has been successfully applied to strontium titanate even though it never becomes truely ferroelectric. The soft modes have been the subject of numerous studies and have been found to account for most of the interesting acoustical and dielectric properties as well as giving rise to the structural phase transitions.

The phase transitions in $SrTiO_3$ have been investigated by measurements of electron and nuclear magnetic resonance (20,21), ultrasonic attenuation (22), elastic constants (23), dielectric constants (24), x-ray diffraction (3), thermal conductivity (25), piezoresistivity (26), optical birefringence (3), light scattering (5,6,17,27), infrared absorption (8-12), neutron scattering (6.7), and vibronic spectra (28-32). In the current model for the 110°K structural transition the octahedra of oxygen atoms are thought to rotate in alternating directions about the cubic crystal axes. This leads to D_{4h}^{18} symmetry as shown in two dimensions in Figure 4 (21). This doubles the size of the unit cell and causes the

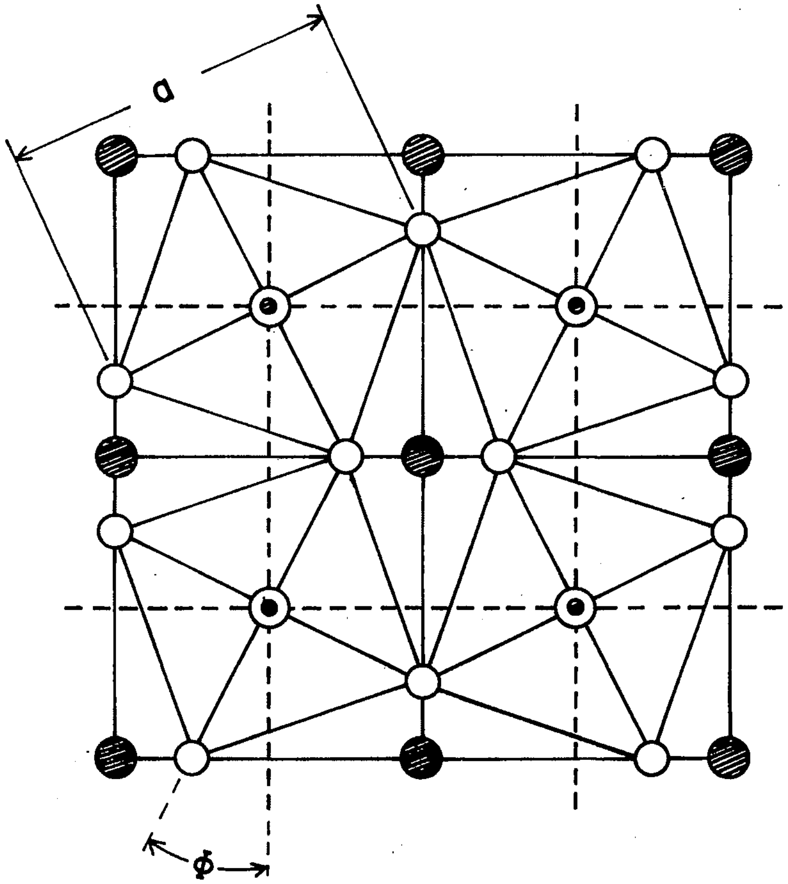

Figure 4. Rotation of the Oxygen Octahedra in $SrTiO_3$ Giving Rise to the Cubic to Tetragonal Phase Transition Shown in a Two Dimensional Cross Section Perpendicular to the Tetragonal Axis (21). ▨; Sr, ⊙; Ti, and ○; O.

R-point of the cubic Brillouin zone to become the new zone center.

Because of size similarities, Cr^{3+} ions probably go into the $SrTiO_3$ lattice substitutionally for Ti^{4+} ions. This requires some charge compensating mechanism such as an oxygen vacancy which probably takes place non-locally since room temperature electron-spin resonance measurements show the chromium ion to occupy a site of cubic symmetry (20). At high temperatures the fluorescence spectrum exhibits a strong zero-phonon line (R-line) arising from a magnetic dipole transition from the ^2E_g excited state to the $^4A_{2g}$ ground state. This is accompanied by weak, structured vibronic sidebands (30). Below 110°K the R-line splits into an R_1, R_2 doublet and more structures are showed up in vibronic sidebands. Another feature which appears in the spectrum is a strong, sharp vibronic peak which cannot be associated with any normal lattice mode of $SrTiO_3$ (30). It does not appear in the spectra of other impurity ions in strontium titanate and thus is attributed to a local vibrational mode induced by the chromium impurities. Since Cr^{3+} is only slightly heavier than Ti^{4+} the local mode is probably induced by force constant changes due to the charge difference and not to mass differences.

Summary of Thesis Work

The continuous fluorescence spectra and the fluorescence decay times of chromium doped strontium titanate were measured at numerous temperatures between about 8°K and 200°K. From this data we obtained the temperature dependence of the vibronic spectra, fluorescence decay time, the widths and positions of the zero-phonon lines, and the width, position, and intensity of the impurity induced local vibrational mode.

The frequency dependence of the low energy vibronic spectra near the zero-phonon lines is found to vary as ω_q^3 which is indicative of an allowed electric dipole transition without the necessity of vibrational induced mixing of states of opposite parity. The vibronic selection rules for phonons at all part of the Brillouin zone were determined and the peaks observed in the vibronic spectra at low temperatures were compared to the results of neutron scattering, Raman scattering, and infrared absorption. Most of the vibronic peaks can be identified and the high energy vibronic sideband was found to be useful in observing the low frequency soft modes of $SrTiO_3$. Using an iteration process, a computer analysis of the data was used to obtain the one-phonon and multiphonon contributions to the observed vibronic sideband. In order to predict a good fit to the observed spectra it is necessary to include quadratic coupling between the local mode and the lattice phonons. The contribution of other multiphonon processes is very small.

The effective phonon distribution reflected by the one-phonon vibronic sideband was used to theoretically predict the temperature dependence of the width and position of the zero-phonon lines and the width, position, and intensity of the local mode. The predictions for both cases do agree fairly well with experimental data. Comparisons are made with the theoretical predictions obtained using a Debye phonon distribution and with predictions involving coupling only to the soft modes. The discrepancies between theory and experiment are discussed in terms of anharmonic interactions and different phonon coupling strengths for different physical processes.

The temperature dependence of the fluorescence decay time is found to compare favorably with the temperature dependence of the ratio of the integrated fluorescence intensity of the zero-phonon line to that of the total spectrum. This implies that the quenching of the decay time at high temperatures is due to the increased probability of radiationless and vibronic processes and not due to the change in the electronic transition probability due to the structural phase transition.

A simple model is assumed for the frequency dependence of the electron-phonon coupling parameters and by dividing this out of the effective phonon distribution obtained from the vibronic spectra an estimate is obtained for the true phonon distribution of the pure crystal. This is compared to the phonon density of states obtained from neutron scattering data and found to agree reasonably well.

CHAPTER II

THEORY

The system we are dealing with consists of the electronic states of the impurity ions, the electromagnetic radiation, and the thermal vibrations of the lattice. The ion interacts with the electromagnetic field by absorbing or emitting photons resulting in transitions to higher or lower electronic states. It interacts with the vibrational field by the absorption or emission of phonons which may or may not result in transitions between the electronic states. Standard second quantization formalism and the semi-classical theory of electromagnetic radiation is used to treat these interactions. In the following sections we derive expression for the vibronic transition rate, the selection rules predicted through symmetry considerations, and the expressions describing the spectral profile.

Derivation of Vibronic Transition Rate

The transition probability per unit time can be predicted in the usual way using Fermi's Golden Rule of time dependent perturbation theory,

$$W = \frac{2\pi}{\hbar} \left|\langle\Psi_f|H_{int}|\Psi_i\rangle\right|^2 \rho_f(E_f = E_i) \ . \tag{1}$$

where Ψ_i and Ψ_f are the wave functions of the initial and final states,

H_{int} is the interaction Hamiltonian causing the transition, and $\rho_f(E_f=E_i)$ is the density of final states. The matrix elements for vibronic transitions can be represented by the diagrams shown in Figure 5. The two interaction verticies in each of these diagrams indicate that H_{int} can be expressed as the sum of the ion-photon interaction H_{int}^{i-e} and the ion-phonon interaction H_{int}^{i-v}.

The Hamiltonian for the total system can be expressed as

$$\begin{aligned} H &= H_{ion} + H_{em} + H_{vib} + H_{int}^{i-e} + H_{int}^{i-v} \\ &= H_o + H_{int}, \end{aligned} \tag{2}$$

where H_{ion} is the Hamiltonian for the ion in a static crystal field, H_{em} and H_{vib} are Hamiltonians for the photon and phonon fields, respectively, and the last two terms are the interaction Hamiltonians of interest here.

Using the semi-classical treatment, the ion-photon interaction Hamiltonian can be expressed in terms of photon creation and annihilation operators in the usual way (33),

$$H_{int}^{i-e} = -\frac{e}{m} \sum_{k,\lambda} \left(\frac{2\pi\hbar}{\omega_{k,\lambda} V}\right)^{\frac{1}{2}} \hat{\pi}_k^{\lambda} \cdot \underline{p} \left(a_k^{\lambda} e^{i\underline{k}\cdot\underline{r}} + a_k^{\lambda+} e^{-i\underline{k}\cdot\underline{r}}\right), \tag{3}$$

where m, $\underline{r}$ and $\underline{p}$ are the mass, position and momentum of an electron, resepctively, and $\underline{k}$ and λ represent the wave vector and polarization of the photon. The operator $a_k^{\lambda+}$ creates a photon of wave vector $\underline{k}$ and polarization λ while a_k^{λ} annihilates such a photon.

The ion-phonon interaction takes place through the modulation of the crystal field at the site of the ion due to the vibration of the surrounding atoms. This can be written as a Taylor's expansion of the

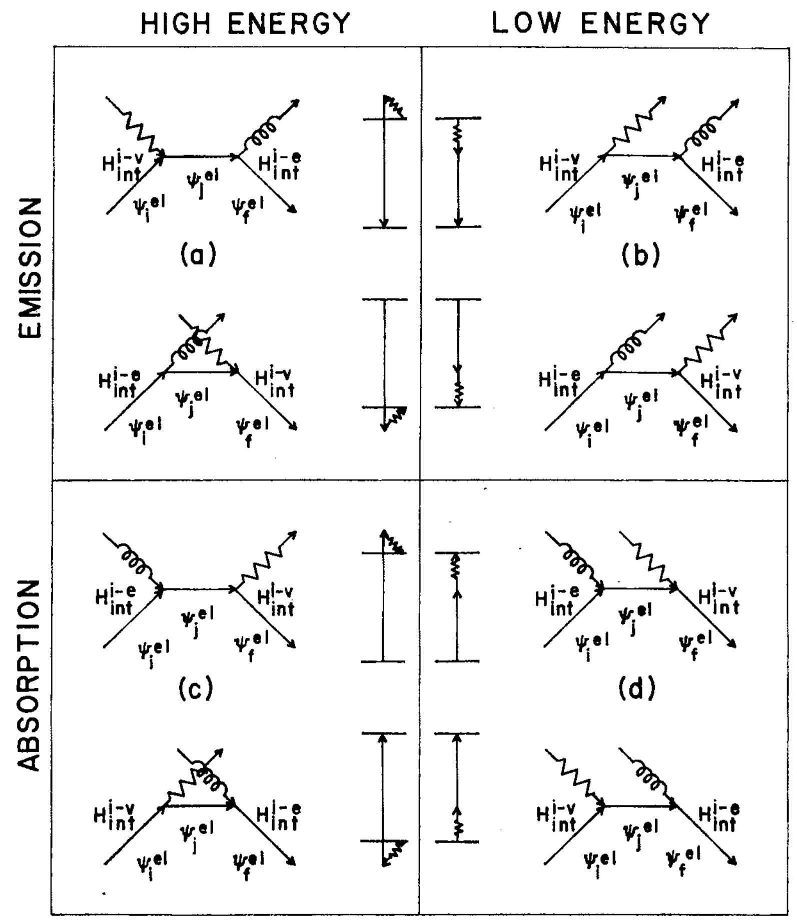
HIGH ENERGY
LOW ENERGY
EMISSION
ABSORPTION
(a)
(b)
(c)
(d)
H^{i-v}_{int}
H^{i-e}_{int}
ψ^{el}_i
ψ^{el}_j
ψ^{el}_f

Figure 5. Feyman Diagrams of the Vibronic Process. The two interaction vertices in each of these diagrams indicate that H_{int} can be expressed as the sum of the ion-photon interaction (H^{i-e}_{int}) and the ion-phonon interaction (H^{i-v}_{int}). → electron; ∿→ photon ($\hbar\omega_k$); and ⋀⋁→ phonon ($h\omega_q$).

crystal field V in terms of the normal coordinates of the lattice vibrations,

$$V = V_o + \sum_{q,\mu} \frac{\partial V}{\partial Q_q{}^\mu}\Bigg|_{Q_q^\mu = o} Q_q^\mu + \frac{1}{2!} \sum_{q\mu q'\mu'} \frac{\partial^2 V}{\partial Q_q^\mu \partial Q_{q'}^{\mu'}}\Bigg|_{\substack{Q_q^\mu = o \\ Q_{q'}^{\mu'} = o}} Q_q{}^\mu Q_{q'}^{\mu'} + \ldots, \tag{4}$$

where Q_q^μ is the normal coordinate for a phonon of wave vector $\underline{q}$ and polarization μ. The normal coordinates can be expressed in terms of creation and annihilation operators as (33)

$$Q_q^\mu = \sqrt{\frac{\hbar}{2\omega_{q\mu}}}\,(b_q{}^\mu + b_{-q}^{\mu +}), \tag{5}$$

where $b_q^{\mu +}$ creates a phonon of wave vector $\underline{q}$ and polarization μ while b_q^μ annihilates a similar phonon. Using this in Equation (4), the first order and second order ion-phonon interaction Hamiltonians can be expressed as

$$H_{int}^{i-v(1)} = \sum_{q,\mu} V_q^\mu \sqrt{\frac{\hbar}{2\omega_{q\mu}}}\,(b_q^\mu - b_q^{\mu +}),$$

$$H_{int}^{i-v(2)} = \frac{\hbar}{2} \sum_{q,\mu} \sum_{q',\mu'} V_q{}^\mu{}_{q'}{}^{\mu'} \frac{1}{\sqrt{\omega_{q\mu}\omega_{q'\mu'}}}\,(b_q^\mu - b_q^{\mu +})(b_{q'}^{\mu'} - b_{q'}^{\mu' +}), \tag{6}$$

where

$$V_q^\mu = \frac{\partial V}{\partial Q_q{}^\mu}\Bigg|_{Q_q^\mu = o},$$

$$V_{q\,q'}^{\mu\,\mu'} = \left.\frac{\partial^2 V}{\partial Q_q^{\mu}\,\partial Q_{q'}^{\mu'}}\right|_{\substack{Q_q^{\mu}=0\\ Q_{q'}^{\mu'}=0}} . \tag{7}$$

Next we need the wave functions for the system. These can be written in second quantized form as

$$|\Psi_i> = |\Psi_i^{el};\ n_1,n_2,\ldots,n_{k\lambda},\ldots;n_1,n_2,\ldots,n_{q\mu},\ldots>,$$

$$|\Psi_f> = |\Psi_f^{el};n_1,n_2,\ldots,n_{k\lambda}\pm 1,\ldots;n_1,n_2,\ldots,n_{q\mu}\pm 1,\ldots>,$$

where Ψ^{el} is the wave function for the electronic state, while $n_{k\lambda}$ and $n_{q\mu}$ represent the occupation numbers for specific photon and phonon states, respectively. By making use of the Born-Oppenheimer approximation these can be written in product form as

$$\begin{aligned}|\Psi_i> &= |\Psi_i^{el}>|n_1>|n_2>\ldots|n_{k\lambda}>\ldots|n_1>|n_2>\ldots|n_{q\mu}>\ldots,\\ |\Psi_f> &= |\Psi_f^{el}>|n_1>|n_2>\ldots|n_{k\lambda}\pm 1>\ldots|n_1>|n_2>\ldots|n_{q\mu}\pm 1>\ldots\ .\end{aligned} \tag{8}$$

Now let us consider the probability per unit time for a specific vibronic transition using the above equations. Since low energy emission vibronics are of greatest interest in this thesis, consider the rate for emission of a photon of wave vector $\underline{k}$ and polarization λ and the concurrent emission of a phonon of wave vector $\underline{q}$ and polarization μ. Substituting Equations (3), (6), and (8) into Equation (1) gives

$$W = \frac{2\pi}{\hbar}\left|\sum_j \frac{<\Psi_f|H_{int}^{i-e} + H_{int}^{i-v}|\Psi_j><\Psi_j|H_{int}^{i-e} + H_{int}^{i-v}|\Psi_i>}{E_i - E_j}\right|^2 \rho_f(E_f = E_i)$$

$$= \frac{2\pi}{\hbar}\Big|\sum_j \frac{\langle \Psi_f^{el};n_{k\lambda}+1;n_{q\mu}+1|H_{int}^{i-e}|\Psi_j^{el};n_{k\lambda};n_{q\mu}+1\rangle\langle\Psi_j^{el};n_{k\lambda};n_{q\mu}+1|H_{int}^{i-v}|\Psi_i^{el};n_{k\lambda};n_{q\mu}\rangle}{E_i^{el}-(E_j^{el}+\hbar\omega_{q\mu})}$$

$$+ \sum_j \frac{\langle \Psi_f^{el};n_{k\lambda}+1;n_{q\mu}+1|H_{int}^{i-v}|\Psi_j^{el};n_{k\lambda}+1;n_{q\mu}\rangle\langle\Psi_j^{el};n_{k\lambda}+1;n_{q\mu}|H_{int}^{i-e}|\Psi_i^{el};n_{k\lambda};n_{q\mu}\rangle}{E_i^{el}-(E_j^{el}+\hbar\omega_{k\lambda})}\Big|^2$$

$$\times\ \rho_f(E_f = E_i)$$

$$= \frac{2\pi}{\hbar}\ \Big|\ \sum_j \frac{\langle \Psi_f^{el};n_{k\lambda}+1|H_{int}^{i-e}|\Psi_j^{el};n_{k\lambda}\rangle\langle\Psi_j^{el}|V_q^{\mu}|\Psi_i^{el}\rangle}{E_i^{el}-(E_j^{el}+\hbar\omega_{q\mu})}\ (n_{q\mu}+1)^{\frac{1}{2}}(\hbar/2\omega_{q\mu})^{\frac{1}{2}}$$

$$+ \sum_j \frac{\langle \Psi_j^{el};n_{k\lambda}+1|H_{int}^{i-e}|\Psi_i^{el};n_{k\lambda}\rangle\langle\Psi_f^{el}|V_q^{\mu}|\Psi_j^{el}\rangle}{E_i^{el}-(E_j^{el}+\hbar\omega_{k\lambda})}\ (n_{q\mu}+1)^{\frac{1}{2}}(\hbar/2\omega_{q\mu})^{\frac{1}{2}}\Big|^2\ \rho_f(E_f = E_i)$$

$$\approx \frac{2\pi}{\hbar}\ \left(\frac{2\pi\hbar}{\omega_{k\lambda}V}\right)\left(\frac{\hbar}{2\omega_{q\mu}}\right)\left(\frac{e}{m}\right)^2(n_{k\lambda}+1)(n_{q\mu}+1)\Big[\sum_j \frac{\langle\Psi_f^{el}|\sum_i e^{-i\underline{k}\cdot\underline{r}_i}\hat{\pi}_k^{\lambda}\cdot\underline{P}|\Psi_j^{el}\rangle\langle\Psi_j^{el}|V_q^{\mu}|\Psi_i^{el}\rangle}{E_i^{el}-(E_j^{el}+\hbar\omega_{q\mu})}\Big]^2$$

$$\times\ \rho_f(E_f = E_i), \qquad (9)$$

where we have assumed that $\omega_{k\lambda} >> \omega_{q\mu}$.

Equation (9) describes the contribution made by a specific phonon to the vibronic sideband. The total sideband reflects the addition of such contributions for all phonons of the system. The selection rules determining whether or not a specific phonon is allowed to take part in a vibronic transition are contained in the matrix elements and discussed in the next section. The density of phonon states of the host crystal is contained in the last factor in Equation (9). The observed vibronic spectral profile represents an effective density of phonon states which is the true density of states modified by the vibronic selection rules, the explicit phonon frequency dependence shown in Equation (9), and the frequency dependence contained in the electron-phonon coupling parameters. The latter point is discussed further in section three of this chapter. The temperature dependence of the vibronic transition rate is contained in the phonon occupation number,

$$n_{q\mu} = \frac{1}{e^{\hbar\omega_{q\mu}/kT} - 1} . \tag{10}$$

It should be noted that for vibronic transitions involving the absorption of a phonon the factor $(n_{q\mu} + 1)$ in Equation (9) is replaced by just $n_{q\mu}$.

Selection Rules

As shown in the last section, the selection rules for vibronic transitions are contained in the matrix elements,

$$<\Psi_f^{el}|e^{i\underline{k}\circ\underline{r}}\underline{p}\cdot\hat{\pi}_k\lambda|\Psi_j^{el}><\Psi_j^{el}|V_q^{\mu}|\Psi_i^{el}> . \tag{11}$$

The exponential may be expanded in the usual way since the wavelength of the incident radiation is large compared with the linear dimensions of the absorbing system,

$$e^{i\underline{k}\cdot\underline{r}} = 1 + i\underline{k}\cdot\underline{r} + \ldots \tag{12}$$

For electric dipole selection rules only the first term in the expansion is retained. Since the electronic wave functions are eigenstates of the ion, the matrix element of the electron momentum operator can be changed to a matrix element of the electron position operator (34),

$$\langle \Psi_f^{el} | \underline{r} | \Psi_j^{el} \rangle = \frac{-i\hbar}{m(E_f^{el} - E_j^{el})} \langle \Psi_f^{el} | \underline{P} | \Psi_j^{el} \rangle , \tag{13}$$

and the vibronic matrix elements become

$$i \frac{m}{\hbar} (E_f^{el} - E_j^{el}) \langle \Psi_f^{el} | \underline{r} \cdot \hat{\pi}_k^{\lambda} | \Psi_j^{el} \rangle \langle \Psi_j^{el} | V_q^{\mu} | \Psi_i^{el} \rangle . \tag{14}$$

Instead of using explicit expressions for the wave functions and electron-phonon interaction operator, it is simpler to use group theory and determine the selection rules by showing that the matrix elements will be zero or non-zero. In order to do this it is necessary to express the electronic wave functions and interaction operators in terms of the irreducible representations according to which they transform in the symmetry group of the system. Since the impurity ion destroys translational symmetry the important group is the point group of the site symmetry of the impurity ion. The electronic wave functions can be expressed as the Γ_i, Γ_j, and Γ_f representations of this group and $\underline{r} \cdot \hat{\pi}_k^{\lambda}$ will transform according to the same representations as x, y, or z depending on the polarization of the incident light. Since V exhibits the symmetry of the point group, $V_q^{\mu} = (\partial V / \partial Q_q^{\mu})_{Q_q^{\mu}=o}$ will transform according to the same irreducible representation as Q_q^{μ}. Thus the criteria for an allowed transition is that reduction of the direct product representation $\Gamma_i \times \Gamma_v \times \Gamma_r$ contains Γ_f or $\Gamma_i \times \Gamma_r \times \Gamma_f$ contains Γ_v, where Γ_v and Γ_r are the representations of the vibrational modes and radiation operator, respectively.

The above procedure can now be applied to the case of $SrTiO_3:Cr^{3+}$. At high temperatures (and to a first approximation at low temperatures) the chromium ion occupies a site of O_h symmetry. We will find the vibronic selection rules for this situation and then discuss how these will be modified by lowering the site symmetry to D_{4h}^{18}. Vibronic selection rules for europium doped strontium titanate have been derived previously assuming cubic symmetry (29). Since a rare earth ion goes into the lattice substitutionally for the Sr ion and involves 4f-4f transitions, the selection rules may be different than in chromium doped strontium titanate.

In O_h symmetry all three components of the electric dipole moment operator transforms as the $\Gamma_r = T_{1u}$ irreducible representation. The irreducible representations for the initial and final electronic states are $\Gamma_i = E_g$ and $\Gamma_f = A_{2g}$, respectively. The direct product of these three irreducible representations can be reduced as

$$E_g \times T_{1u} \times A_{2g} = T_{1u} + T_{2u} . \tag{15}$$

The vibronic transition is allowed only for phonon modes which transform as one of the irreducible representations that appear in the reduction of this product representation. Thus it is necessary to determine the symmetry representations of the phonon modes at all parts of the Brillouin zone. These are determined using space group theory with basis functions of the Block form,

$$f(\underline{R}) = \underline{u}_q(\underline{R})\, e^{i\underline{q}\cdot\underline{R}} , \tag{16}$$

where $\underline{u}_q(\underline{R})$ is a vector displacement of the atom at $\underline{R}$ from the equilibrium position due to a symmetry operation. When an impurity ion is placed in the lattice, translational symmetry is destroyed and only the operations which leave the impurity site invariant are included in the group.

The basis functions of interest are then those of Equation (16) with $\underline{q} = 0$ and the site group is the point group at the center of the Brillouin zone. The symmetry representations of phonons at all parts of the Brillouin zone can then be expressed in terms of the symmetry representations at the zone center.

Figure 6 shows the unit cell of strontium titanate and the first Brillouin zone with the points of high symmetry labeled. With five atoms per unit cell there should be fifteen phonon modes at each point in the Brillouin zone. For a symmorphic space group we can factor out the rotational and translational operations and treat them separately. To obtain the symmetry of the phonon modes we work with the group of the wave vector at each point in the Brillouin zone. Operations of this group $G_o(\underline{q})$ either leave $\underline{q}$ invariant or transform it into $\underline{q} + \underline{Q}$ where $\underline{Q}$ is a primitive vector of reciprocal space. Thus an operation (C) in $G_o(\underline{q})$ will leave the basis function in Equation (16) invariant or transform it into another basis function in the same set (i.e., with the same $\underline{q}$ vector).

$$\{c|o\}\,\underline{u}(\underline{R})\,e^{i\underline{q}\cdot\underline{R}} = \{c\underline{u}(\underline{R})\}\,e^{i\underline{q}\cdot(c\underline{R})} = \underline{u}(\underline{R}')\,e^{i(c\underline{q})\cdot\underline{R}}$$

$$= \underline{u}(\underline{R}')\,e^{i(\underline{q}+\underline{Q})\cdot\underline{R}} = \underline{u}(\underline{R}')\,e^{i\underline{q}\cdot\underline{R}}\,e^{i\underline{Q}\cdot\underline{R}}\,. \qquad (17)$$

The character of the group operator will be the trace of the matrix that operates on $\underline{u}(\underline{R})e^{i\underline{q}\cdot\underline{R}}$ multiplied by the factor $e^{i\underline{Q}\cdot\underline{R}}$. The former can be obtained easily by noting that only those ions whose position remains unchanged or which transform into an equivalent ion in a neighboring unit cell contribute to the character (X) of the transformation matrix,

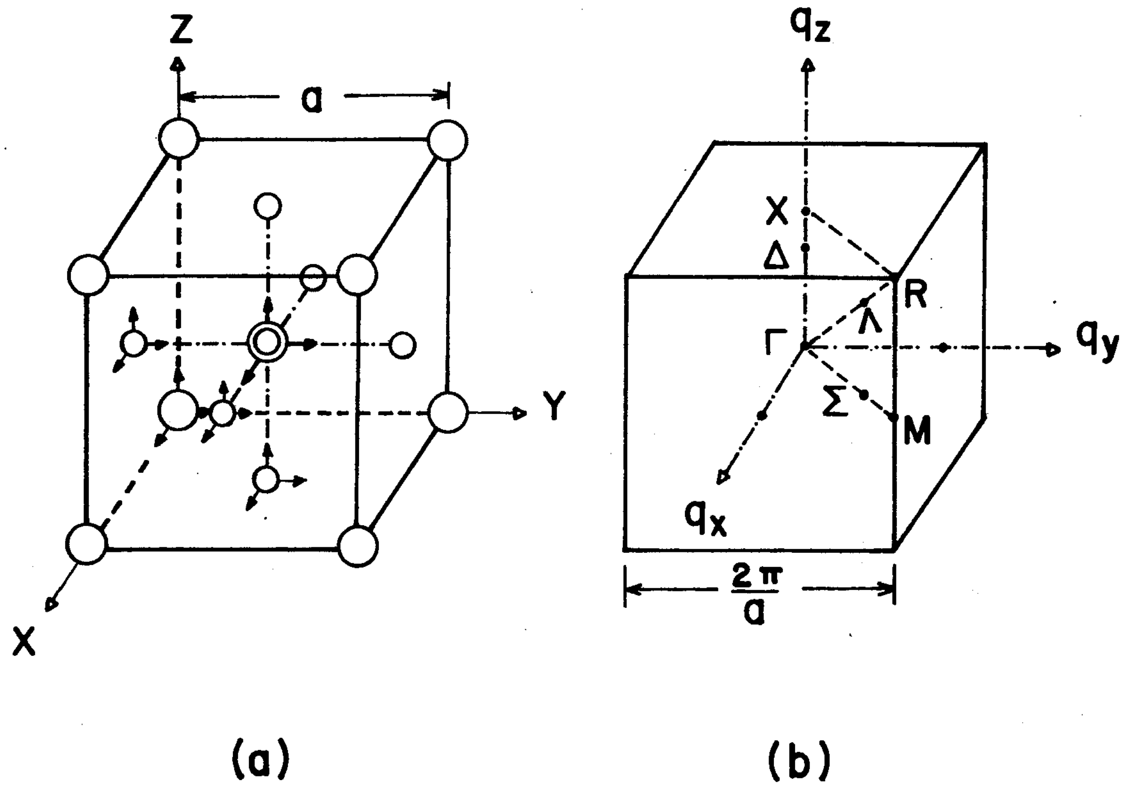
Z
a
Y
X
(a)
q_z
X
Δ
R
Λ
Γ
q_y
Σ
M
q_x
$\frac{2\pi}{a}$
(b)

Figure 6. Unit Cell (a) and First Brillouin Zone of Strontium Titanate With Five Atoms of Which Coordinates are Sr(0,0,0);○,Ti(½,½,½); ◎ O1(½,0,½); ○,O_2(1,½,½); ○ and O_3(½,½,0); ○ and the First Brillouin Zone (b) With the Points of High Symmetry Labeled.

$$\begin{pmatrix} \begin{matrix} \cos\phi & -\sin\phi & 0 \\ \sin\phi & \cos\phi & 0 \\ 0 & 0 & \pm 1 \end{matrix} & \bigcirc & \bigcirc \cdots \\ \bigcirc & \begin{matrix} \cos\phi & -\sin\phi & 0 \\ \sin\phi & \cos\phi & 0 \\ 0 & 0 & \pm 1 \end{matrix} & \bigcirc \cdots \\ \bigcirc & \bigcirc & \ddots \end{pmatrix} , \tag{18}$$

where ϕ is the angle of rotation and the + and - signs refer to proper and improper rotations, respectively. The trace of this matrix is just the character for the operation within the Brillouin zone

$$X(\phi) = N_u \, (2 \cos \phi \pm 1), \tag{19}$$

where N_u is the number of ions contributing to the trace. On the surface of the zone this becomes

$$X(\phi, \underline{R}) = \sum_u (2 \cos \phi \pm 1) \, e^{i\underline{Q} \cdot \underline{R}_u} . \tag{20}$$

Characters of this type can be determined for each symmetry operation and the resulting representation can be reduced in terms of the irreducible representations of the group of the $\underline{q}$ vector at that point. The irreducible representations appearing in this reduction represent the symmetry modes of the phonons at this point in the Brillouin zone.

Table I lists the components of the $\underline{q}$ vector, the symmetry elements which leave it invariant, and the resulting point group for the special points in the Brillouin zone which can be determined by inspection of Figure 6. Inside the Brillouin zone the exponential factor in Equation

TABLE I

SPACIAL SYMMETRY OF THE VARIOUS POINTS IN THE BRILLOUIN ZONE OF $SrTiO_3$ AT ROOM TEMPERATURE AND IRREDUCIBLE REPRESENTATIONS OF THE VIBRATIONAL MODES OF $SrTiO_3$ AT VARIOUS POINTS OF THE BRILLOUIN ZONE

Points in the B. Z.	q_x, q_y, q_z	Elements of Symmetry	Point Group	Irreducible Representations of the Vibration Modes
Γ	(0,0,0)	$E, 8C_3, 9C_2, 6C_4, i, 8S_6, 9\sigma, 6S_4$	O_h	$4T_{1u} + T_{2u}$
Δ	(0,0,q)	$E, 2C_4, C_2, 4\sigma_v$	C_{4v}	$4A_1 + B_1 + 5E$
X	(0,0,½)	$E, 2C_4, 5C_2, 2\sigma_v, 2S_4, \sigma_h, i, \sigma$	D_{4h}	$2A_{1g} + B_{1g} + 3E_g + 2A_{2u} + 2E_u$
Σ	(q,q,0)	$E, C_2, 2\sigma_v$	C_{2v}	$5A_1 + A_2 + 5B_1 + 4B_2$
M	(½,½,0)	$E, 2C_4, 5C_2, 2\sigma_v, i, 2S_4, \sigma_h, \sigma$	D_{4h}	$A_{1g}+A_{2g}+B_{1g}+B_{2g}+E_g+A_{2u}+2B_{1u}+3E_u$
Λ	(q,q,q)	$E, 2C_3, 3\sigma_v$	C_{3v}	$4A_1 + A_2 + 5E$
R	(½,½,½)	$E, 9C_2, 8C_3, 6C_4, i, 6S_4, 8S_6, 9\sigma$	O_h	$T_{2g} + A_{2u} + E_u + 2T_{1u} + T_{2u}$
K	(q_1, q_2, q_3)	E	C_1	15A

(20) will be equal to 1 since $\underset{\sim}{q}$ is too small to transform into even a primitive vector of reciprocal space and thus $\underset{\sim}{Q} = 0$. It is possible for $\underset{\sim}{Q}$ to be non-zero for points on the surface of the Brillouin zone and these are shown in Table II along with the explicit form of the character for each relevant type operation.

Now let us consider each special point in the Brillouin zone.

Γ Point: The symmetry of the wave vector at the center of the Brillouin zone is O_h. Table III shows the characters of the irreducible representations of this group and the characters obtained for the total vibrational representation (Γ_v) using Equation (20). Note that since $\underset{\sim}{q} = 0$ at this point $\underset{\sim}{Q}$ will also be zero and the exponential factors in Equation (20) will all be equal to one. The reduction of the vibrational representation is

$$\Gamma_v = 4T_{1u} + T_{2u}, \tag{21}$$

so there are four triply degenerate T_{1u} phonon modes and one triply degenerate T_{2u} modes at the zone center. Since the three acoustical modes transform like a vector they will belong to the T_{1u} representation and the other three T_{1u} modes and the T_{2u} mode will be optical phonon branches. Actually the three T_{1u} optical modes each will be split into doubly degenerate transverse modes and non-degenerate longitudinal modes due to the macroscopic electrostatic field but the symmetries involved have not been determined and the cubic mode designations are generally used to determine selection rules.

For other points inside the Brillouin zone the group of the $\underset{\sim}{q}$ vector will be subgroups of O_h and the easiest way to obtain the vibrational mode representations is through compatability relationships. These

TABLE II

MODIFIED PART OF THE CHARACTER OF VARIOUS OPERATOR AT THE SURFACE OF THE BRILLOUIN ZONE

Operators	N_u	Atoms Contributing to the Modified Factor of the Character and Their Vector Change After the Applying Operator	Modified Character $\sum_{N_u} e^{i\underline{Q}\cdot\underline{R}}$
C_{4z}	3	Ti; $\underline{R} = a\hat{i}$ Sr; $\underline{R} = 0$ O_3; $\underline{R} = a\hat{i}$	$1 + 2e^{iQ_x a}$
C_{2z}	5	Ti; $\underline{R} = 2a\hat{i} + 2a\hat{j}$ Sr; $\underline{R} = 0$ O_1; $\underline{R} = a\hat{j}$ O_2; $\underline{R} = a\hat{i}$ O_3; $\underline{R} = 2a\hat{i} + 2a\hat{j}$	$1+2e^{i2(Q_x+Q_y)a} + e^{iQ_x a} + e^{iQ_y a}$
C'_2 (45° to x and y axis)	3	Ti; $\underline{R} = a\hat{k}$ Sr; $\underline{R} = 0$ O_3; $\underline{R} = 0$	$2 + e^{iQ_z a}$
i	5	Ti; $\underline{R} = a(\hat{i}+\hat{j}+\hat{k})$ Sr; $\underline{R} = 0$ O_1; $\underline{R} = a(\hat{j}+\hat{k})$ O_2; $\underline{R} = a(\hat{k}+\hat{i})$ O_3; $\underline{R} = a(\hat{i}+\hat{j})$	$1+e^{i(Q_x+Q_y+Q_z)a} + e^{i(Q_y+Q_z)a} + e^{i(Q_z+Q_x)a} + e^{i(Q_x+Q_y)a}$

TABLE II (Continued)

Operators	N_u	Atoms Contributing to the Modified Factor of the Character and Their Vector Change After the Applying Operator	Modified Character $\sum_{N_u} e^{i\underline{Q}\cdot\underline{R}}$
$\sigma_{h_{xy}}$	5	Ti; $\underline{R} = a\hat{k}$ Sr; $\underline{R} = 0$ O_1; $\underline{R} = a\hat{k}$ O_2; $\underline{R} = a\hat{k}$ O_3; $\underline{R} = 0$	$2 + 3\ e^{iQ_z a}$
σ_d	3	Ti; $\underline{R} = 0$ Sr; $\underline{R} = 0$ O_3; $\underline{R} = 0$	3
S_{4z}	3	Ti; $\underline{R} = a\hat{i}+a\hat{k}$ Sr; $\underline{R} = 0$ O_3; $\underline{R} = a\hat{i}$	$1+e^{i(Q_x+Q_z)a}+e^{iQ_x a}$

TABLE III

CHARACTER TABLE OF O_h AND THE VIBRATIONAL MODES AT Γ POINT

O_h	E	$8C_3$	$6C_2$	$6C_4$	$3C_2(C_4^2)$	i	$6S_4$	$8S_6$	$3\sigma_h$	$6\sigma_d$
A_{1g}	1	1	1	1	1	1	1	1	1	1
A_{2g}	1	1	−1	−1	1	1	−1	1	1	−1
E_g	2	−1	0	0	2	2	0	−1	2	0
T_{1g}	3	0	−1	1	−1	3	1	0	−1	−1
T_{2g}	3	0	1	−1	−1	3	−1	0	−1	1
A_{1u}	1	1	1	1	1	−1	−1	−1	−1	−1
A_{2u}	1	1	−1	−1	1	−1	1	−1	−1	1
E_u	2	−1	0	0	2	−2	0	1	−2	0
T_{1u}	3	0	−1	1	−1	−3	−1	0	1	1
T_{2u}	3	0	1	−1	−1	−3	1	0	1	−1
N_u	5	2	3	3	5	5	3	2	5	3
$2 \cos \phi \pm 1$	3	0	−1	1	−1	−3	−1	0	1	1
$X(\Gamma_v)$	15	0	−3	3	−5	−15	−3	0	5	3

are found by determining how the representations of the vibrations at the Γ-point reduce in terms of the representations of the subgroups at the Δ, Σ, and Λ points shown in Figure 6 and at a general point in the zone designated by $\underline{q}$. Table IV shows the correlation among the elements of the O_h symmetry group and its relevant subgroups along with the compatibility relationships for their irreducible representations. This gives the symmetry designations of all phonon modes inside the Brillouin zone as summarized in Table I.

Finally we have to consider the points on the surface of the Brillouin zone. For these points $\underline{Q}$ is not necessarily zero and must be determined for each operation as described in Table II. Table V shows this along with the characters of the total vibrational representations and their reductions for the three special points on the surface of the zone shown in Figure 6. The phonon symmetries obtained in this way are summarized in Table I.

To obtain the vibronic selection rules for an impurity ion in $SrTiO_3$ it is necessary to express the vibrational representations of phonons at all points in the Brillouin zone in terms of the representations of the O_h group at the zone center. The representations of the O_h group in which each subgroup representation appears are listed in Table IV. If the representation in O_h symmetry is contained in the reduction of the direct product representation in Equation (15) then phonons whose space group representations are contained in this point group representation give allowed vibronic transitions. Other phonons do not contribute to vibronic processes. These considerations lead to the vibronic selection rules for $SrTiO_3:Cr^{3+}$ shown in Table VI.

The final point to consider is the effect of the phase transition

TABLE IV

CORRELATION AMONG ELEMENTS OF O_h AND ITS SUBGROUP PRESENTED BY AN IMPURITY ION

													Reduction In Terms of Subgroup Representations				
O_h	E	$8C_3$	$6C_2$	$6C_4$	$3C_2(C_4^2)$		i	$6S_4$	$8S_6$	$3\sigma_h$		$6\sigma_d$	D_{4h}	C_{4v}	C_{3v}	C_{2v}	C_1
A_{1g}	1	1	1	1	1		1	1	1	1		1	A_{1g}	A_1	A_1	A_1	A
A_{2g}	1	1	-1	-1	1		1	-1	1	1		-1	B_{1g}	B_1	A_2	B_1	A
E_g	2	-1	0	0	2		2	0	-1	2		0	$A_{1g}+B_{1g}$	A_1+B_1	E	A_1+B_1	2A
T_{1g}	3	0	-1	1	-1		3	1	0	-1		-1	E_g+A_{2g}	A_2+E	A_2+E	$A_2+B_1+B_2$	3A
T_{2g}	3	0	1	-1	-1		3	-1	0	-1		1	E_g+B_{2g}	B_2+E	A_1+E	$A_1+A_2+B_2$	3A
A_{1u}	1	1	1	1	1		-1	-1	-1	-1		-1	A_{1u}	A_2	A_2	A_2	A
A_{2u}	1	1	-1	-1	1		-1	1	-1	-1		1	B_{1u}	B_2	A_1	B_2	A
E_u	2	-1	0	0	2		-2	0	1	-2		0	$A_{1u}+B_{1u}$	A_2+B_2	E	A_2+B_2	2A
T_{1u}	3	0	-1	1	-1		-3	-1	0	1		1	E_u+A_{2u}	A_1+E	A_1+E	$A_1+B_1+B_2$	3A
T_{2u}	3	0	1	-1	-1		-3	1	0	1		-1	E_u+B_{2u}	B_1+E	A_2+E	$A_1+A_2+B_1$	3A
D_{4h}	E		$2C_2''$	$2C_4$	$2C'$	C_2	i	$2S_4$		σ_h	σ_v	$2\sigma_d$	O_h Representations in Which Each Subgroup Representation Appears				
A_{1g}	1		1	1	1	1	1	1		1	1	1	A_{1g},E_g				
A_{2g}	1		-1	1	-1	1	1	1		1	-1	-1	T_{1g}				
B_{1g}	1		-1	-1	1	1	1	-1		1	1	-1	A_{2g},E_g				
B_{2g}	1		1	-1	-1	1	1	-1		1	-1	1	T_{2g}				
E_g	2		0	0	0	-2	2	0		-2	0	0	T_{1g},T_{2g}				
A_{1u}	1		1	1	1	1	-1	-1		-1	-1	-1	A_{1u},E_u				
A_{2u}	1		-1	1	-1	1	-1	-1		-1	1	1	T_{1u}				
B_{1u}	1		-1	-1	1	1	-1	1		-1	-1	1	A_{2u},E_u				
B_{2u}	1		1	-1	-1	1	-1	1		-1	1	-1	T_{2u}				
E_u	2		0	0	0	-2	-2	0		2	0	0	T_{1u},T_{2u}				
C_{4v}	E			$2C_4$	C_2					$2\sigma_v$		$2\sigma_d$					
A_1	1			1	1					1		1		A_{1g},E_g,T_{1u}			
A_2	1			1	1					-1		-1		T_{1g},A_{1u},E_u			
B_1	1			-1	1					1		-1		A_{2g},E_g,T_{2u}			
B_2	1			-1	1					-1		1		T_{2g},A_{2u},E_u			
E	2			0	-2					0		0		$T_{1g},T_{2g},T_{1u},T_{2u}$			
C_{3v}	E	$2C_3$										$3\sigma_v$					
A_1	1	1										1			$A_{1g},T_{2g},A_{2u},T_{1u}$		
A_2	1	1										-1			$A_{2g},T_{1g},A_{1u},T_{2u}$		
E	2	-1										0			$E_g,T_{1g},T_{2g},E_u,$ T_{1u},T_{2u}		
C_{2v}	E		C_2							σ_v (xz)		σ_v (yz)					
A_1	1		1							1		1				$A_{1g},E_g,T_{2g},$ T_{1u},T_{2u}	
A_2	1		1							-1		-1				$T_{1g},T_{2g},A_{1u},$ E_u,T_{2u}	
B_1	1		-1							1		-1				$A_{2g},E_g,T_{1g},$ T_{1u},T_{2u}	
B_2	1		-1							-1		1				$T_{1g},T_{2g},A_{2u},$ E_u,T_{1u}	
C_1	E																
A	1																$A_{1g},A_{2g},E_g,T_{1g},$ $T_{2g},A_{1u},A_{2u},E_u,$ T_{1u},T_{2u}

TABLE V

TOTAL REPRESENTATIONS AND THEIR REDUCTIONS ON THE SURFACE OF THE BRILLOUIN ZONE

Point	O_h	E	$8C_3$	$6C_2$	$6C_4$	$3C_2(C_4^2)$	i	$6S_4$	$8S_6$	$3\sigma_h$	$6\sigma_d$	Reductions
R	$2\cos\phi \pm 1$	3	0	−1	1	−1	−3	−1	0	1	1	
	$N_u^{\Sigma} e^{iQ\cdot R}$	5		1	−1	1	3	1		−1	3	
	$X(\Gamma_v)$	15	0	−1	−1	−1	−9	−1	0	−1	3	$T_{2g}+A_{2u}+E_u+2T_{1u}+T_{2u}$

Point	D_{4h}	E	$2C_2''$	$2C_4$	$2C'$	C_2	i	$2S_4$	σ_h	σ_v	$2\sigma_d$	Reductions
X	$2\cos\phi \pm 1$	3	−1	1	−1	−1	−3	−1	1	1	1	
	$N_u^{\Sigma} e^{iQ\cdot R}$	5	1	3	−1	5	−1	1	−1	5	3	
	$X(\Gamma_v)$	15	−1	3	1	−5	3	−1	−1	5	3	$2A_{1g}+B_{1g}+3E_g+2A_{2u}+2E_u$
M	$2\cos\phi \pm 1$	3	−1	1	−1	−1	−3	−1	1	1	1	
	$N_u^{\Sigma} e^{iQ\cdot R}$	5	3	−1	−1	1	1	−1	5	−1	3	
	$X(\Gamma_v)$	15	−3	−1	1	−1	−3	1	5	−1	3	$A_{1g}+A_{2g}+B_{1g}+B_{2g}+E_g+A_{2u}+2B_{1u}+3E_u$

TABLE VI

ALLOWED VIBRATIONAL MODES FROM ^2E_g BY ELECTRIC DIPOLE TRANSITION $\Gamma_r(T_{1u})$ IN VARIOUS POINT IN THE BRILLOUIN ZONE

Final states allowed Possible vibrational modes			A_{1g}	A_{2g}	E_g	T_{1g}	T_{2g}
O_h	R	T_{2g}					
		A_{2u}				x	x
		E_u				x	x
		T_{1u}	x	x	x	x	x
		T_{2u}	x	x	x	x	x
	Γ	T_{1u}	x	x	x	x	x
		T_{2u}	x	x	x	x	x
D_{4h}	M	A_{1g}					
		A_{2g}					
		B_{1g}					
		B_{2g}					
		E_g					
		A_{2u}	x	x	x	x	x
		B_{1u}				x	x
		E_u	x	x	x	x	x
	X	A_{1g}					
		B_{1g}					
		E_g					
		A_{2u}	x	x	x	x	x
		E_u	x	x	x	x	x
C_{4v}	Δ	A_1	x	x	x	x	x
		B_1	x	x	x	x	x
		E	x	x	x	x	x
C_{3v}	Λ	A_1	x	x	x	x	x
		A_2	x	x	x	x	x
		E	x	x	x	x	x

TABLE VI (Continued)

Final states allowed / Possible vibrational modes			A_{1g}	A_{2g}	E_g	T_{1g}	T_{2g}
C_{2v}	Σ	A_1	x	x	x	x	x
		A_2	x	x	x	x	x
		B_1	x	x	x	x	x
		B_2	x	x	x	x	x
C_1	K	A	x	x	x	x	x

to lower symmetry below 110°K. This acts as only a small perturbation on the cubic symmetry of the system. Since the great majority of phonon modes are allowed to take part in vibronic transitions in cubic symmetry, the most important effect of this transition will be to split some of the degenerate modes. The distortion accompanying the rotation of the oxygen octahedra can be represented by B_{2u} in D_{4h}^{18} symmetry. Thus all phonon symmetry designations in the O_h group can be reduced in terms of the new D_{4h}^{18} point symmetry and the reduction of the direct product of these representations with B_{2u} gives the new phonon symmetry designations. These are summarized in Table VII and show the splittings of some of the doubly and triply degenerate modes.

The results of these symmetry considerations will be discussed further in the interpretation of the vibronic spectra in Chapter IV.

Derivation of the Equation for the Spectral Profile

The transition probability per unit time for a vibronic transition involving a specific photon and phonon was derived in Section 1 of this chapter. Now we would like to derive an expression to describe the whole vibronic band made up of transitions involving phonons and photons of many different frequencies. To do this we begin by using the formal expression for the transition rate instead of the Golden Rule

$$P_{ab} = \frac{d}{dt} \sum_b |C_b(t)|^2 \ . \tag{22}$$

The development of the amplitude function in the interaction picture can be found in standard quantum mechanics texts (34). It is convenient to

TABLE VII

SPLITTINGS OF THE VIBRATIONAL MODES OF CUBIC SYMMETRY UNDER THE DISTORTION (B_{1u}) INTO TETRAGONAL SYMMETRY (6)

Vibrational Mode in Cubic Symmetry (O_h)	Reduction in D_{4h} Symmetry	Splittings of the Vibrational Mode in Tetragonal Symmetry (D_{4h})
A_{2u}	B_{1u}	A_{2g}
T_{2g}	$E_g + B_{2g}$	E_u A_{1u}
T_{1u}	$E_u + A_{2u}$	E_g B_{1g}
E_u	$A_{1u} + B_{1u}$	B_{2g} A_{2g}
T_{2u}	$E_u + B_{2u}$	E_g A_{1g}

express it in terms of the time translation operator given by

$$U(t,t_o) = e^{iH_o t/\hbar}\, e^{-iH(t-t_o)/\hbar}\, e^{-iH_o t_o/\hbar} \, . \tag{23}$$

This obeys the differential equation

$$i\hbar\, dU(t,t_o)/dt = V(t)U(t,t_o) \tag{24}$$

where V(t) is the interaction potential in the interaction picture which is related to the Schroedinger interaction potential by

$$V(t) = e^{iH_o t/\hbar}\, V\, e^{-H_o t/\hbar} \, . \tag{25}$$

The differential equation for $U(t,t_o)$ can be rewritten as an integral equation and expanded as a power series in terms of V(t)

$$\begin{aligned} U(t,t_o) &= 1 - \frac{i}{\hbar} \int_{t_o}^{t} V(t')U(t',t_o)dt' \\ &= 1 - \frac{i}{\hbar} \int_{t_o}^{t} V(t')dt' + \left(\frac{-i}{\hbar}\right)^2 \int_{t_o}^{t} V(t')dt' \int_{t_o}^{t} V'(t'')dt'' + \ldots \end{aligned} \tag{26}$$

Using the time ordering operator this can be written in the form

$$\begin{aligned} U(t,t_o) &= 1 + \sum_{n=1}^{\infty} \frac{1}{n!} \left(\frac{-i}{\hbar}\right)^n \int_{t_o}^{t} \int_{t_o}^{t} \ldots \int_{t_o}^{t} dt_1 dt_2 \ldots dt_n T[V(t_1)V(t_2)\ldots V(t_n)] \\ &= T \exp \left[- \frac{i}{\hbar} \int_{t_o}^{t} V(t')dt'\right] \, . \end{aligned} \tag{27}$$

The time translation operator has the following useful properties:

$$U(t,t'') = U(t,t')U(t',t''), \tag{28}$$

$$U(t,t_o)|\Psi(t_o)> = |\Psi(t)> , \tag{29}$$

$$\lim_{t_o \to \infty} U(0,t_o)|\Psi_a> = |\Psi_a^+> , \tag{30}$$

where $|\Psi_a>$ is an eigenstate of H_0 and $|\Psi_a^+>$ is an eigenstate of $H = H_0 + V(t)$. In the limit of $t_0 \to -\infty$ the matrix element of $U(t,t_0)$ is just the transition amplitude $c_b(t)$.

Thus the transition rate to an eigenstate b in Equation (22) can be rewritten in terms of the time development operator as

$$\begin{aligned} P_{ab} &= \lim_{t_o \to -\infty} \frac{d}{dt}|<\Psi_b|U(t,t_o)|\Psi_a>|^2 \\ &= \lim_{t_o \to -\infty} \frac{d}{dt} <\Psi_a|U(t,t_o)^*|\Psi_b><\Psi_b|U(t,t_o)|\Psi_a> . \end{aligned} \tag{31}$$

where $|\Psi_b>$ is an eigenstate of H_o. Equation (24) can be used to evaluate the time derivative

$$P_{ab} = \frac{2}{\hbar} \text{Im} \lim_{t_o \to -\infty} <\Psi_a|U(t,t_o)^*|\Psi_b><\Psi_b|V(t)U(t,t_o)|\Psi_a>. \tag{32}$$

In order to evaluate the matrix element we can use Equation (28) to make the substitution

$$U(t,t_o) = U(t,0)U(0,t_o),$$

so that Equation (30) can then be applied

$$\begin{aligned} P_{ab} &= \frac{2}{\hbar} \text{Im} \lim_{t_o \to -\infty} <\Psi_a|U^*(0,t_o)U^*(t,0)|\Psi_b><\Psi_b|V(t)U(t,0)U(0,t_o)|\Psi_a> \\ &= \frac{2}{\hbar} \text{Im} <\Psi_a^+|e^{iHt/\hbar} e^{-iH_o t/\hbar}|\Psi_b><\Psi_b|e^{iH_o t/\hbar} V e^{-iHt/\hbar}|\Psi_a^+> \end{aligned}$$

$$= \frac{2}{\hbar} \, \mathrm{Im} \, \langle \Psi_a^{+} | \Psi_b \rangle \langle \Psi_b | V | \Psi_a^{+} \rangle \ , \tag{33}$$

where the expressions for $U(t,t_o)$ and $V(t)$ in Equations (23) and (25) have been used. Next we can use an iteration expansion to write the wave function (34)

$$| \Psi_a^{+} \rangle = | \Psi_a \rangle + \lim_{\varepsilon \to o} \frac{1}{E_a - H_o + i\hbar\varepsilon} V | \Psi_a^{+} \rangle + \ . \ . \ . \ . \tag{34}$$

Thus,

$$P_{ab} = \frac{2}{\hbar} \, \mathrm{Im} \left[\langle \Psi_a | \Psi_b \rangle + \lim_{\varepsilon \to o} \langle \Psi_a^{+} \left| \frac{V}{E_a - H_o - i\hbar\varepsilon} \right| \Psi_b \rangle \right]$$

$$\times \left[\langle \Psi_b | V | \Psi_a \rangle + \lim_{\varepsilon \to o} \langle \Psi_b | V \frac{1}{E_a - H_o + i\hbar\varepsilon} V | \Psi_a^{+} \rangle \right]$$

$$= \frac{2}{\hbar} \, \mathrm{Im} \left[\delta(b-a) + \lim_{\varepsilon \to o} \frac{R^{*}_{ba}}{E_a - E_b - i\hbar\varepsilon} \right]$$

$$\times \left[V_{ba} + \lim_{\varepsilon \to o} \sum_c \langle \Psi_b \left| \frac{V}{E_a - E_c + i\hbar\varepsilon} \right| \Psi_c \rangle \langle \Psi_c | V | \Psi_a^{+} \rangle \right]$$

$$= \frac{2}{\hbar} \, \mathrm{Im} \left[\delta(b-a) + \lim_{\varepsilon \to o} \frac{R^{*}_{ba}}{E_a - E_b - i\hbar\varepsilon} \right] \left[R_{ba} \right]$$

$$= \frac{2}{\hbar} \, \mathrm{Im} \, R_{ba} \, \delta(b-a) + \frac{2}{\hbar} \, \mathrm{Im} \lim_{\varepsilon \to o} \frac{|R_{ba}|^2}{E_a - E_b - i\hbar\varepsilon} \ , \tag{35}$$

where

$$R_{ba} = \langle \Psi_b | V | \Psi_a^{+} \rangle = \langle \Psi_b | V | \Psi_a \rangle + \sum_c \frac{V_{bc} V_{ca}}{E_a - E_c + i\hbar\varepsilon} + \dots$$

$$= V_{ba} + \sum_c \frac{V_{bc} V_{ca}}{E_a - E_c + i\hbar\varepsilon} + \dots \tag{36}$$

which is called the "reaction matrix".

Since for our case b $\neq$ a the first term in Equation (35) is zero. The limiting value of the second term can be expressed in terms of Cauchey's principal value plus a delta function (34)

$$\lim_{\varepsilon \to 0} \frac{1}{x \pm i\hbar\varepsilon} = P(\frac{1}{x}) \mp i\pi\delta(x) \ . \tag{37}$$

Substituting this into Equation (35) gives

$$P_{ab} = \frac{2\pi}{\hbar} |R_{ba}|^2 \, \delta(E_a - E_b) \ . \tag{38}$$

It is usually necessary to retain only the first term in the expansion of the reaction matrix in Equation (36) leaving us with

$$P_{ab} = \frac{2\pi}{\hbar} |V_{ba}|^2 \, \delta(E_a - E_b) \ , \tag{39}$$

which is the transition rate in the first Born approximation.

Using the integral representation of the delta function we have

$$P_{ab} = \frac{1}{\hbar^2} <\Psi_a|V^* \int_{-\infty}^{\infty} dt \; e^{i(H_a - H_b)t/\hbar} |\Psi_b><\Psi_b|V|\Psi_a> \ . \tag{40}$$

To obtain the total transition rate this expression must be averaged over initial states and summed over final states

$$P_{ab} = \frac{1}{\hbar^2} \mathop{Av}_{a} \sum_{b} <\Psi_a|V^* \int_{-\infty}^{\infty} dt \; e^{i(H_a - H_b)t/\hbar} |\Psi_b> \quad <\Psi_b|V|\Psi_a>. \tag{41}$$

This general expression must now be specialized to the case of a vibronic transition. Using the Born-Oppenheimer approximation the wave functions of the initial and final states can be written as products of electronic and vibrational wave functions and the Hamiltonians for a vibronic emission transition are sums of electronic and phonon Hamiltonian

$$H_a = H_e = H_e^{el} + H_e^{ph} \tag{42}$$

$$H_b = H_g = H_g^{el} + H_g^{ph} + \hbar\omega + M, \tag{43}$$

where $\hbar\omega$ is the energy of the emitted photon and M is the electromagnetic multipole moment operator causing the transition. The initial state phonon configuration is taken to be in equilibrium so

$$H_e^{ph} = \sum_q \hbar\omega_q \, (b_q^+ \, b_q + \tfrac{1}{2}), \tag{44}$$

while the final state phonon configuration includes the interaction between electrons and phonons

$$H_g^{ph} = \sum_q \hbar\omega_q \, (b_q^+ \, b_q + \tfrac{1}{2}) + V \, . \tag{45}$$

The electron phonon interaction Hamiltonian is given in Equation (6). Thus

$$P_{ab} = \frac{1}{\hbar^2} \mathop{Av}_a \sum_b \langle\{n_{q_a}\}|\langle\Psi_a^{el}|(M^*) \int_{-\infty}^{\infty} dt \, e^{-i\omega t} \, e^{i(H_e^{el}-H_g^{el})t/\hbar} \, e^{i(H_e^{ph}-H_g^{ph})t/\hbar}$$

$$\times \, |\Psi_b^{el}\rangle|\{n_{q_b}\}\rangle\langle\{n_{q_b}\}|\langle\Psi_b^{el}|M|\Psi_a^{el}\rangle|\{n_{q_a}\}\rangle \, .$$

Assuming that the Franck-Condon approximation is valid so the electron transition is independent of the nuclear coordinates, the electronic matrix elements can be evaluated

$$P_{ab} = \frac{1}{\hbar^2} \underset{a}{\mathrm{Av}} \sum_b \int_{-\infty}^{\infty} dt\, e^{-i\omega t}\, e^{i(E_e^{el}-E_g^{el})t/\hbar} \langle\{n_{q_a}\}|M_{ab}^* \, e^{i(H_e^{ph}-H_g^{ph})t/\hbar}$$

$$\times\ |\{n_{q_b}\}\rangle\langle\{n_{q_b}\}|M_{ab}|\{n_{q_a}\}\rangle$$

$$= \frac{1}{\hbar^2} \int_{-\infty}^{\infty} dt\, e^{-i\omega t}\, e^{i\omega_o t} \underset{a}{\mathrm{Av}} \langle\{n_{q_a}\}|e^{iH_e^{ph}t/\hbar}\, e^{-iH_g^{ph}t/\hbar}|\{n_{q_a}\}\rangle |M_{ab}|^2$$

$$= \frac{1}{\hbar^2} |M_{ab}|^2 \int_{-\infty}^{\infty} dt\, e^{-i(\omega-\omega_o)t} \langle U(t,0)\rangle_a\ , \tag{46}$$

where the definition of $U(t,t_o)$ in Equation (23) has been used with the phonon Hamiltonian substituted for H and H_o.

If we treat explicitly an electric dipole emission transition and account for the density of final photon states and the effective electromagnetic field in the crystal this becomes (35)

$$P_{ab}(ed) = \left[\frac{n^3}{\varepsilon} \left(\frac{E_e}{E}\right)^2\right] \left(\frac{8\ \pi}{\hbar c^3}\right) \omega^3\ |M_{ab}^{ed}|^2\ G(ab;\omega)$$

$$= C\ \omega^3\ |M_{ab}^{ed}|^2\ G(ab;\omega), \tag{47}$$

where

$$G(ab;\omega) = \int_{-\infty}^{\infty} dt\ e^{-i\omega t}\ G(ab;t), \tag{48}$$

$$G(ab;t) = \langle U(t,0)\rangle_a\ e^{i\omega_o t}\ , \tag{49}$$

and C is constant. $G(ab;\omega)$ is called the spectral distribution function.

To evaluate the average value in the spectral distribution function it is helpful to use the expression for U(t,0) in Equation (27) and group the expansion products as a cumulant average using the generating function (2)

$$\ln \langle e^{tX} \rangle = \sum_{n=1}^{\infty} (t^n/n!) \langle X^n \rangle_c , \tag{50}$$

so

$$\begin{aligned} \langle X \rangle_c &= \langle X \rangle \\ \langle X^2 \rangle_c &= \langle X^2 \rangle - \langle X \rangle^2 \\ \langle X^3 \rangle_c &= \langle X^3 \rangle - 3\langle X^2 \rangle \langle X \rangle + 2 \langle X \rangle^3 \\ &\vdots \end{aligned} \tag{51}$$

Thus,

$$\begin{aligned} G(ab;t) &= \exp\left[\sum_{n=1} \left(\frac{-i}{\hbar}\right)^n \left(\frac{1}{n!}\right) \int_0^t dt_1 \cdots \int_0^t dt_n \langle T\, V(t_1) \cdots V(t_n) \rangle_{ca}\right] e^{i\omega_o t} \\ &= e^{g(t)} , \end{aligned} \tag{52}$$

where

$$g(t) = \left\{\frac{-i}{\hbar} \int_0^t dt_1 \langle V(t_1) \rangle_{ca} - \frac{1}{\hbar^2} \int_0^t dt_1 \int_0^{t_1} dt_2 \langle TV(t_1)V(t_2) \rangle_{ca} + \cdots \right\} e^{i\omega_o t} . \tag{53}$$

The averages in this expansion can be evaluated term by term using the Equation (25) for V(t) and the Hamiltonian in Equation (6). For the first term

$$\langle V(t_1) \rangle_{ca} = \langle V(t_1) \rangle_a = \langle \{n_{q_a}\} | e^{iH_e^{ph} t_1/\hbar} V e^{-iH_e^{ph} t_1/\hbar} | \{n_{q_a}\} \rangle$$

$$= \langle \{n_{q_a}\} | \sum_q (V_q b_q + V_q{}^* b_q{}^+) + \tfrac{1}{2} \sum_{qq'} V_{qq'} (b_q + b_q{}^+)(b_{q'} + b^+_{q'}) | \{n_{q_a}\} \rangle$$

$$= \tfrac{1}{2} \sum_{q,q'} V_{qq'} \, [(\bar{n}_q + 1)\delta_{q,q'} + \bar{n}_q \delta_{q,q'}]$$

$$= \tfrac{1}{2} \sum_q V_{qq} \, (2\bar{n}_q + 1) \; . \qquad (54)$$

Since this is independent of time the integral over time is just

$$\int_0^t dt_1 \, \langle V(t_1) \rangle_{ca} = \tfrac{1}{2} \sum_q V_{qq} \, (2\bar{n}_q + 1) t \; . \qquad (55)$$

Using Equation (51) the next term in the expansion is

$$\langle TV(t_1)V(t_2) \rangle_{ca} = \langle TV(t_1)V(t_2) \rangle - \langle V(t_1) \rangle \langle V(t_2) \rangle \; . \qquad (56)$$

The second term is just the product of two terms like Equation (54)

$$\int_0^t dt_1 \int_0^{t_1} dt_2 \, \langle V(t_1) \rangle \langle V(t_2) \rangle = [\tfrac{1}{2} \sum_q V_{qq} \, (2\bar{n}_q + 1)]^2 \, \frac{t^2}{2} \; . \qquad (57)$$

The first term can be calculated as

$$\langle TV(t_1)V(t_2) \rangle = \langle \{n_{q_a}\} | e^{iH_e^{ph} t_1/\hbar} V e^{-H_e^{ph} t_1/\hbar} e^{iH_e^{ph} t_2/\hbar} V e^{iH_e^{ph} t_2/\hbar} | \{n_{q_a}\} \rangle$$

$$= \langle \{n_{q_a}\} | e^{iH_e^{ph} t_1/\hbar} [\sum_{q_1} (V_{q_1} b_{q_1} + V^*_{q_1} b^+_{q_1}) + \tfrac{1}{2} \sum_{q_1 q_2} V_{q_1 q_2}$$

$$(b_{q_1} + b^+_{q_1}) \quad (b_{q_2} + b^+_{q_2})] \, e^{-iH_e^{ph} t_1/\hbar} \, e^{iH_2^{ph} t_2/\hbar}$$

$$[\sum_{q_3} (V_{q_3} b_{q_3} + V^*_{q_3} b^+_{q_3}) + \tfrac{1}{2} \sum_{q_3 q_4} V_{q_3 q_4} (b_{q_3} + b^+_{q_3})$$

$$(b_{q_4} + b^+_{q_4})] \, e^{iH_e^{ph} t_2/\hbar} | \{n_{q_a}\} \rangle$$

$$= \langle \{n_{q_a}\} | e^{iH_e^{ph} t_1/\hbar} \Big[\sum_{q_1} (V_{q_1} b_{q_1} + V^*_{q_1} b^+_{q_1}) + \tfrac{1}{2} \sum_{q_1 q_2} V_{q_1 q_2} \{ (b_{q_1} + b^+_{q_1}) e^{iH_e^{ph} t_1/\hbar}$$

$$\times e^{-iH_e^{Ph} t_1/\hbar} (b_{q_2} + b^+_{q_2}) \}$$

$$\times e^{iH_e^{ph} t_1/\hbar} \Big] \Big[e^{iH_e^{ph} t_2/\hbar} \sum_{q_3} (V_{q_3} b_{q_3} + V^*_{q_3} b^+_{q_3}) + \tfrac{1}{2} \sum_{q_3 q_4} V_{q_3 q_4} \{ (b_{q_3} + b^+_{q_3})$$

$$\times e^{-iH_e^{ph} t_2/\hbar} e^{-iH_e^{ph} t_2/\hbar} (b_{q_4} + b^+_{q_4}) \} e^{-iH_e^{ph} t_2/\hbar} \Big] | \{n_{q_a}\} \rangle$$

$$= \sum_{q_1 q_3} \Big[V_{q_1} V^*_{q_3} e^{-i\omega_{q_1} t_1} e^{i\omega_{q_3} t_2} \langle \{n_{q_a}\} | b_{q_1} b^+_{q_3} | \{n_{q_a}\} \rangle + V^*_{q_1} V_{q_3}$$

$$e^{i\omega_{q_1} t_1} e^{-i\omega_{q_3} t_2}$$

$$\times \langle \{n_{q_a}\} | b^+_{q_1} b_{q_3} | \{n_{q_a}\} \rangle \Big] + \tfrac{1}{4} \sum_{q_1 q_2 q_3 q_4} V_{q_1 q_2} V_{q_3 q_4}$$

$$\times \Big[e^{-i(\omega_{q_1} + \omega_{q_2}) t_1} e^{i(\omega_{q_3} + \omega_{q_4}) t_2} \langle \{n_{q_a}\} | b_{q_1} b_{q_2} b^+_{q_3} b^+_{q_4} | \{n_{q_a}\} \rangle$$

$$+ e^{i(\omega_{q_1} - \omega_{q_2}) t_1} e^{i(\omega_{q_3} - \omega_{q_4}) t_2} \langle \{n_{q_a}\} | b^+_{q_1} b_{q_2} b^+_{q_3} b_{q_4} | \{n_{q_a}\} \rangle$$

$$+ e^{i(\omega_{q_1} - \omega_{q_2}) t_1} e^{-i(\omega_{q_3} - \omega_{q_4}) t_2} \langle \{n_{q_a}\} | b^+_{q_1} b_{q_2} b^+_{q_3} b_{q_4} | \{n_{q_a}\} \rangle$$

$$+ e^{i(\omega_{q_1} - \omega_{q_2}) t_1} e^{-i(\omega_{q_3} - \omega_{q_4}) t_2} \langle \{n_{q_a}\} | b^+_{q_1} b_{q_2} b_{q_3} b^+_{q_4} | \{n_{q_a}\} \rangle$$

$$+ e^{-i(\omega_{q_1}-\omega_{q_2})t_1} e^{i(\omega_{q_3}-\omega_{q_4})t_2} <\{n_{q_a}\}|b_{q_1} b^+_{q_2} b^+_{q_3} b_{q_4}|\{n_{q_a}\}>$$

$$+ e^{-i(\omega_{q_1}-\omega_{q_2})t_1} e^{-i(\omega_{q_3}-\omega_{q_4})t_2} <\{n_{q_a}\}|b_{q_1} b^+_{q_2} b_{q_3} b^+_{q_4}|\{n_{q_a}\}>$$

$$+ e^{i(\omega_{q_1}+\omega_{q_2})t_1} e^{-i(\omega_{q_3}+\omega_{q_4})t_2} <\{n_{q_a}\}|b^+_{q_1} b^+_{q_2} b_{q_3} b_{q_4}|\{n_{q_a}\}>] \ . \tag{58}$$

For Equation (58) we used the facts that

$$\begin{aligned} <n|e^{iH_e^{ph}t/\hbar} b_q e^{-iH_e^{ph}t/\hbar}|n> &= e^{-i\omega_q t} <n|b_q|n> \\ <n|e^{iH_e^{ph}t/\hbar} b^+_q e^{-iH_e^{ph}t/\hbar}|n> &= e^{i\omega_q t} <n|b_q{}^+|n> \ , \end{aligned} \tag{59}$$

and only terms which contain same number of creation ($b_q{}^+$) and annihilation (b_q) operators are non-zero. Temporarily ignoring the time dependent exponents, further computation of the Equation (58), each of eight matrix elements of the Equation (58) should be calculated as follows:

$$<\{n_{q_a}\}|b_{q_1} b_{q_3}{}^+|\{n_{q_a}\}> = (\bar{n}_{q_1}+1)\delta_{q_1q_3} \tag{60}$$

$$<\{n_{q_a}\}|b^+_{q_1} b_{q_3}|\{n_{q_a}\}> = \bar{n}_{q_1}\delta_{q_1q_3} \tag{61}$$

For the next six calculations it is necessary to consider all the possible combinations of the operator $b^+_{q_i} b_{q_j}$ because of the summation over all q_i. For $<\{n_{q_a}\}|b_{q_1} b_{q_2} b^+_{q_3} b^+_{q_4}|\{n_{q_a}\}>$ there are two possible combinations of $b^+_{q_i} b_{q_j}$ namely $b_{q_1} b^+_{q_3}$, $b_{q_2} b^+_{q_4}$ and $b_{q_1} b^+_{q_4}$, $b_{q_2} b^+_{q_3}$. For the first combination,

$$
\begin{aligned}
\langle\{n_{q_a}\}|b_{q_1} b_{q_2} b^+_{q_3} b^+_{q_4}|\{n_{q_a}\}\rangle &= \langle\{n_{q_a}\}|b_{q_2} b_{q_1} b^+_{q_3} b^+_{q_4}|\{n_{q_a}\}\rangle \\
&= \langle\{n_{q_a}\}|b_{q_2}(b^+_{q_3} b_{q_1} + \delta_{q_1q_3})b^+_{q_4}|\{n_{q_a}\}\rangle \\
&= \langle\{n_{q_a}\}|b_{q_2} b^+_{q_3} b_{q_1} b^+_{q_4}|\{n_{q_a}\}\rangle + \delta_{q_1q_3} \langle\{n_{q_a}\}|b_{q_2} b^+_{q_4}|\{n_{q_a}\}\rangle \\
&= \sum_{n'_{q_a} n''_{q_a}} \langle\{n_{q_a}\}|b_{q_2}|\{n''_{q_a}\}\rangle\langle\{n''_{q_a}\}|b^+_{q_3} b_{q_1}|\{n'_{q_a}\}\rangle\langle\{n'_{q_a}\}|b^+_{q_4}|\{n_{q_a}\}\rangle \\
&\qquad + \delta_{q_1q_3}\,\delta_{q_2q_4}\,(\bar{n}_{q_2}+1) \\
&= \bar{n}_{q_1}(\bar{n}_{q_2}+1)\,\delta_{q_1q_3}\,\delta_{q_2q_4} + \delta_{q_1q_3}\,\delta_{q_2q_4}\,(\bar{n}_{q_2}+1) \\
&= (\bar{n}_{q_1}+1)(\bar{n}_{q_2}+1)\,\delta_{q_1q_3}\,\delta_{q_2q_4} \qquad (62)
\end{aligned}
$$

where the commutation relation $[b_q, b^+_{q'}] = \delta_{qq'}$ has been used.

For the second combination

$$
\begin{aligned}
\langle\{n_{q_a}\}|b_{q_1} b_{q_2} b^+_{q_3} b^+_{q_4}|\{n_{q_a}\}\rangle &= \langle\{n_{q_a}\}|b_{q_1}(b^+_{q_3} b_{q_2} + \delta_{q_2q_3})b^+_{q_4}|\{n_{q_a}\}\rangle \\
&= \sum_{n'_{q_a} n''_{q_a}} \langle\{n_{q_a}\}|b_{q_1}|\{n'_{q_a}\}\rangle\langle\{n'_{q_a}\}|b^+_{q_3} b_{q_2}|\{n''_{q_a}\}\rangle\langle\{n''_{q_a}\}|b^+_{q_4}|\{n_{q_a}\}\rangle \\
&\qquad +(\bar{n}_{q_1}+1)\,\delta_{q_1q_4}\,\delta_{q_2q_3}
\end{aligned}
$$

$$= (\bar{n}_{q_1}+1)\ \bar{n}_{q_2}\ \delta_{q_2q_3}\ \delta_{q_1q_4} + (\bar{n}_{q_1}+1)\ \delta_{q_1q_4}\ \delta_{q_2q_3}$$

$$= (\bar{n}_{q_1}+1)\ (\bar{n}_{q_2}+1)\ \delta_{q_1q_4}\ \delta_{q_2q_3}\ . \tag{63}$$

So we may write the third term as

$$<\{n_{q_a}\}|b_{q_1}b_{q_2}b^+_{q_3}b^+_{q_4}|\{n_{q_a}\}> = (\bar{n}_{q_1}+1)(\bar{n}_{q_2}+1)\ \delta_{q_1q_3}\ \delta_{q_2q_4} +$$

$$(\bar{n}_{q_1}+1)(\bar{n}_{q_2}+1)\ \delta_{q_1q_4}\ \delta_{q_2q_3}$$

$$= (\bar{n}_{q_1}+1)(\bar{n}_{q_2}+1)(\delta_{q_1q_3}\ \delta_{q_2q_4} + \delta_{q_1q_4}\ \delta_{q_2q_3})\ . \tag{64}$$

In similar fashion we have values of the other five terms as

$$<\{n_{q_a}\}|b^+_{q_1}b_{q_2}b^+_{q_3}b_{q_4}|\{n_{q_a}\}> = \bar{n}_{q_1}\bar{n}_{q_3}\ \delta_{q_1q_2}\ \delta_{q_3q_4} + \bar{n}_{q_1}(\bar{n}_{q_2}+1)\delta_{q_1q_4}\delta_{q_2q_3}\ , \tag{65}$$

$$<\{n_{q_a}\}|b^+_{q_1}b_{q_2}b_{q_3}b_{q_4}^+|\{n_{q_a}\}> = \bar{n}_{q_1}(\bar{n}_{q_3}+1)\delta_{q_1q_2}\delta_{q_3q_4} + \bar{n}_{q_1}(\bar{n}_{q_2}+1)\delta_{q_1q_3}\delta_{q_2q_4}, \tag{66}$$

$$<\{n_{q_a}\}|b_{q_1}b_{q_2}^+b_{q_3}^+b_{q_4}|\{n_{q_a}\}> = (\bar{n}_{q_1}+1)\bar{n}_{q_3}\delta_{q_1q_2}\delta_{q_3q_4} + (\bar{n}_{q_1}+1)\bar{n}_{q_2}\delta_{q_1q_3}\delta_{q_2q_4}, \tag{67}$$

$$<\{n_{q_a}\}|b_{q_1}b_{q_2}^+b_{q_3}b_{q_4}|\{n_{q_a}\}> = (\bar{n}_{q_3}+1)(\bar{n}_{q_3}+1)\delta_{q_1q_2}\delta_{q_3q_4} + (\bar{n}_{q_1}+1)\bar{n}_{q_2}$$

$$\delta_{q_1q_4}\ \delta_{q_2q_3}, \tag{68}$$

$$<\{n_{q_a}\}|b^+_{q_1}b^+_{q_2}b_{q_3}b_{q_4}|\{n_{q_a}\}> = \bar{n}_{q_1}\bar{n}_{q_2}\ (\delta_{q_1q_4}\ \delta_{q_2q_3} + \delta_{q_1q_3}\ \delta_{q_2q_4})\ . \tag{69}$$

Using Equations (56) - (58), (60), (61) and (64) - (69), the second term of Equation (53) becomes

$$-\frac{1}{\hbar^2}\int_o^t dt_1 \int_o^{t_1} dt_2 <TV(t_1)V(t_2)>_{ca} = \frac{1}{8\hbar^2}\{\sum_q V_{qq}\ (2\bar{n}_q+1)\}^2 t^2$$

$$-\frac{1}{\hbar^2}\int_o^t dt_1 \int_o^{t_1} dt_2 \Big[\sum_{q_1q_3} \{V_{q_1}V^*_{q_3}\, e^{-i\omega_{q_1}t_1}\, e^{i\omega_{q_3}t_2}\ (\bar{n}_{q_1}+1)\delta_{q_1q_3}$$

$$+ V^*_{q_1}V_{q_3}\, e^{i\omega_{q_1}t_1}\, e^{-i\omega_{q_3}t_2}\ \bar{n}_{q_1}\delta_{q_1q_3}\}$$

$$+ \tfrac{1}{4}\sum_{q_1q_2q_3q_4} V_{q_1q_2}\ V_{q_3q_4}\ \{e^{-i(\omega_{q_1}+\omega_{q_2})t_1}\, e^{i(\omega_{q_3}+\omega_{q_4})t_2}\ (\bar{n}_{q_1}+1)(\bar{n}_{q_2}+1)$$

$$x\ (\delta_{q_1q_3}\ \delta_{q_2q_4} + \delta_{q_1q_4}\ \delta_{q_2q_3})$$

$$+ e^{i(\omega_{q_1}-\omega_{q_2})t_1}\, e^{i(\omega_{q_3}-\omega_{q_4})t_2}\ (\bar{n}_{q_1}\bar{n}_{q_3}\delta_{q_1q_2}\delta_{q_3q_4} + n_{q_1}(\bar{n}_{q_2}+1)\delta_{q_1q_4}\delta_{q_2q_3}$$

$$+ e^{i(\omega_{q_1}-\omega_{q_2})t_1}\, e^{-i(\omega_{q_3}-\omega_{q_4})t_2}\ (\bar{n}_{q_1}(\bar{n}_{q_3}+1)\ \delta_{q_1q_2}\delta_{q_3q_4} + \bar{n}_{q_1}(\bar{n}_{q_2}+1)$$

$$\delta_{q_1q_3}\ \delta_{q_2q_4})$$

$$+ e^{-i(\omega_{q_1}-\omega_{q_2})t_1}\, e^{i(\omega_{q_3}-\omega_{q_4})t_2}\ ((\bar{n}_{q_1}+1)\ \bar{n}_{q_3}\ \delta_{q_1q_2}\ \delta_{q_3q_4} + (\bar{n}_{q_1}+1)\bar{n}_{q_2}$$

$$\delta_{q_1q_3}\ \delta_{q_2q_4})$$

$$+ e^{-i(\omega_{q_1}-\omega_{q_2})t_1} e^{-i(\omega_{q_3}-\omega_{q_4})t_2} ((\bar{n}_{q_1}+1)(\bar{n}_{q_3}+1) \delta_{q_1q_2} \delta_{q_3q_4} + (\bar{n}_{q_1}+1)\bar{n}_{q_2} \delta_{q_1q_4} \delta_{q_2q_3})$$

$$+ e^{i(\omega_{q_1}+\omega_{q_2})t_1} e^{-i(\omega_{q_3}+\omega_{q_4})t_2} \bar{n}_{q_1} \bar{n}_{q_2} (\delta_{q_1q_4} \delta_{q_2q_3} + \delta_{q_1q_3} \delta_{q_2q_4})\}]$$

$$= \frac{1}{8\hbar^2} \{\sum_q V_{qq} (2\bar{n}_q+1)\}^2 t^2$$

$$- \frac{1}{\hbar^2} \sum_{q_1} (V_{q_1})^2 \{(\bar{n}_{q_1}+1) \int_0^t dt_1 \int_0^{t_1} dt_2 \, e^{-i\omega_{q_1}t_1} e^{i\omega_{q_1}t_2} + n_{q_1} \int_0^t dt_1 \int_0^{t_1} dt_2 \, e^{i\omega_{q_1}t_1} e^{-i\omega_{q_1}t_2}\}$$

$$- \frac{1}{4\hbar^2} [\sum_{q_1q_2} \{V_{q_1q_2} V_{q_1q_2} (\bar{n}_{q_1}+1)(\bar{n}_{q_2}+1) \int_0^t dt_1 \int_0^{t_1} dt_2 \, e^{-i(\omega_{q_1}+\omega_{q_2})t_1} e^{+i(\omega_{q_1}+\omega_{q_2})t_2}$$

$$+ V_{q_1q_2} V_{q_2q_1} (\bar{n}_{q_1}+1)(\bar{n}_{q_2}+1) \int_0^t dt_1 \int_0^{t_1} dt_2 \, e^{-i(\omega_{q_1}+\omega_{q_2})t_1} e^{+i(\omega_{q_2}+\omega_{q_1})t_2}\}$$

$$+ \sum_{q_1q_3} V_{q_1q_1} V_{q_3q_3} \bar{n}_{q_1} \bar{n}_{q_3} \int_0^t dt_1 \int_0^{t_1} dt_2 + \sum_{q_1q_2} V_{q_1q_2} V_{q_2q_1} \bar{n}_{q_1} (\bar{n}_{q_2}+1) \int_0^t dt_1 \int_0^{t_1} dt_2 \, e^{i(\omega_{q_1}-\omega_{q_2})t_1} e^{-i(\omega_{q_1}-\omega_{q_2})t_2}$$

$$+ \sum_{q_1q_3} V_{q_1q_3} V_{q_3q_3} \bar{n}_{q_1} (\bar{n}_{q_3}+1) \int_0^t dt_1 \int_0^{t_1} dt_2 + \sum_{q_1q_2} V_{q_1q_2} V_{q_1q_2} \bar{n}_{q_1}$$

$$(\bar{n}_{q_2}+1) \int_0^t dt_1 \int_0^{t_1} dt_2 \, e^{i(\omega_{q_1}-\omega_{q_2})t_2} \, e^{-i(\omega_{q_1}-\omega_{q_2})t_2}$$

$$+ \sum_{q_1q_3} V_{q_1q_1} V_{q_3q_3} (\bar{n}_{q_1}+1)\bar{n}_{q_3} \int_0^t dt_1 \int_0^{t_1} dt_2 + \sum_{q_1q_2} V_{q_1q_2} V_{q_1q_2}$$

$$(\bar{n}_{q_1}+1)\bar{n}_{q_2} \int_0^t dt_1 \int_0^{t_1} dt_2 \, e^{-i(\omega_{q_1}-\omega_{q_2})t_1} \, e^{i(\omega_{q_1}-\omega_{q_2})t_2}$$

$$+ \sum_{q_1q_3} V_{q_1q_1} V_{q_3q_3} (\bar{n}_{q_1}+1)(\bar{n}_{q_3}+1) \int_0^t dt_1 \int_0^{t_1} dt_2 + \sum_{q_1q_2} V_{q_1q_2} V_{q_2q_1}$$

$$(\bar{n}_{q_1}+1)\bar{n}_{q_2} \int_0^t dt_1 \int_0^{t_1} dt_2 \, e^{-i(\omega_{q_1}-\omega_{q_2})t_1} \, e^{i(\omega_{q_1}-\omega_{q_2})t_2}$$

$$+ \sum_{q_1q_2} V_{q_1q_2} V_{q_2q_1} \bar{n}_{q_1}\bar{n}_{q_2} \int_0^t dt_1 \int_0^{t_1} dt_2 \, e^{i(\omega_{q_1}+\omega_{q_2})t_1} \, e^{-i(\omega_{q_1}+\omega_{q_2})t_2}$$

$$+ \sum_{q_1q_2} V_{q_1q_2} V_{q_1q_2} \bar{n}_{q_1}\bar{n}_{q_2} \int_0^t dt_1 \int_0^{t_1} dt_2 \, e^{i(\omega_{q_1}+\omega_{q_2})t_1} \, e^{-i(\omega_{q_1}+\omega_{q_2})t_2}]$$

$$= \frac{1}{8\hbar^2} \{\sum_q V_{qq} (2\bar{n}_q+1)\}^2 t^2 - \frac{1}{2\hbar^2} \sum_{q_1} (V_{q_1})^2 \{(\bar{n}_{q_1}+1)(\frac{1}{\omega_{q_1}^2} - \frac{1}{\omega_{q_1}} it$$

$$- \frac{1}{\omega_{q_1}^2} e^{-i\omega_{q_1}t}) + \bar{n}_{q_1} (\frac{1}{\omega_{q_1}^2} + \frac{1}{\omega_{q_1}} it - \frac{1}{\omega_{q_1}^2} e^{i\omega_{q_1}t})\}$$

$$- \frac{1}{4\hbar^2} \Big[\sum_{q_1 q_2} V_{q_1 q_2} V_{q_1 q_2} (\bar{n}_{q_1}+1)(\bar{n}_{q_2}+1) \Big\{ \frac{1}{(\omega_{q_1}+\omega_{q_2})^2} - \frac{1}{\omega_{q_1}+\omega_{q_2}}\, it - \frac{e^{-i(\omega_{q_1}+\omega_{q_2})t}}{(\omega_{q_1}+\omega_{q_2})^2}) \Big\}$$

$$+ \sum_{q_1 q_2} V_{q_1 q_2} V_{q_2 q_1} (\bar{n}_{q_1}+1)(\bar{n}_{q_2}+1) \Big\{ \frac{1}{(\omega_{q_1}+\omega_{q_2})^2} - \frac{1}{\omega_{q_1}+\omega_{q_2}}\, it - \frac{e^{-i(\omega_{q_1}+\omega_{q_2})t}}{(\omega_{q_1}+\omega_{q_2})^2} \Big\}$$

$$+ \sum_{q_1 q_2} V_{q_1 q_1} V_{q_2 q_2} \bar{n}_{q_1} \bar{n}_{q_2} \frac{t^2}{2} + \sum_{q_1 q_2} V_{q_1 q_2} V_{q_2 q_1} \bar{n}_{q_1} (\bar{n}_{q_2}+1)$$

$$\times \Big\{ \frac{1}{(\omega_{q_1}-\omega_{q_2})^2} + \frac{1}{(\omega_{q_1}-\omega_{q_2})}\, it - \frac{e^{i(\omega_{q_1}-\omega_{q_2})t}}{(\omega_{q_1}-\omega_{q_2})^2} \Big\}$$

$$+ \sum_{q_1 q_2} V_{q_1 q_1} V_{q_2 q_2} \bar{n}_{q_1} (\bar{n}_{q_2}+1) \frac{t^2}{2} + \sum_{q_1 q_2} V_{q_1 q_2} V_{q_1 q_2} \bar{n}_{q_1} (\bar{n}_{q_2}+1)$$

$$\times \Big\{ \frac{1}{(\omega_{q_1}-\omega_{q_2})^2} + \frac{1}{(\omega_{q_1}-\omega_{q_2})}\, it - \frac{e^{i(\omega_{q_1}-\omega_{q_2})t}}{(\omega_{q_1}-\omega_{q_2})^2} \Big\}$$

$$+ \sum_{q_1 q_2} V_{q_1 q_1} V_{q_2 q_2} (\bar{n}_{q_1}+1) \bar{n}_{q_2} \frac{t^2}{2} + \sum_{q_1 q_2} V_{q_1 q_2} V_{q_1 q_2} (\bar{n}_{q_1}+1) \bar{n}_{q_2}$$

$$\times \Big\{ \frac{1}{(\omega_{q_1}-\omega_{q_2})^2} - \frac{1}{(\omega_{q_1}-\omega_{q_2})}\, it - \frac{e^{-i(\omega_{q_1}-\omega_{q_2})t}}{(\omega_{q_1}-\omega_{q_2})^2} \Big\}$$

$$+ \sum_{q_1q_2} V_{q_1q_1} V_{q_2q_2} (\bar{n}_{q_1}+1)(\bar{n}_{q_2}+1) \frac{t^2}{2} + \sum_{q_1q_2} V_{q_1q_2} V_{q_2q_1} (\bar{n}_{q_1}+1)\bar{n}_{q_2}$$

$$\times \{\frac{1}{(\omega_{q_1}-\omega_{q_2})^2} - \frac{1}{(\omega_{q_1}-\omega_{q_2})} it - \frac{e^{-i(\omega_{q_1}-\omega_{q_2})t}}{(\omega_{q_1}-\omega_{q_2})^2}\}$$

$$+ \sum_{q_1q_2} V_{q_1q_2} V_{q_2q_1} \bar{n}_{q_1} \bar{n}_{q_2} \{\frac{1}{(\omega_{q_1}+\omega_{q_2})^2} + \frac{1}{(\omega_{q_1}+\omega_{q_2})} it - \frac{e^{i(\omega_{q_1}+\omega_{q_2})t}}{(\omega_{q_1}+\omega_{q_2})^2}\}$$

$$+ \sum_{q_1q_2} V_{q_1q_2} V_{q_1q_2} \bar{n}_{q_1} \bar{n}_{q_1} \{\frac{1}{(\omega_{q_1}+\omega_{q_2})^2} + \frac{1}{(\omega_{q_1}+\omega_{q_2})} it - \frac{e^{i(\omega_{q_1}+\omega_{q_2})t}}{(\omega_{q_1}+\omega_{q_2})^2}\}]. \tag{70}$$

We changed dummy variable q_2 to q_3 in Equation (70). Since t^2 terms are cancelled each other, all the terms of Equations (70) and (55) can be collected and Equation (53) can be expressed as

$$g(t) = - S - it\Omega + i\omega_o t + g_1(t) + g_2(t) , \tag{71}$$

where

$$S = \sum_{q_1} \frac{(V_{q_1})^2}{(\hbar\omega_{q_1})^2} (2\bar{n}_{q_1}+1) , \tag{72}$$

$$\Omega = \frac{1}{2\hbar} \sum_q V_{qq} (2\bar{n}_q+1) - \frac{1}{\hbar^2} \sum_{q_1} (V_{q_1})^2 \frac{1}{\omega_{q_1}}$$

$$- \frac{1}{2\hbar^2} \sum_{q_1q_2} (V_{q_1q_2})^2 [\frac{\bar{n}_{q_1}+\bar{n}_{q_2}+1}{\omega_{q_1}+\omega_{q_2}} + \frac{\bar{n}_{q_2}-\bar{n}_{q_1}}{\omega_{q_1}-\omega_{q_2}}] , \tag{73}$$

$$g_1(t) = \frac{1}{\hbar^2} \sum_{q_1} \frac{(V_{q_1})^2}{\omega_{q_1}^2} \{(\bar{n}_{q_1}+1)\, e^{-i\omega_{q_1} t} + \bar{n}_{q_1}\, e^{i\omega_{q_1} t}\} \tag{74}$$

$$g_2(t) = \frac{1}{2\hbar^2} \sum_{q_1 q_2} \frac{(V_{q_1 q_2})^2}{(\omega_{q_1}+\omega_{q_2})^2} \{(\bar{n}_{q_1}+1)(\bar{n}_{q_2}+1)(1 - e^{-i(\omega_{q_1}+\omega_{q_2})t})$$

$$+ \bar{n}_{q_1}\bar{n}_{q_2}\, (1 - e^{i(\omega_{q_1}+\omega_{q_2})t})\}$$

$$- \frac{1}{\hbar^2} \sum_{q_1 q_2} \frac{(V_{q_1 q_2})^2}{(\omega_{q_1}-\omega_{q_2})^2} (\bar{n}_{q_1}+1)\, \bar{n}_{q_1}\, (1 - e^{-i(\omega_{q_1}-\omega_{q_2})t}) \, . \tag{75}$$

Notice that since q_1 and q_2 are arbitrary subscripts we used following relation:

$$\sum_{q_1 q_2} V_{q_1 q_2} V_{q_2 q_1} \bar{n}_{q_1} (\bar{n}_{q_2}+1) \{\frac{1}{(\omega_{q_1}-\omega_{q_2})^2} - \frac{e^{i(\omega_{q_1}-\omega_{q_2})t}}{(\omega_{q_1}-\omega_{q_2})^2}\}$$

$$= \sum_{q_1 q_2} V_{q_1 q_2} V_{q_2 q_1} (\bar{n}_{q_1}+1)\bar{n}_{q_2} \{\frac{1}{(\omega_{q_1}-\omega_{q_2})^2} - \frac{e^{-i(\omega_{q_1}-\omega_{q_2})t}}{(\omega_{q_1}-\omega_{q_2})^2}\} \, . \tag{76}$$

Therefore, we can rewrite the emission probability of Equation (47) as

$$P_{ab} = C\, \omega^3 |M_{ab}|^2\, G(ab;\omega),$$

where

$$G(ab;\omega) = \int_{-\infty}^{\infty} dt\, e^{-i\omega t}\, e^{g(t)}, \tag{77}$$

and

$$g(t) = -S - it\Omega + i\omega_0 t + g_1(t) + g_2(t),$$

where S, Ω, $g_1(t)$ and $g_2(t)$ are given in Equations (72) - (75).

In general the quadratic coupling term $g_2(t)$ is important only in the contribution it makes to the temperature dependence of the zero-phonon line and we will discuss it further in Chapter V. The linear coupling term $g_1(t)$ is important in analyzing vibronic sidebands. Since the structure in the experimentally observed sidebands is sharpest at very low temperatures this is the most interesting data to consider. Thus the theoretical expressions can be used in the limit T=0. In this limit only phonon emission occurs since $\bar{n}_q(\omega_q)$ equals zero. The expressions describing the spectral distribution function from Equations (71) through (74) and (77) are then

$$S = \sum_q \frac{V_q^{\,2}}{(\hbar\omega_q)^2} = \sum_q S_q, \tag{78}$$

$$\Omega = 0, \tag{79}$$

$$g_1(t) = \sum_q S_q\, e^{-i\omega_q t}, \tag{80}$$

$$G_B(ab;\omega) \approx e^{-S} \int_{-\infty}^{\infty} dt\, e^{-i(\omega-\omega_0)t}\, [e^{g_1(t)} - 1] . \tag{81}$$

Multiphonon processes will simply be represented by the product of terms such as that appearing in Equation (81). This can be expressed by expanding $(e^{g_1(t)} - 1)$ in a power series

$$G_B(ab;\omega) = \sum_{n=1}^{\infty} [e^{-S} \int_{-\infty}^{\infty} dt\, e^{-i(\omega-\omega_o)t} \frac{[g_1(t)]^n}{n!}]$$

$$= \sum_{n=1}^{\infty} G_n(ab;\omega), \tag{82}$$

where

$$G_n(ab;\omega) = e^{-S} \int_{-\infty}^{\infty} dt\, e^{-i(\omega-\omega_o)t} \frac{[g_1(t)]^n}{n!} . \tag{83}$$

One-phonon processes are then given by

$$G_1(ab;\omega) = e^{-S} \int_{-\infty}^{\infty} dt\, e^{-i(\omega-\omega_o)t} g_1(t)$$

$$= e^{-S} \sum_q S_q \int_{-\infty}^{\infty} dt\, e^{-i(\omega-\omega_o+\omega_q)t}$$

$$= 2\pi e^{-S} \sum_q S_q\, \delta(\omega_o-\omega-\omega_q) , \tag{84}$$

and the n-phonon contribution to the spectrum becomes

$$G_n(ab;\omega) = e^{-S} \int_{-\infty}^{\infty} dt\, e^{-i(\omega-\omega_o)t} \frac{1}{n!} (\sum_q S_q\, e^{-i\omega_q t})^n$$

$$= \frac{e^{-S}}{n!} \int_{-\infty}^{\infty} dt\, e^{-i(\omega-\omega_o)t} \sum_q S_q\, e^{-i\omega_q t} (\sum_q S_q\, e^{-i\omega_q t})^{n-1}$$

$$= \frac{2\pi e^{-S}}{n!} \int_{-\infty}^{\infty} d\omega_1 \cdots d\omega_n \frac{e^S G_1(ab;\omega_1)}{2\pi} \cdots \frac{e^S G_1(ab;\omega_n)}{2\pi}$$

$$\delta[(\omega_o-\omega) - \sum_{m=1}^{n} (\omega_o-\omega_m)] . \tag{85}$$

This can be written in a simpler form which can be understood by looking explicitly at the first two terms n = 1, and n = 2,

$$G_1(ab;\omega) = \frac{2\pi e^{-S}}{1!} \int_{-\infty}^{\infty} d\omega_1 \; \frac{e^S G_1(ab;\omega_1)}{2\pi} \, \delta[(\omega_o-\omega) - (\omega_o-\omega_1)]$$

$$= \frac{2\pi e^{-S}}{1!} \frac{e^S}{2\pi} G_1(ab;\omega) = 2\pi e^{-S} \sum_q \frac{S_q}{1!} \delta[(\omega_o-\omega)-\omega_q] \; .$$

$$G_2(ab;\omega) = \frac{2\pi e^{-S}}{2!} \int_{-\infty}^{\infty} \int_{-\infty}^{\infty} d\omega_1 \, d\omega_2 \, \frac{e^S G(ab;\omega_1)}{2\pi} \, \frac{e^S G_1(ab;\omega_2)}{2\pi} \, \delta(\omega_1+\omega_2 - \omega_o-\omega)$$

$$= \frac{2\pi e^{-S}}{2!} \sum_q S_q \int_{-\infty}^{\infty} d\omega_1 \, \delta[(\omega_o-\omega_1)-\omega_q] \, \frac{e^S}{2\pi} G_1(ab;\omega_o+\omega-\omega_1)$$

$$= 2\pi e^{-S} \sum_{qq'} \frac{S_q}{1!} \, \frac{S_{q'}}{2!} \, \delta[(\omega_o-\omega) - (\omega_q+\omega_{q'})] \; .$$

Thus, for an nth order process this can be generalized to

$$G_n(ab;\omega) = 2\pi e^{-S} \sum_{\{n_q \geq 0\}} \delta_{n,\sum_q n_q} \left(\prod_q \frac{S_q^{\,n_q}}{\;}\right) \delta[(\omega_o-\omega) - \sum_q n_q\omega_q]. \qquad (86)$$

Note that the ratio of the integrated intensity of the n-phonon spectrum to that of the total broad band spectrum can be expressed as

$$\frac{\int_{-\infty}^{\infty} d\omega \, G_n(ab;\omega)}{\int_{-\infty}^{\infty} d\omega \, G_B(ab;\omega)} = \frac{\int_{-\infty}^{\infty} d\omega \, e^{-S} \int_{-\infty}^{\infty} dt \, e^{-i(\omega-\omega_o)t} \, \frac{[g_1(t)]^n}{n!}}{\sum_{n=1}^{\infty} \int_{-\infty}^{\infty} d\omega \int_{-\infty}^{\infty} dt \, e^{-S} \, e^{-i(\omega-\omega_o)t} \, \frac{[g_1(t)]^n}{n!}} = \frac{2\pi e^{-S} \; (S^n/n!)}{2\pi e^{-S} \sum_{n=1}^{\infty} (S^n/n!)}$$

$$= \frac{S^n}{n!} \, \frac{1}{\sum_{n=0}^{\infty} \frac{S^n}{n!} - 1} = \frac{S^n}{n!} \, \frac{1}{e^S - 1} = \frac{S^n}{n!} \, \frac{e^{-S}}{1-e^{-S}} \; . \qquad (87)$$

Although we have been neglecting the zero-phonon line for simplicity this expression also holds for n=0. Thus the area under the zero-phonon line divided by the area of the total spectra can be used to determine the Huang-Rhys factor at T=0.

Computer Analysis of the Vibronic Sideband

The first step in understanding an observed vibronic sideband is to separate it into its one-phonon, two-phonon, and all other n-phonon contributions. For this purpose some type of iterative procedure is required since $G_1(ab;\omega_q)$ is needed to generate the other $G_n(ab;\omega_q)$ contributions. To do this one assumes a trial one-phonon spectrum which can be obtained in several ways such as from the density of states obtained from neutron scattering data. For the case of interest here the majority of the structure observed in the low temperature vibronic sideband is divided into 10^{23} equally spaced "phonon modes" with individual mode Huang-Rhys factors proportional to the spectral intensity at that frequency. The sideband is then represented by a series of equally spaced delta functions normalized to the total Huang-Rhys factor

$$S(\omega_q) = \sum_q S_q \, \delta(\omega_q - q\Delta) \; . \tag{88}$$

Thus the experimental values for the S_q's and the frequency interval Δ are the only important inputs for the computer calculations. The one-phonon spectrum is then given by Equation (84) and the next few higher order spectra are obtained from the convolution of this spectrum according to Equation (85). The total spectral profile is then just the sum of the $G_n(ab;\omega)$ for all n-phonon processes which make non-negligible contributions to the results. The computer predicted band $G_B(ab;\omega_q)$ is then compared with the experimental data and if the fit is not satisfactory an iteration process is employed to obtain a more accurate predicted sideband. This is done with the equations

$$G_1^{new}(\omega_q) = \tfrac{1}{2}\{G_B^{exp}(\omega_q) + AG_B^{old}(\omega_q)\} \quad \text{for} \quad q_1 \leq q \leq 2q_1-1,$$

$$G_1^{new}(\omega_q) = \tfrac{1}{2}\{G_B^{exp}(\omega_q) + AG_B^{old}(\omega_q)\} - \{1 + \frac{q - 2q_1}{q_2 - 2q_1}(A - 1)\}$$

$$\{G_B^{old}(\omega_q) - G_1^{old}(\omega_q)\} \quad \text{for} \quad 2q_1 < q \leq q_2 \, , \qquad (89)$$

where

$$A = \frac{G_B^{exp}(\omega_{q_2} + 1)}{G_B^{old}(\omega_{q_2} + 1)}$$

and q_1 and q_2 are the lowest and highest frequency countings of the one-phonon side band. Equation (89) gives a new trial function $G_1^{new}(\omega_q)$ to be used as the one-phonon spectrum in the convolution process. The iteration process is repeated until a suitable fit is obtained and the computer then plots the final predicted spectral profile and each of the n-phonon contributions to the total spectrum. The results are plotted by connecting consecutive points with straight lines. Even though the convolution process is good enough to get the reasonable fit to the experimental data in our case, other cases may need to use moment analysis to get the higher n-phonon emission spectra at T=0. In our program we use this moment analysis only to calculate the parameters for comparison with experiment. A discussion of moment analysis is given in the Appendix.

The computer program for the above procedure was developed by Mostoller, et al. (36) and the flow diagram for the program is shown in Figure 7.

The program starts to read the necessary control factors such as lowest and highest one-phonon frequencies, Huang-Rhys factors, number of phonons included, number of iterations desired, number of temperature steps for the zero-phonon line widths and positions, several plot control factors, and criterion factors whether to go to moment analysis or convolution processes or not. Then the X-axis (wave length) is set. Once the wave length is set the program reads the measured spectral function (G_B^{exp} $(ab;\omega_q)$) which is derived from measured spectral intensity divided by ω^3 because of the frequency factor in Equation (47). The main program then calls subroutine GMOMTS which normalizes G_B^{exp} $(ab;\omega_q)$ and calculates average frequency distribution and the root mean square phonon frequency distribution and other characteristic constants of G_B^{exp} $(ab;\omega_q)$ such as skewness (γ_1), excess (γ_2) and fifth cummulants (γ_3) by using Equations (A-3) - (A-12). These are only used for comparison with the calculations. Then the main program points out the normalized G_B^{exp} $(ab;\omega_q)$. For this fitting program we have to estimate the one-phonon side bands for which we simply use the experimental data out to 0.1397 ev. For the best fit we also need some consideration about the local mode which we will describe in detail later in local mode chapter.

Now the main program is actually in one part of the iteration loop. It prepares the iteration parameters (IFSHOW). Then the subroutine MOMENT is called. MOMENT calculates γ_1, γ_2, γ_3 and $\gamma_1(n)$, $\gamma_2(n)$ and $\gamma_3(n)$ at T=0 for all phonons for a given $G_1(ab;\omega_q)$ and computes the

Figure 7. Flow Chart of the Computer Program Used. The subroutines used in the main program do the following:

GMOMTS: Calculates the skewness, excess, and the fifth cumulants from the experimental spectral function.

MOMENT: For given one-phonon side band, calculates the characteristic constants such as skewness, etc. and temperature dependence of the line width, position and intensity of the zero-phonon line.

CONVOL: Generates n-phonon spectrum by convoluting one and (n-1) phonon spectrum.

GAUSKW: Calculates skewgaussian spectral function from the given constants (γ_1, γ_2, γ_3 and the normalization factor).

GBLOOP: Renormalizes the skewgaussian spectral function and W_{peak}, W_{width}, W_{plus}, W_{minus}.

PLOTG1: Plots the calculated n-phonon band and the broad bands.

PLOTG2: Plots one-phonon band as effective one-phonon and quadratic contribution part separately.

PLOTG3: Plots calculated and experimental broad band.

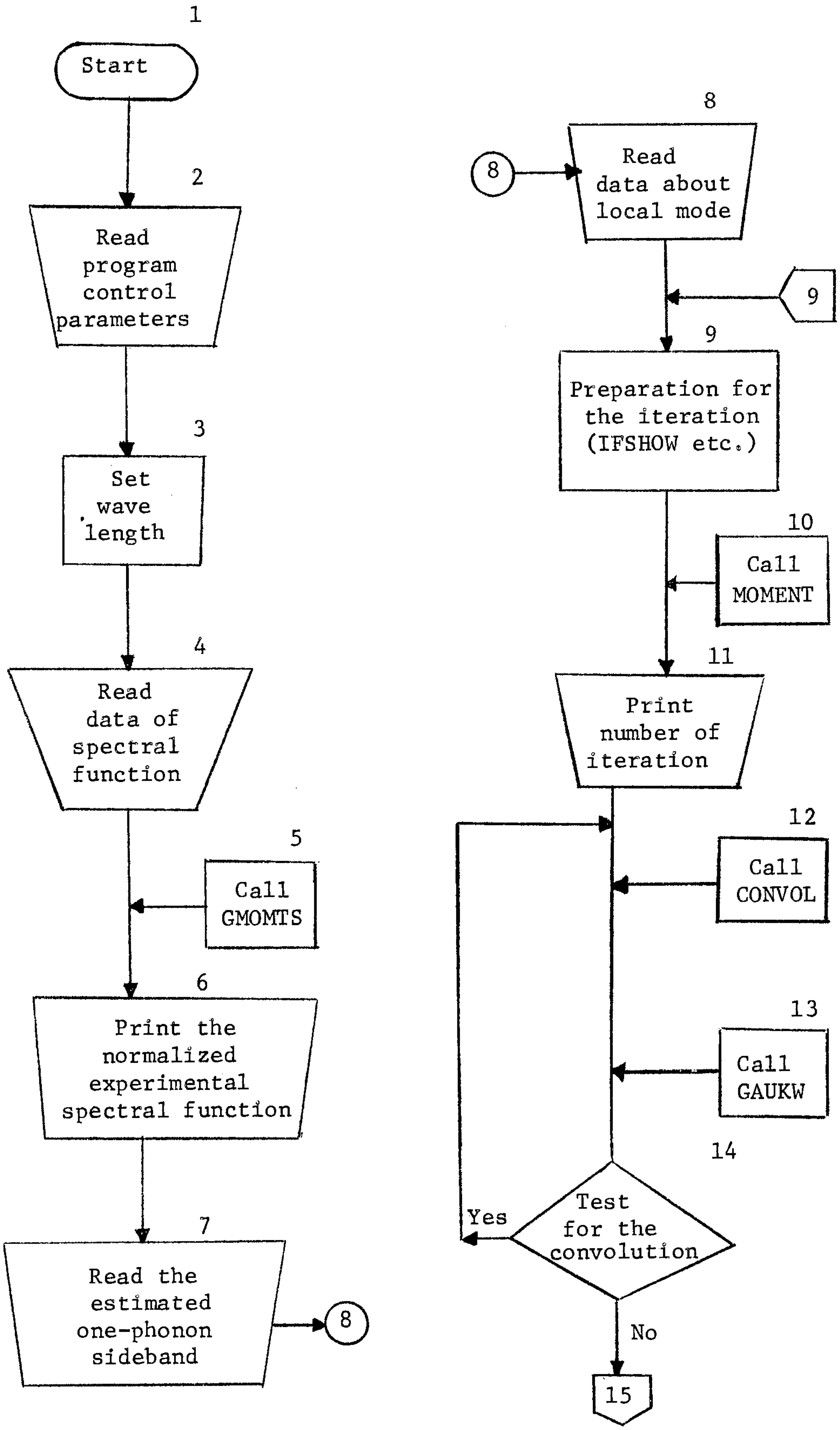
1
Start
2
Read program control parameters
3
Set wave length
4
Read data of spectral function
5
Call GMOMTS
6
Print the normalized experimental spectral function
7
Read the estimated one-phonon sideband
8
8
8
Read data about local mode
9
9
Preparation for the iteration (IFSHOW etc.)
10
Call MOMENT
11
Print number of iteration
12
Call CONVOL
13
Call GAUKW
14
Test for the convolution
Yes
No
15

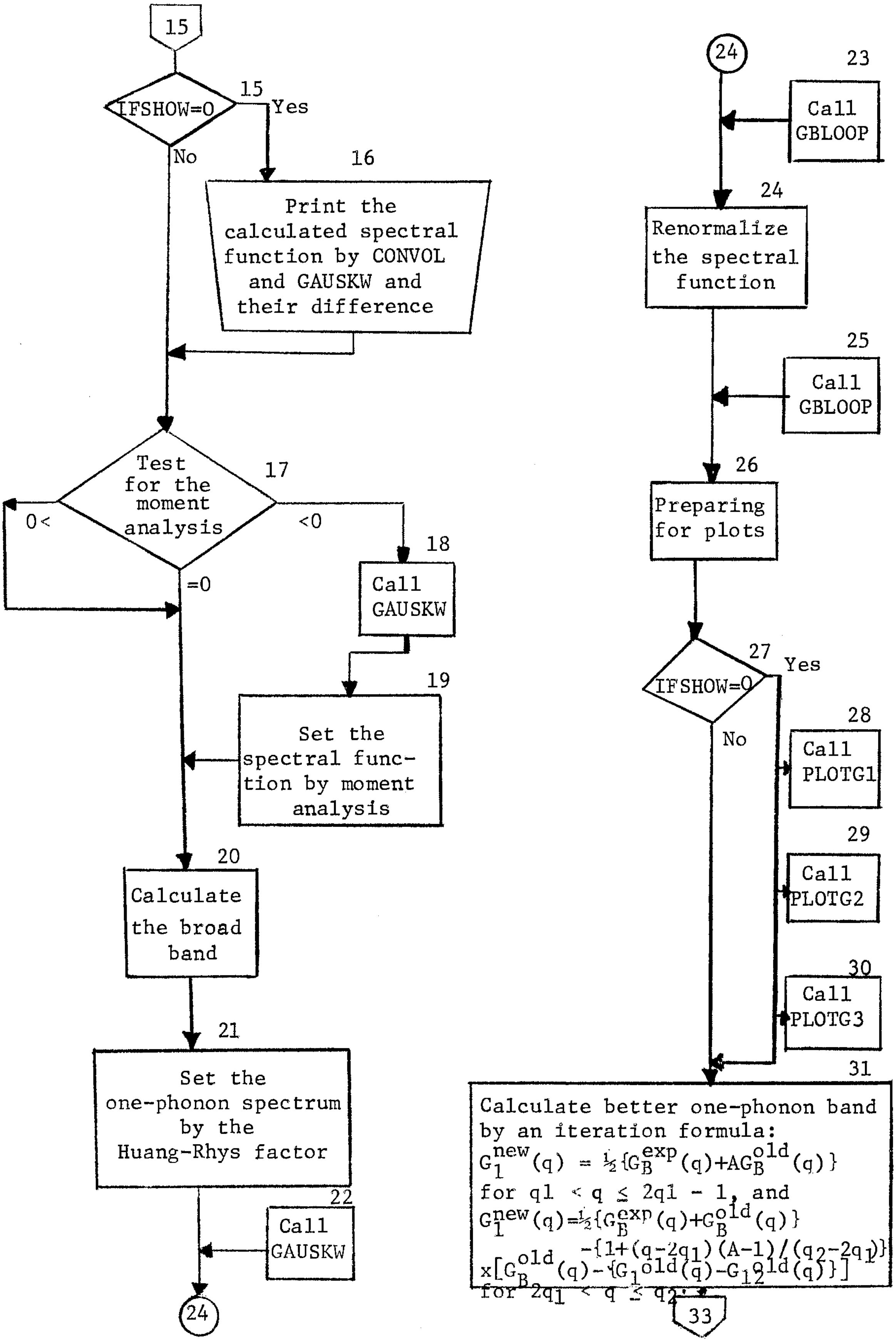
15
IFSHOW=0
15
Yes
No
16
Print the calculated spectral function by CONVOL and GAUSKW and their difference
Test for the moment analysis
17
0<
<0
=0
18
Call GAUSKW
19
Set the spectral function by moment analysis
20
Calculate the broad band
21
Set the one-phonon spectrum by the Huang-Rhys factor
22
Call GAUSKW
24
24
23
Call GBLOOP
24
Renormalize the spectral function
25
Call GBLOOP
26
Preparing for plots
27
IFSHOW=0
Yes
No
28
Call PLOTG1
29
Call PLOTG2
30
Call PLOTG3
31
Calculate better one-phonon band by an iteration formula:
$G_1^{new}(q) = \frac{1}{2}\{G_B^{exp}(q)+AG_B^{old}(q)\}$
for $q1 < q \leq 2q1 - 1$, and
$G_1^{new}(q)=\frac{1}{2}\{G_B^{exp}(q)+G_B^{old}(q)\}$
$-\{1+(q-2q_1)(A-1)/(q_2-2q_1)\}$
$x[G_B^{old}(q)-\{G_1^{old}(q)-G_{12}^{old}(q)\}]$
for $2q_1 < q \leq q_2$,
33

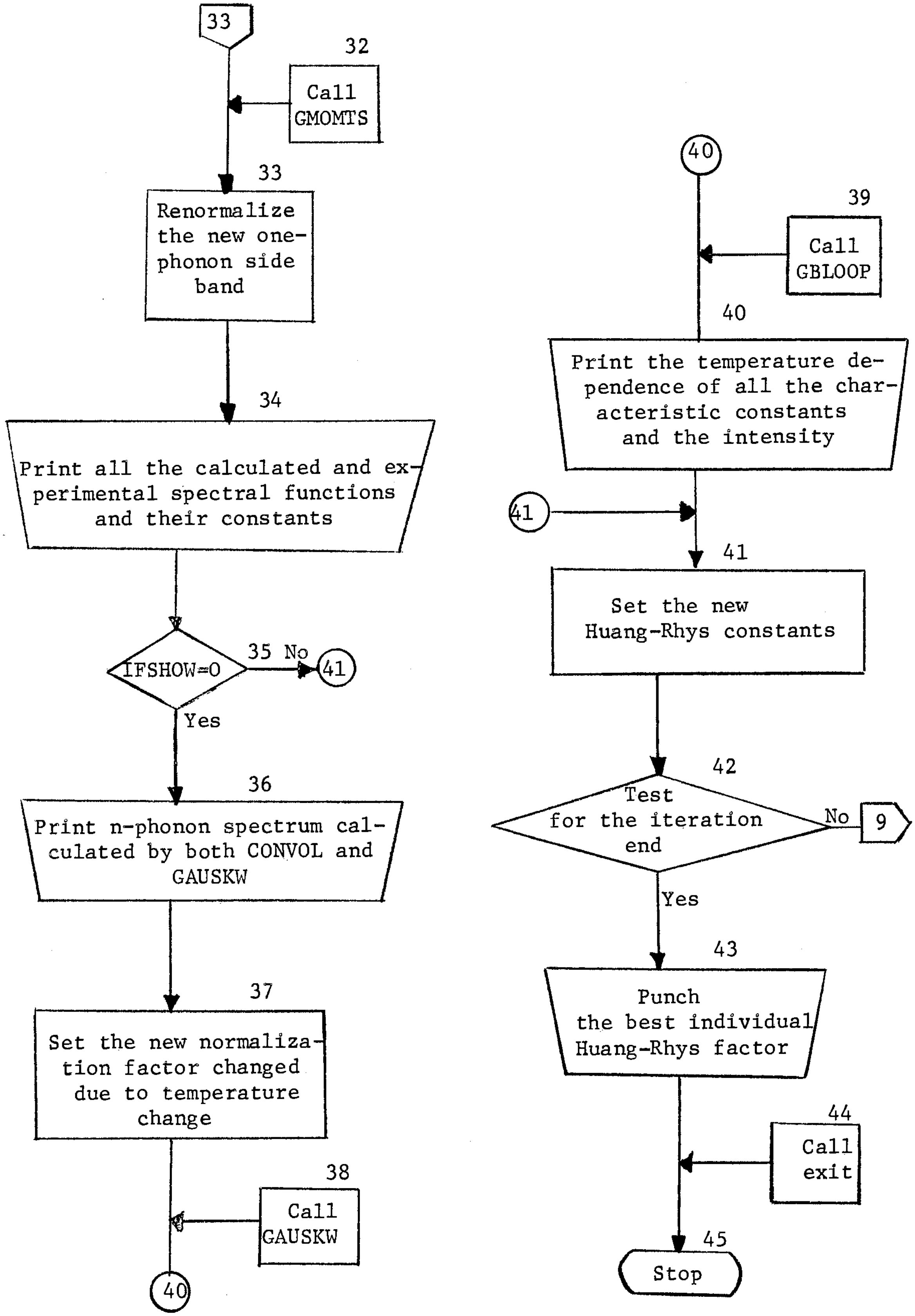
33
32
Call GMOMTS
33
Renormalize the new one-phonon side band
34
Print all the calculated and experimental spectral functions and their constants
IFSHOW=0
35 No
41
Yes
36
Print n-phonon spectrum calculated by both CONVOL and GAUSKW
37
Set the new normalization factor changed due to temperature change
38
Call GAUSKW
40
40
39
Call GBLOOP
40
Print the temperature dependence of all the characteristic constants and the intensity
41
41
Set the new Huang-Rhys constants
42
Test for the iteration end
No
9
Yes
43
Punch the best individual Huang-Rhys factor
44
Call exit
45
Stop

temperature dependence of the zero-phonon line positions, widths and the intensity for each iteration as we will describe later. After printing out the number of iterations the main program calls the subroutine CONVOL which generates G(I,J) = $G_n(ab;\omega_q)$ by convolutiong one and (n-1) phonon spectrum by Equation (85). Then the $G_n(ab;\omega_q)$ is compared with the skewgaussian of Equation (A-8) which is calculated by subroutine GAUSKW to decide whether the moment analysis is to be used or not. However, in our case we never go to the moment analysis because of the structured side bands. After the completion of the convolution the main program continues to calculate $G_B(ab;\omega_q) = G_1(ab;\omega_q) + G_2(ab;\omega_q) + G_3(ab;\omega_q)$ except the first and the last iteration processes which print out the last convoluted spectrum comparison with the calculated skewgaussian. Once the spectral function is readjusted by the Huang-Rhys factor the skewgaussian recalculated by the GAUSKW and is renormalized by the subroutine GBLOOP and calculates W_{peak}, W_{width}, W_{plus}, and W_{minus} for the later comparison. This means $G_n(ab;\omega_q)$ once again needs to renormalization because of the maximum value was changed. It is done by calling the GBLOOP which also recomputes W_{peak}, W_{width}, W_{plus}, and W_{minus}. Except the first and the last processes in which the $G_n(ab;\omega_q)$, GTOT(J) = $G_B(ab;\omega_q)$ and $G_1(ab;\omega_q) = G_{11}(ab;\omega_q) + G_{12}(ab;\omega_q)$, $G_B(ab;\omega_q) = G_B^{exp}(ab;\omega_q)$ are plotted, then $G_1^{new}(J)$ will be calculated by the Equation (89) for the better fit to the measured spectrum. Actually this is the main part of this program. Once $G_1^{new}(J)$ is generated, subroutine GMOMTS again calculates the moments parameters to compare with the experimental values before renormalizing the new calculated each Huang-Rhys factor. The program then prints out all the needed calculated and experimental values. It also sets the new Huang-Rhys factor for the next iteration processes. The main program also prints out the wavelength, calculated $G_n(ab;\omega_q)$, skewgaussian, and the total spectrum along with the temperature dependence of W_{peak}, W_{width}, W_{plus}, W_{minus} after calling GAUSKW and GBLOOP by setting the new individual Huang-Rhys factor.

This is the whole first iteration process. This iteration process will continue up to the satisfied fitting level which may be estimated by the outputs. After the whole iteration the main program will punch the newly calculated individual Huang-Rhys factors and complete the program execution.

CHAPTER III

EXPERIMENTAL EQUIPMENTS AND SAMPLES

The $SrTiO_3$ crystal doped with Cr^{3+} used in these experiments was grown at the National Lead Company. It contained 0.02% of Cr_2O_3 by weight. A sample was cut and polished with dimensions of 10.70 x 7.30 x 0.80 mm^3.

The apparatus used for the measurement of absorption spectra was a Cary Model 14 spectrophotometer. In the visible region a tungsten lamp was used as a source and a 1P28 photomultiplier tube as a detector. In the ultraviolet region (from 3500 Å down to 2500 Å) the source was changed to a hydrogen lamp. For the infrared region the tungsten lamp was the source and a lead sulfide cell was used as a detector. The spectrophotometer records the optical density as a function of wavelength.

The block diagram of the continuous fluorescence apparatus is shown in Figure 8. The monochrometer shown between the source and the sample is used only for excitation experiments. For studying continuous fluorescence spectra, the sample was illuminated with white light from a water cooled PEK AH-6 1000 W high pressure mercury arc lamp filtered through 4 cm of saturated $CuSO_4$ solution. The fluorescence emission was chopped at 2000 Hz and focused on to the entrance slit of a Spex Model 1704 one-meter scanning monochrometer. The monochrometer has a Czerny-Turner mount with the grating blazed at 5000 Å having a ruling of 1200 lines/mm. The signal was detected by an RCA C31034 photomultiplier tube

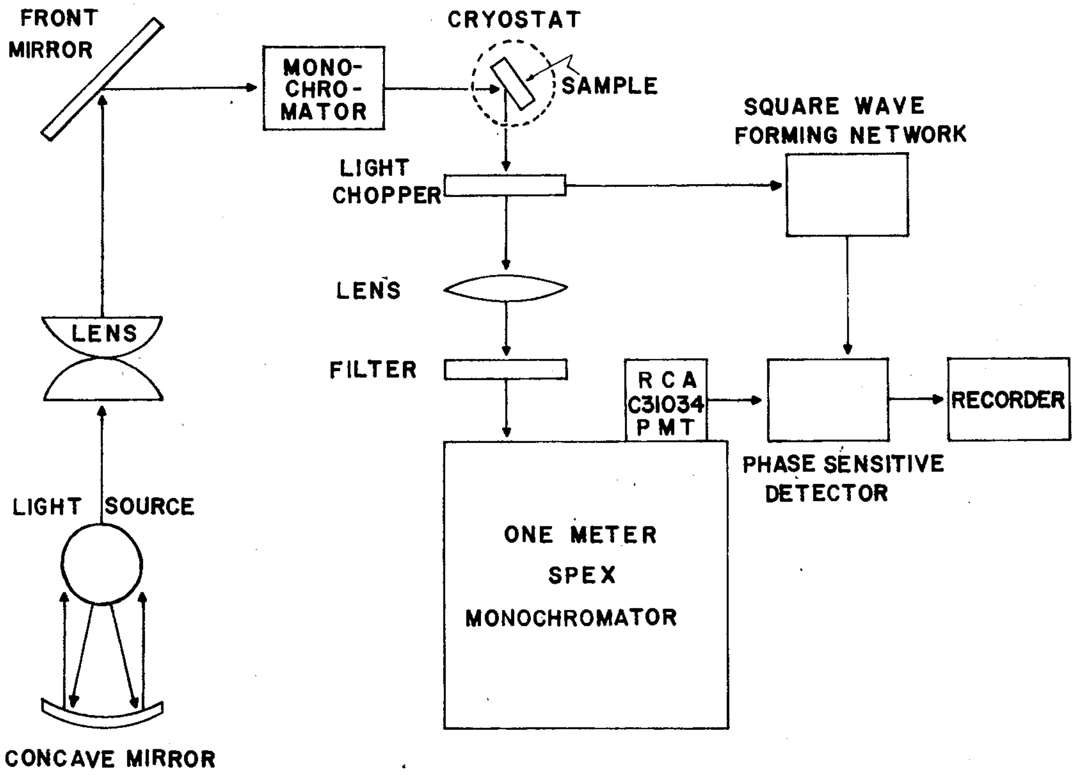
FRONT MIRROR
MONO-CHRO-MATOR
CRYOSTAT
SAMPLE
SQUARE WAVE FORMING NETWORK
LIGHT CHOPPER
LENS
LENS
FILTER
RCA C31034 PMT
RECORDER
PHASE SENSITIVE DETECTOR
LIGHT SOURCE
ONE METER SPEX MONOCHROMATOR
CONCAVE MIRROR

Figure 8. Block Diagram of the Continuous Fluorescence Measurement Apparatus

which was thermoelectrically cooled. The modulated signal was amplified by a Princeton Applied Research Model 128 lock-in amplifier tuned to the reference signal from the chopper. The amplified signal was displayed on the Heath Model EU-205-11 strip chart recorder. Absolute calibration of the detection system was accomplished with a quartz-iodine standard lamp. The response factor of the system determined from the calibration is shown in Figure 9.

For low temperature measurements the sample was mounted in an Air Products Displex Helium Refrigerator Model CS-202. By balancing the heat from a small electric heater installed on the cold finger of the cryostat against the removal of heat by the refrigerator, temperatures between 8^{o}K and room temperature could be obtained and held accurately for the needed periods of time. The temperature on the sample was measured with a gold-chrominel wires.

The time dependence of the fluorescence was monitored using the multichannel scaling technique shown in Figure 10. The sample was excited by a Xenon Corporation Model 457 Nanopulser with a repetition rate of approximately 40 Hz and a pulse width about 10.0 nsec. The exciting light was passed through a Schoeffel Instrument Corporation GM 100 grating monochrometer and the fluorescence light was passed through a Corning 2-64 color filter before being detected by a cooled RCA C31034 photomultiplier tube. Signals from the light pulser and phototube were sent to the start and counter terminals of a Nuclear Data 256 channel multichannel analyzer. The signal taken from the ninth stage dynode of the phototube was passed through a scintillation preamplifier, spectroscopic amplifier and a single channel analyzer set to pass only single photon events. The signal which was built up in the multichannel

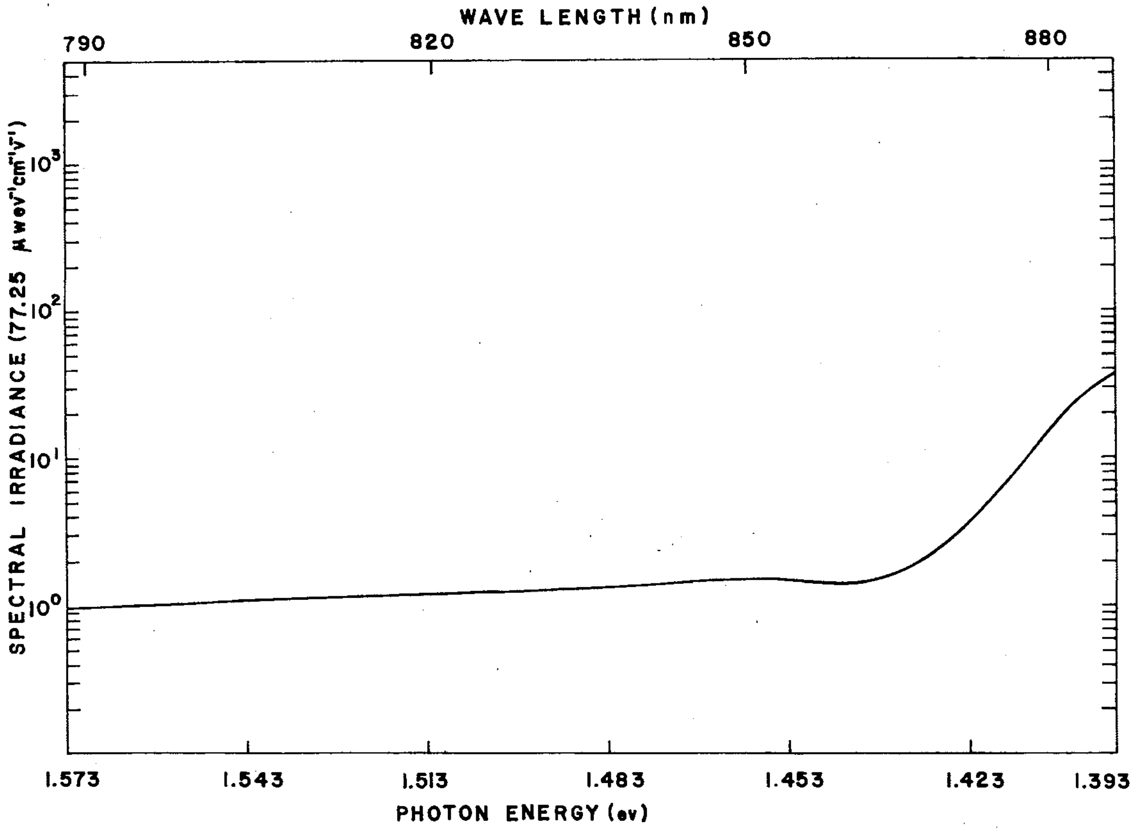

Figure 9. Response of Luminescence Detection System as a Function of Photon Energy

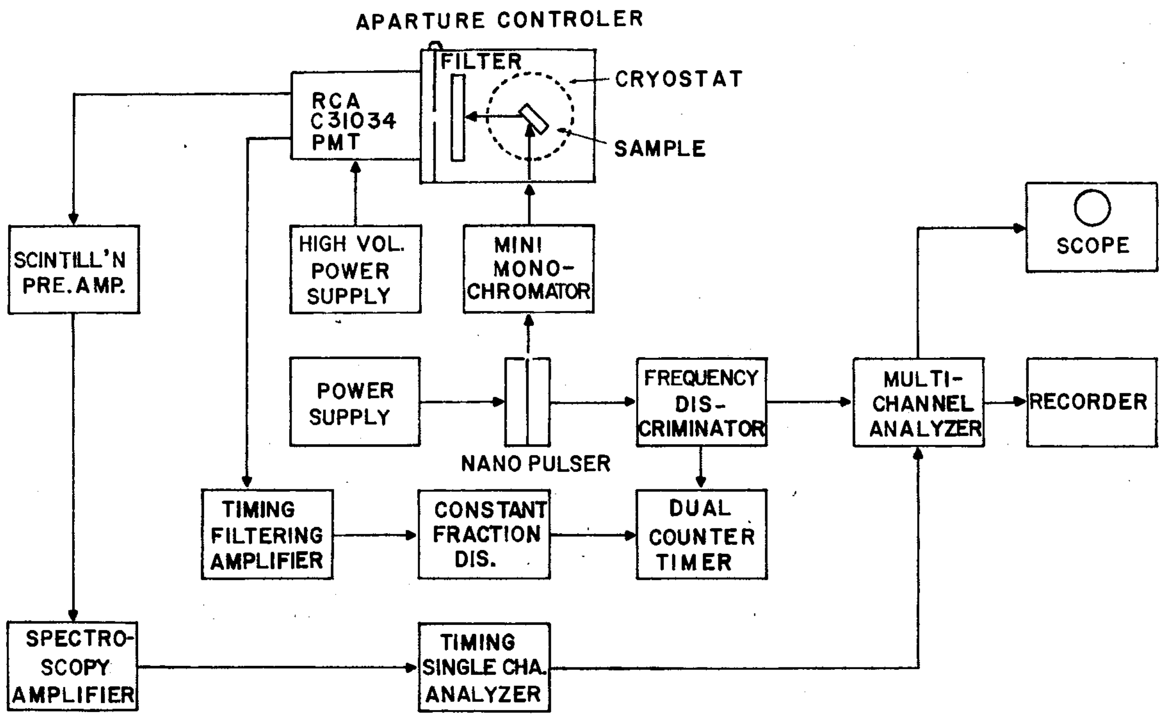
APARTURE CONTROLER
FILTER
CRYOSTAT
SAMPLE
RCA C31034 PMT
SCINTILL'N PRE.AMP.
HIGH VOL. POWER SUPPLY
MINI MONO-CHROMATOR
SCOPE
POWER SUPPLY
NANO PULSER
FREQUENCY DIS-CRIMINATOR
MULTI-CHANNEL ANALYZER
RECORDER
TIMING FILTERING AMPLIFIER
CONSTANT FRACTION DIS.
DUAL COUNTER TIMER
SPECTRO-SCOPY AMPLIFIER
TIMING SINGLE CHA. ANALYZER

Figure 10. Block Diagram of the Fluorescence Decay Time Measurement Apparatus

analyzer was recorded on a strip chart recorder. For the decay time measurements at low temperatures the sample was mounted in the same refrigerator as for the continuous fluorescence spectrum for the excitation by the Xenon Corporation Model 457 nanopulser.

CHAPTER IV

RESULTS AND INTERPRETATION--VIBRONIC SPECTRA

Figure 11 shows the fluorescence spectrum of $SrTiO_3:Cr^{3+}$ at about 8^oK and 150^oK. At low temperatures the sharp zero-phonon lines (R_1 and R_2) are split by about 4.08×10^{-4} eV whereas in the high temperature cubic phase only one R line appears. The low energy vibronic sideband appears as a series of peaks spread over 0.1530 eV from the R lines. The intense, sharp peaks at 1.4913 eV and 1.4203 eV are due to a local vibrational mode and its harmonic as discussed in the following chapter. The other structure can be associated with lattice phonons.

Low Energy Vibronics

Table VIII lists the energies for phonon modes in strontium titanate determined experimentally through infrared absorption, Raman scattering, neutron scattering, and vibronic spectroscopy. Since no structure is observed in the low energy vibronic sideband below 0.0124 eV only modes of this energy or greater are listed and modes of lower energy are discussed in the next section. Figure 12 shows the low energy vibronic spectra at 8^oK in comparison with neutron scattering dispersion curves of $SrTiO_3:Cr^{3+}$ and Raman and infrared data. The complete dispersion curves have been obtained only up to 0.0621 eV; however, a neutron scattering peak at the Γ-point has been observed at about 0.1023 eV. This mode is also seen in infrared spectra along with the four other

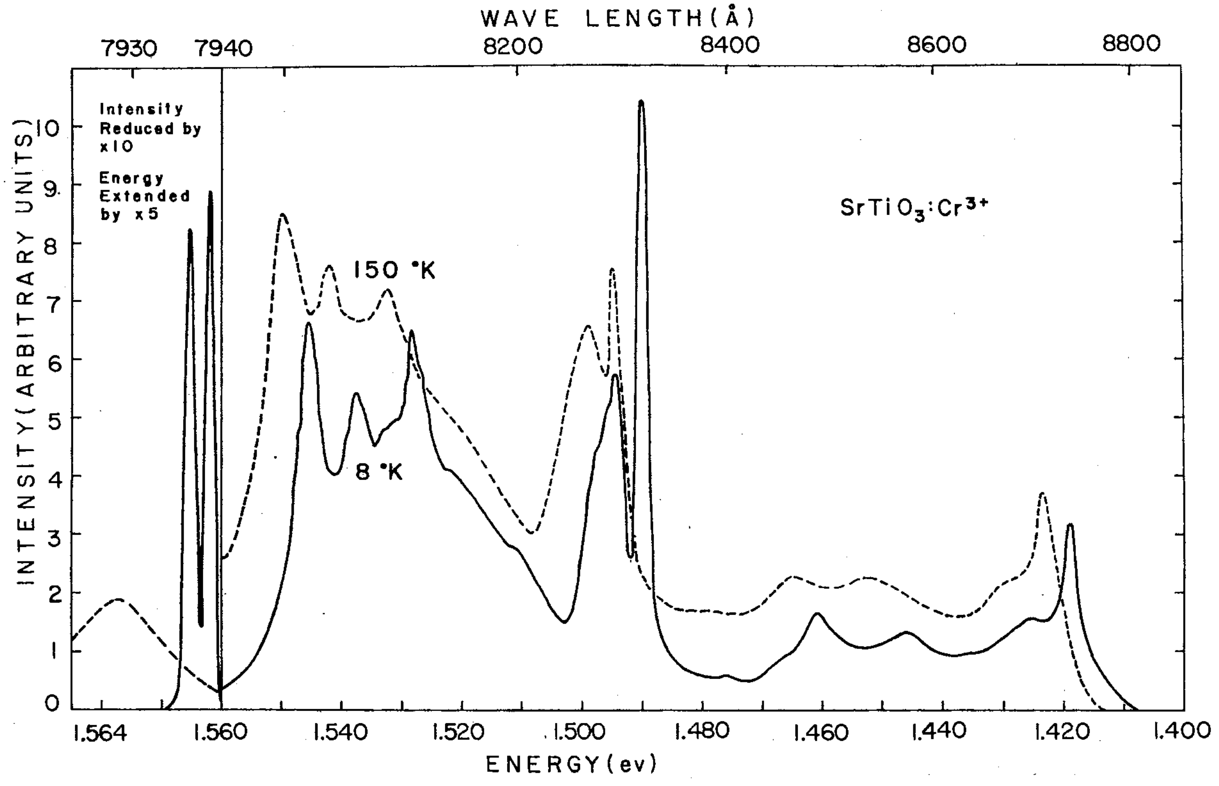

Figure 11. The Fluorescence Spectrum of $SrTiO_3:Cr^{3+}$ at About 8°K and 150°K

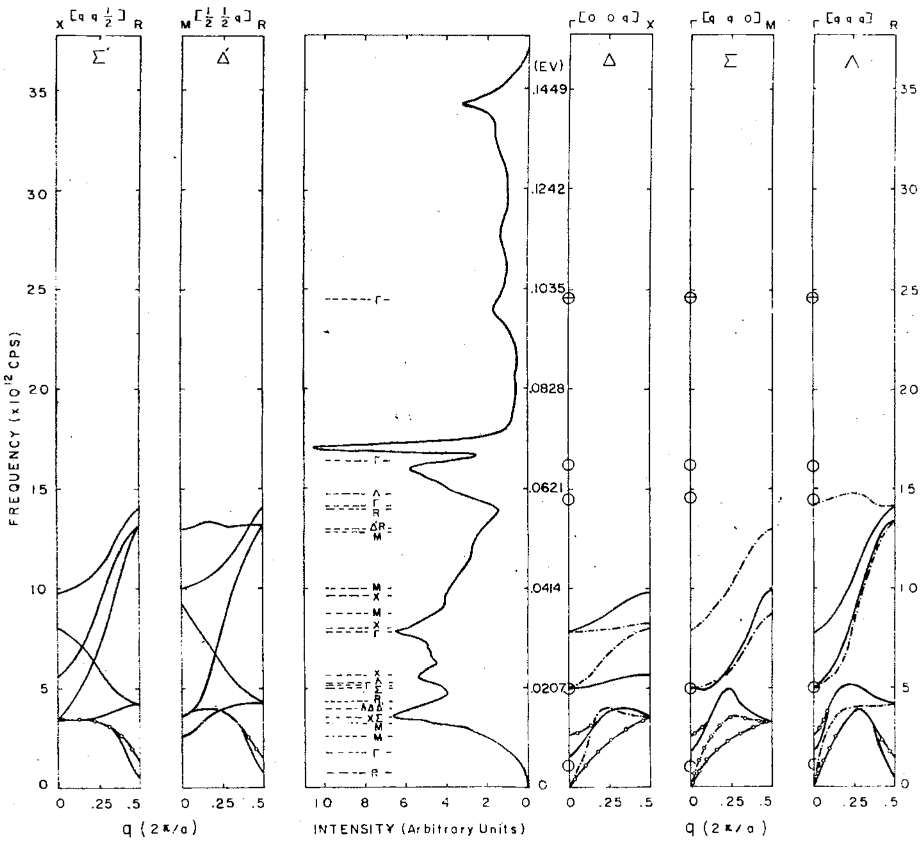

Figure 12. Low Energy Vibronic Spectra at 8°K in Comparison With Neutron Scattering Dispersion Curves of $SrTiO_3$ and Raman and Infrared Data (○). ⊕ is showing the highest observation of the phonon modes by neutron scattering. Solid lines and dashed lines in the right side of the spectra are transverse and longitudinal modes respectively, and the solid lines in the left side of the spectrum are the mixed modes.

TABLE VIII

VIBRATIONAL MODES OF $SrTiO_3$ APPEARING IN SPECTRA OF VIBRONIC, INFRARED ABSORPTION AND RAMAN SPECTRA, AND NEUTRON SCATTERING (UNIT eV X 10^{-2})

Vibronics (^{o}K) (Ref.)			Pure (^{o}K) (Ref.)			Assignment
Cr^{3+}	Mn^{4+}	Eu^{3+}	Infrared	Raman*	Neutron	Mode (Point)
1.30(4)(31) 1.368(8.4) 1.346(20.4)(30)	1.327(20.4)(30)				1.428(297)(6)	TO_1(X)
1.50(4)(31) 1.315(20.4)(30)					1.470(297)(6)	TA(X)
1.483(8.4) 1.485(20.4)(30)	1.486(20.4)(30)				1.491(297)(6)	LA(M)
1.637(8.4) 1.533(20.4)(30)	1.564(20.4)(30)					
1.65(4)(31)	1.639(20.4)(30)				1.651(296)(6)	TO_1(Δ)
1.50(4)(31) 1.869(8.4) 1.688(20.4)(30)					1.805(297)(6)	TO_1(R) LO_1(R)
	1.787(20.4)(30)				1.862(296)(6)	LA(X)
2.11(4)(31) 2.310(8.4) 2.197(20.4)(30)	2.234(20.4)(30)	2.110(77)(29)	2.115(300)(37) 2.210(300)(9) 2.296(300)(12)		2.073(296)(6) 2.110(297)(6)	LO_1(Γ)

TABLE VIII (Continued)

Vibronics (°K) (Ref.)			Pure (°K) (Ref.)			Assignment
Cr^{3+}	Mn^{4+}	Eu^{3+}	Infrared	Raman*	Neutron	Mode (Point)
2.48(4)(31) 2.405(8.4) 2.321(20.4)(30)	2.334(20.4)(30)					
2.20(4)(31)			2.185(300)(37)			$TO_2(\Gamma)$
2.558(8.4)					2.321(296)(6)	
2.38(4)31					2.434(297)(6)	$TO_2(X)$
2.730(8.4)						
2.881(8.4) 2.867(20.4)(30)	2.855(20.4)(30)				2.855(296)(6)	$2TA(X),2TO_1(X)$
3.10(4)(31) 3.071(8.4) 3.078(20.4)(30)	3.041(20.4)(30)			3.103(300)(16)		$TO_3(\Gamma)$
3.222(8.4) 3.252(20.4)(30)	3.265(20.4)(30)					
3.10(4)(31)				3.116(300)(17)	3.289(297)(6)	$LO_2(\Gamma),TO_3(\Gamma)$
3.30(4)(31) 3.393(8.4) 3.426(20.4)(30)	3.426(20.4)(30)				3.395(297)(6)	$LO_1(X)$
					3.478(297)(6)	$LO_1(M)$
3.50(4)(31)					3.602(297)(6)	$LO_2(X)$

TABLE VIII (Continued)

Vibronics (°K) (Ref.)			Pure (°K) (Ref.)			Assignment Mode (Point)
Cr^{3+}	Mn^{4+}	Eu^{3+}	Infrared	Raman*	Neutron	
				3.823(300)(17) 3.848(300)(16)		
3.95(4)(31) 3.899(8.4) 3.923(20.4)(30)					4.079(297)(6)	$TO_3(X)$
					4.120(297)(6)	$TO_5(M)$
					5.549(297)(6)	$TO_3(R)$
				4.580(300)(17) 4.469(300)(16) 4.717(300)(16)	5.590(297)(6)	$TO_2(R), LO_2(R)$
5.70(4)(31)	4.791(20.4)(30)	5.710(77)(29)	5.871(300)(37)		5.673(297)(6)	$LO_3(\Gamma)$
				5.524(4)(16)		
					5.809(297)(6)	$LO_2(M)$
6.40(4)(31) 6.260(8.4) 6.219(20.4)(30)					5.880(297)(6)	$LO_3(R)$
6.459(8.4) 6.430(20.4)(30)	6.356(20.4)(30)					$LO_2(X)$

TABLE VIII (Continued)

Vibronics (^{o}K) (Ref.)			Pure (^{o}K) (Ref.)			Assignment Mode (Point)
Cr^{3+}	Mn^{4+}	Eu^{3+}	Infrared	Raman*	Neutron	
6.78(4)(31) 6.622(8.4) 6.616(204)(30)		6.827(77)(29)	6.778(300)(9) 6.889(300)(12)		6.790(297)(6)	TO$_4$(Γ)
				7.696(300)(16) 7.808(300)(17)		
7.054(8.4) 7.044(20.4)(30) 7.20(4)(31)						Local Mode TO$_4$(X)
			6.827(300)(10)			
8.391(20.4)(30)	8.342(20.4)(30)			8.379(300)(16) 8.491(300)(17)	8.143(296)(6)	2TO$_3$(X)
9.319(8.4) 9.260(20.4)(30)				8.937(300)(16) 9.024(300)(17)		
11.60(4)(31)				9.186(300)(16)		LO$_4$(X)
10.0(4)(31) 9.926(8.4) 9.881(20.4)(30)	10.377(20.4)(30)	9.806(77)(29)	9.980(300)(37)		10.227(297)(6)	LO$_4$(Γ)
10.664(8.4)						
11.430(8.4) 11.445(20.4)(30)	10.799(20.4)(30)					

TABLE VIII (Continued)

Vibronics (°K) (Ref.)			Pure (°K) (Ref.)			Assignment Mode (Point)
Cr^{3+}	Mn^{4+}	Eu^{3+}	Infrared	Raman*	Neutron	
13.252(8.4) 13.195(20.4)(30)	12.438(20.4)(30)			12.786(300)(16) 12.885(300)(17)		
14.203(8.4) 15.417(20.4)(30)	14.114(20.4)(30)			16.447(300)(17)		2(Local Mode)
				20.085(300)(17)		

*Second-order.

modes indicated by circles on the Γ-point axis. The T_{2u} mode is inactive in infrared absorption as are all of the longitudinal optic modes and all acoustic modes. All phonon modes are inactive in first order Raman scattering in the cubic phase and most of the data listed in Table VIII can be attributed to second order scattering processes. Some first order low energy peaks have been observed at low temperatures as discussed in the next section.

Peaks in the vibronic spectra should occur at frequencies of phonon modes having a high density of states and being allowed in vibronic transitions. The density of phonon states is proportional to $1/|\nabla_{\underline{q}}\omega|$ which is just the reciprocal of the slope of the phonon dispersion curves. Thus, when the dispersion curves have zero slope there will be a high density of states region. This may occur at the high symmetry points on the zone boundary and along some of the lines of high symmetry as shown in Figure 12. It might also occur at other points of lower symmetry where dispersion curves have not been obtained. The dashed lines near the vibronic spectra in Figure 12 indicate the high density of states regions for the dispersion curves of the phonon modes shown. Their positions at special points in the Brillouin zone are listed in Table IX. The selection rules given in Table VI indicate that certain phonons will not contribute to the observed vibronic spectrum and these are identified (marked *) in Table IX. A reasonable correlation can be seen between the other vibronic peaks and high density of states regions between about 0.0100 and 0.0621 eV. The lower energy region is discussed in the next section. The vibronic peaks at 0.0661 eV and 0.0994 eV correspond to the Γ-point modes observed in infrared absorption. The other vibronic structure at high energies can be attributed to two-phonon processes as

TABLE IX

VIBRATIONAL NORMAL MODES AT 297°K FOR THE PRINCIPAL SYMMETRY POINTS DETERMINED FROM NEUTRON SCATTERING AND BY A RIGID SHELL MODEL

Points			Modes (x 10^{-2} eV)						
Γ (0,0,0)	Transverse	Irreducible Representation	T_{1u}	T_{1u}	T_{1u}	T_{2u}		T_{1u}	
		Experiment	0	1.14±0.04	2.10±0.04	3.29±0.06		6.78±0.04	
		Theory	0	1.06	2.14	3.42		6.93	
	Longitudinal	Irreducible Representation	T_{1u}		T_{1u}	T_{2u}	T_{1u}		T_{1u}
		Experiment	0		2.10±0.04	3.29±0.06	5.67±0.21		10.21±0.12
		Theory	0		2.11	3.42	6.10		9.06
X (0,0,½)	Transverse	Irreducible Representation	E_g^*	E_u	E_g^*			Eu	
		Experiment	1.47±0.02	1.47±0.02	2.43±0.03			4.09±0.08	
		Theory	1.48	1.51	2.49			3.85	
	Longitudinal	Irreducible Representation	A_{2u}			A_{1g}^*	B_{1g}^*		
		Experiment	1.43±0.06			3.39±0.08	3.60±0.06		
		Theory	1.68			3.72	3.81		
M (½,½,0)	Transverse	Irreducible Representation	B_{1g}^*	B_{1u}^*	A_{2u}			E_g^*	
		Experiment	1.09±0.02	1.38±0.05	1.38±0.05			4.11±0.08	
		Theory	0.83	1.34	1.50			3.78	
	Longitudinal	Irreducible Representation				E_u	E_u		A_{1g}^*
		Experiment				1.49±0.06	3.47±0.08		5.81±0.10
		Theory				1.35	3.70		

TABLE IX (Continued)

Points		Modes (x 10^{-2} eV)					
R (½,½,½)	Transverse	Irreducible Representation	T_{2u}	T_{1u}	E_u*	T_{1u}	
		Experiment	0.64±0.02	1.80±0.05	5.58±0.08	5.54±0.17	
		Theory	0.73	1.54	5.14	5.23	
	Longitudinal	Irreducible Representation	T_{2u}	T_{1u}	T_{1u}		T_{2g}*
		Experiment	0.64±0.02	1.80±0.05	5.58±0.08		5.87±0.21
		Theory	0.73	1.54	5.23		5.99

*Forbidden by vibronic selection rules.

discussed below.

The computer program described in Chapter II can be used to separate the one-phonon and multi-phonon contributions to the observed low energy vibronic sideband. For $G_B^{exp}(ab;\omega_q)$ the observed intensity of the vibronic spectrum divided by ω^3 at every 0.000497 eV was used (see Equation (47)). Since the structure in the vibronic spectrum closely resembles that predicted from phonon dispersion curves up to 0.1243 eV as discussed above, the first estimate for $G_1(ab;\omega_q)$ was taken as the observed shape divided by ω^3 of the sideband up to and including the local mode at 0.0706 eV. The initial value we tried for the Huang-Rhys factor was 0.766 which was the value obtained from finding the ratio of the area of the zero-phonon lines to that of the estimated one-phonon sideband at 8^oK (see Equation (87)). The results of this are shown in Figure 13. Part (b) of the figure shows the one-phonon, two-phonon, and three-phonon contribution to the vibronic spectra predicted by the computer after going through the iteration process described in Chapter II. This results in the good fit to the data shown in part (a) of the figure. In this case three-phonon and higher order processes are predicted to make negligible contributions to the spectra. The two-phonon processes are predicted to make almost no contribution to the structure observed in the sideband but they do make a significant contribution to the spectral intensity between about 0.0500 and 0.1500 eV. The one-phonon contribution predicted by the computer is similar to the initial estimate used as input for $G_1(ab;\omega_q)$ below 0.0800 eV but in addition it includes much of the sideband and structure greater than 0.0900 eV. This is not expected in comparison with neutron scattering results as seen in Figure 12.

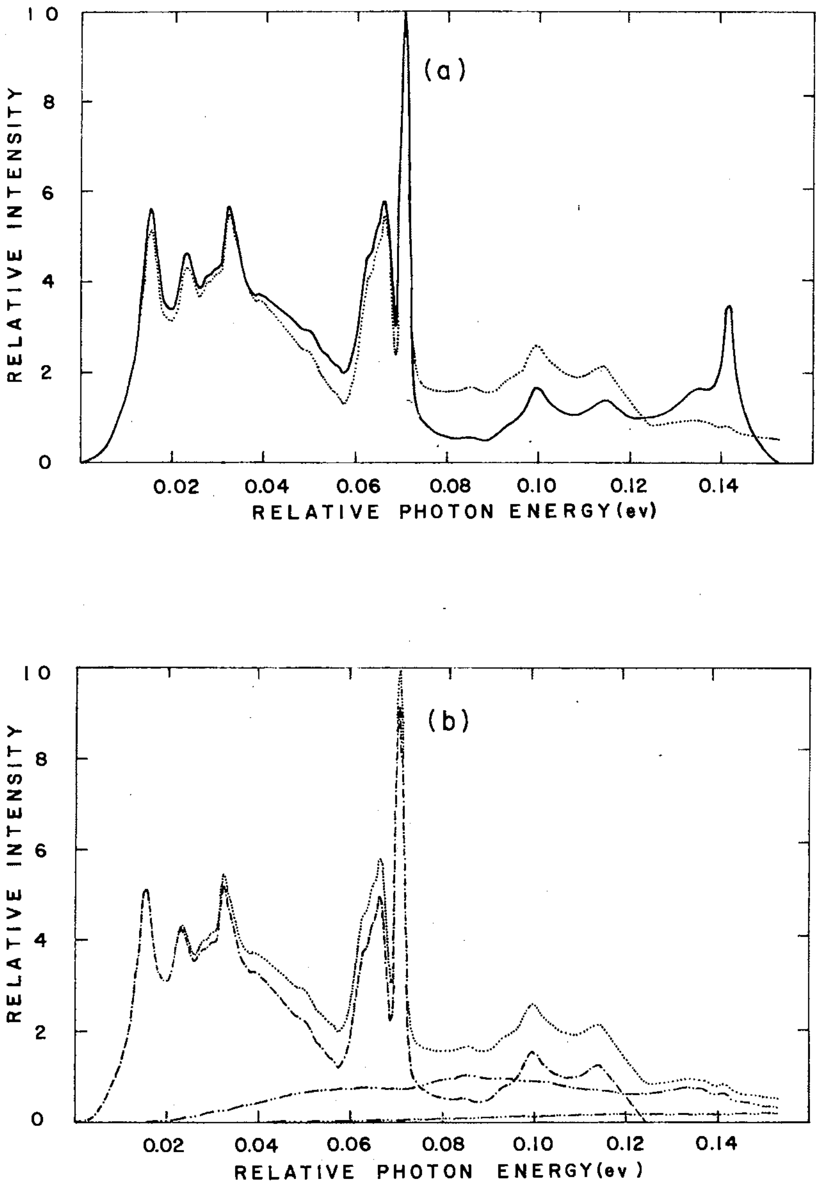

Figure 13. (a) Measured (———) and Calculated (····) Broad Band Spectrum Using Huang-Rhys Factor S = 0.766 and an Estimated One-Phonon Spectrum. (b) One (-·-·-), two (-··-··-) and three (-···-···-) phonon contribution to the vibronic broad band (··········) with S = 0.766.

In an attempt to account for this apparent discrepancy in the predicted one-phonon vibronic sideband we explicitly included the interaction between the local mode and the lattice modes by including the quadratic term in Equation (75). To do this we assume that the coupling strength represented by the parameter α is the same for all lattice modes with energies less than the local mode. In the simplest approximation the quadratic coupling coefficients can be written as

$$V^2_{qq_{1m}} \approx (\alpha V_q V_{q_{1m}})^2 = \alpha^2 V_q^2 V_{q_{1m}}^2 = \alpha^2 S_q S_{q_{1m}} \omega_q^2 \omega_{q_{1m}}^2 \hbar^4 . \tag{90}$$

Thus,

$$g_2(t) = \frac{\alpha^2\hbar^2}{2} \Sigma \frac{S_q S_{q_{1m}} \omega_q^2 \omega_{q_{1m}}^2}{(\omega_q + \omega_{q_{1m}})^2} \left(e^{-(\omega_q+\omega_{q_{1m}})t} - 1\right) . \tag{91}$$

Then the n-phonon spectrum predicted in Equation (83) becomes

$$G_n(ab;\omega) = e^{-S} \int_{-\infty}^{\infty} dt\, e^{i(\omega-\omega_0)t} \frac{\{g_1(t) + g_2(t)\}^n}{n!} , \tag{92}$$

and the one-phonon spectrum with this quadratic coupling will be approximately

$$G_1'(ab;\omega) = 2\pi e^{-S} \Big[\Sigma_{q'} S_{q'} \delta\{(\omega_0-\omega) - \omega_{q'}\} + \frac{\alpha^2\hbar^2}{2} \Sigma_q \frac{S_q S_{q_{1m}} \omega_q^2 \omega_{q_{1m}}^2}{(\omega_q + \omega_{q_{1m}})^2} \{\delta([\omega_0-\omega] - [\omega_q + \omega_{q_{1m}}]) + \delta(\omega_0-\omega)\}\Big] . \tag{93}$$

Now the spectrum can be considered in three distinct regions. For

$$\omega_q \leq 0.0706 \; (\omega_{q_{1m}}) \text{ eV} ,$$

or

$$\omega_q \geq 0.1476 \; (\omega_{q_{1m}} + \omega_{q_{max}}) \text{ eV} ,$$

the predicted one-phonon spectrum is the same as with no quadratic coupling,

$$G_1'(\omega_q) = 2\pi \, e^{-S} \, S_q = G_1(\omega_q) \; . \tag{94}$$

For

$$0.0706 \text{ eV} < \omega_q < 0.1476 \text{ eV}$$

$$G_1'(\omega_q) = 2\pi \, e^{-S} \, \{S_q + \frac{\alpha^2 \hbar^2}{2} \frac{S_{q-q_{1m}} \, S_{q_{1m}} \, \omega^2_{q-q_{1m}} \, \omega^2_{q_{1m}}}{(\omega_{q-q_{1m}} + \omega_{q_{1m}})^2}\} \; . \tag{95}$$

An estimate for the quadratic coupling parameter α can be obtained from comparing the intensity of the local mode peak with that of its first harmonic

$$G_1'(2\omega_{q_{1m}}) = \frac{\pi\hbar^2}{4} \, e^{-S} \, \alpha^2 \, S^2_{q_{1m}} \, \omega^2_{q_{1m}} \; . \tag{96}$$

This gives $\alpha = 255$ 1/eV.

The results of this fitting procedure are shown in Figure 14. Part (a) of the figure shows the best fit between the observed and predicted results which was obtained with $\alpha = 350$ 1/eV. The fit is excellent for energies less than 0.0800 eV. Above this energy all of the observed structure is predicted but the intensities are not always exactly cor-

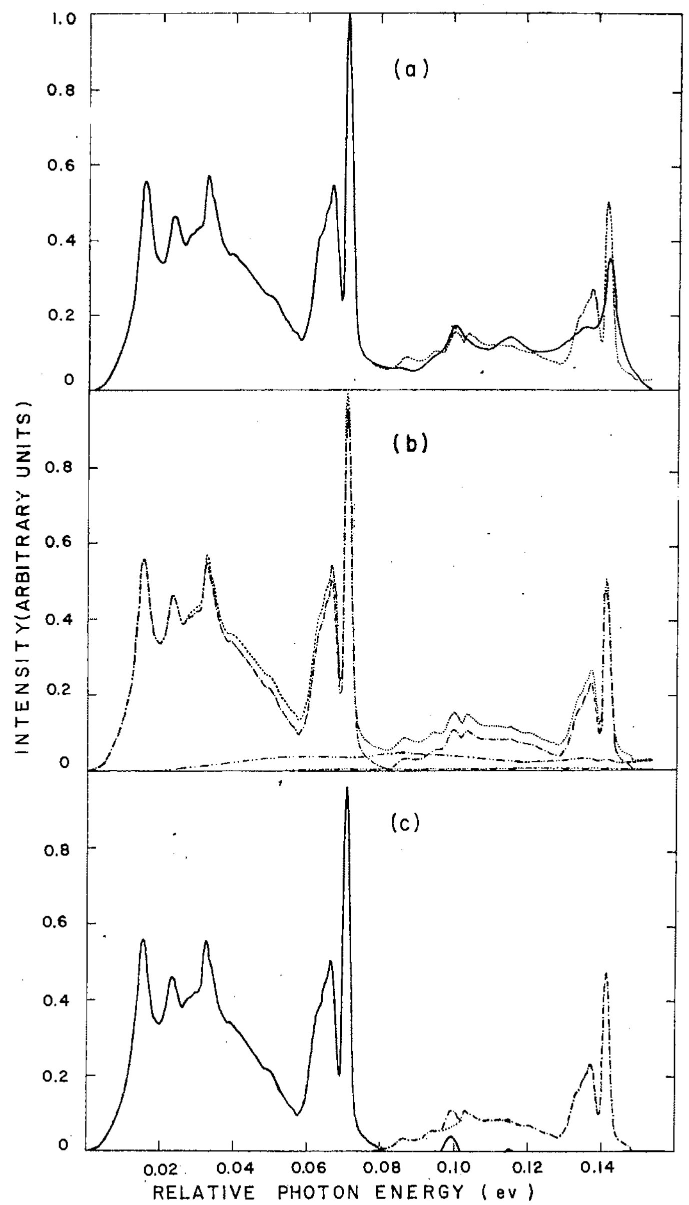

Figure 14. (a) The Best Fit Between Observed (———) and Predicted (····) Vibronic Sideband Which was Obtained with α = 350 1/eV and S = 0.300. (b) One (-·-·-), two (-··-··-) and three (-···-···-) phonon contributions to the predicted vibronic broadband (······). (c) Predicted one-phonon side band (———) and the contribution (·····) due to quadratic coupling with the local mode to the effective one-phonon sideband (-·—·-·-).

rect. Part (b) of the figure shows that most of the structure in the spectrum is due to the one-phonon contributions with quadratic coupling while two-phonon processes contribute significantly to the intensity of the spectrum only between about 0.0500 and 0.1100 eV and higher order processes are negligible. Figure 14(c) shows the predicted one-phonon sideband and the contribution due to quadratic coupling with the local mode. The one-phonon spectrum extends up to 0.0800 eV with two small peaks occurring at higher energies. The quadratic coupling accounts for most of the spectrum above 0.0800 eV. This shows the importance of quadratic coupling in the vibronic spectrum of this system. The discrepancies between the observed and predicted sideband can probably be attributed to the fact that the coupling constant can be different for different phonon modes.

The structure in the one-phonon sideband shown in Figure 14(c) compares well with what would be predicted from other data as shown in Figure 12. All of the observed structure in the vibronic sideband at lower energies than the local mode is part of the one-phonon contribution. The only significant structure predicted at higher energies occurs at 0.1000 eV which is also a peak in the one-phonon sideband. The very small peak at 0.1148 eV is insignificant.

The one-phonon sideband can be considered an effective phonon density of states for the host crystal. This can be written explicitly as

$$\rho(\omega) = G_1(ab;\omega) = \sum_q S_q \, \delta(\omega_o-\omega-\omega_q) = \sum_q \frac{V_q^2}{\hbar\omega_q^2} \, \delta(\omega_o-\omega-\omega_q). \qquad (97)$$

Using this and Equations (47), (78) and (84) the vibronic transition probability at low temperatures becomes

$$
\begin{aligned}
P_{ab} &\approx P_{ab}^{(1)} \\
&= C\omega^3 |M_{ab}|^2 \, G_1(ab;\omega) \\
&= 2\pi C\omega^3 |M_{ab}|^2 e^{-S} \sum_q S_q \, \delta(\omega_o - \omega - \omega_q) \\
&= \frac{2\pi}{\hbar^2} C\omega^3 |M_{ab}|^2 \, e^{-S} \, \frac{\rho(\omega_q)}{\omega_q^2} \, ,
\end{aligned} \tag{98}
$$

where

$$
S = \frac{1}{\hbar^2} \int_0^\infty d\omega_q \, \frac{\rho(\omega_q)}{\omega_q^2} \, . \tag{99}
$$

This shows how the effective density of states is obtained from the experimentally observed one-phonon vibronic sideband. This $\rho(\omega_q)$ can then be used to obtain theoretical predictions for the temperature dependences of the widths and positions of the zero-phonon line as described in the next chapter.

In order to obtain the real density of phonon states for the crystal from the effective density of states observed in vibronic spectra it is necessary to explicitly express the phonon frequency and wave vector dependences of the electron-phonon coupling parameter for each phonon mode. This is quite complicated to do and has been done in only a very few cases on crystals with simple structures (1). Approximations for these expressions in the limit of long wavelength phonons have given reasonable results in some cases (2). Such approximations have been shown to be especially good in the spectral region very close to the zero-phonon line (37,38). We outline here the long wavelength phonon model and analyze our results for $SrTiO_3:Cr^{3+}$ in terms of this model.

In order to keep the calculations as simple as possible we neglect difference in masses of the impurity ion and the ion it replaces in the lattice. Also the phonon modes of the crystal with impurities are assumed to be the same as the phonon modes of the perfect crystal. Finally, only nearest neighbor vibrations are assumed to make important contributions to the electron-phonon interaction at the impurity ion.

The electron-phonon interaction Hamiltonian developed in Chapter II must be rewritten using an exact expression for the crystal field in the expansion given in Equation (4) and using the exact expression for the strain tensor instead of its average value given in Equation (7). The position of the nuclei of the ions in the lattice is designated by the vector $\underline{R}$ with the impurity nucleus located at the origin of the coordinate system, $\underline{R} = 0$. The coordinate of the transition electron on the impurity ion is $\underline{r}$. The effective charge and the displacement from equilibrium of the atom at position $\underline{R}$ are given by $z(\underline{R})$ and $u(\underline{R})$, respectively. The crystal field at the transition electron can then be written as

$$V(\underline{r}) = \sum_{\underline{R}\neq\underline{o}} \frac{ez(\underline{R})}{|\underline{R} + \{\underline{u}(\underline{R}) - \underline{u}(\underline{O})\} - \underline{r}|} . \tag{100}$$

In the usual case of localized impurity electron states and small applitude lattice vibrations,

$$|\underline{u}(\underline{R}) - \underline{u}(\underline{o})| << |\underline{R}| \text{ and } |\underline{r}| << |\underline{R}| , \tag{101}$$

the crystal field can be expanded in terms of the relative displacements $\underline{u}(\underline{R}) - \underline{u}(\underline{o})$,

$$V(\underline{r}) = \sum_{\underline{R}\neq \underline{o}} \frac{ez(\underline{R})}{|\underline{R}-\underline{r}|} - \sum_{\underline{R}\neq \underline{o}} \sum_{\mu} \frac{ez(\underline{R})}{|\underline{R}-\underline{r}|^3} (R_\mu - r_\mu)\{u_\mu(\underline{R}) - u_\mu(\underline{o})\} - \dots \qquad (102)$$

As was done in Equation (4) the first term in this expansion is considered part of the Hamiltonian for the static crystal and the second term is used as the electron-phonon interaction Hamiltonian. Because of the second condition in Equation (101) this term can be expanded in a Taylor series in $\underline{r}$, then the electron-phonon interaction Hamiltonian becomes

$$H^{i-v}_{int} = - \sum_{\underline{R}\neq \underline{0}} \sum_{\mu} \frac{ez(\underline{R})}{|\underline{R}-\underline{r}|^3} (R_\mu - r_\mu)\{u_\mu(\underline{R}) - u_\mu(\underline{o})\}$$

$$= - \sum_{\underline{R}\neq \underline{0}} \sum_{\mu} \frac{ez(\underline{R})}{|\underline{R}|^3} R_\mu\{u_\mu(\underline{R}) - u_\mu(\underline{o})\}$$

$$- \sum_{\underline{R}\neq \underline{0}} \sum_{\mu} \frac{ez(\underline{R})}{|\underline{R}|^5} (3R_\mu \, \underline{R}\cdot\underline{r} - r_\mu|\underline{R}|^3) \{u_\mu(\underline{R}) - u_\mu(\underline{o})\} \, . \qquad (103)$$

Note that the first term is independent of the electron coordinate $\underline{r}$ and therefore has non-zero matrix elements between the same electronic states. This is not true for the second term. Thus when only the first term is used to determine the matrix elements for vibronic transitions given in Equation (9) the only term left in the sum over intermediate electronic states is $\Psi^{el}_j = \Psi^{el}_i$. Thus the multipole character of the electronic part of the vibronic transition will be the same as that of the zero-phonon line. If the second term in Equation (103) is used as the interaction Hamiltonian in Equation (9) the intermediate states will be different than the initial state and the electronic part of the vibronic transition may be electric dipole for either electric dipole or magnetic dipole zero-phonon lines. This is especially important for crystal structures with a center of symmetry where electric dipole transitions are forbidden for the zero-phonon line.

Next we want to express the displacements in terms of the local strain tensor. To do this we expand the ionic displacements

$$u_\mu(\underline{R} + \Delta\underline{R}) - u_\mu(\underline{R}) = \sum_\nu \frac{\partial u_\mu(\underline{R})}{\partial R_\nu} \Delta R_\nu + \tfrac{1}{2} \sum_\nu \sum_\xi \frac{\partial u_\mu(\underline{R})}{\partial R_\nu \partial R_\xi} \Delta R_\nu \Delta R_\xi , \quad (104)$$

which is valid for long wavelength phonons. For our case this expansion becomes

$$u_\mu(\underline{o} + \underline{R}) - u_\mu(\underline{0}) = \sum_\nu \frac{\partial u_\mu(\underline{o})}{\partial R_\nu} R_\nu + \tfrac{1}{2} \sum_\nu \sum_\xi \frac{\partial u_\mu(\underline{o})}{\partial R_\nu \partial R_\xi} R_\nu R_\xi . \quad (105)$$

The strain tensor at $\underline{r} = \underline{0}$ can be written as

$$\varepsilon_{\mu\nu}(\underline{0}) = \tfrac{1}{2} \left\{ \frac{\partial u_\mu(\underline{0})}{\partial R_\nu} + \frac{\partial u_\nu(\underline{0})}{\partial R_\mu} \right\} . \quad (106)$$

At this point we must consider specific lattice structures. Since strontium titanate is a very complicated structure we will assume a simpler structure to try to obtain approximate results. Rocksalt and zinc blende are the only two structures which have been treated in detail (39). The former is centrosymmetric while the latter does not have a center of symmetry. Since strontium titanate does not have a center of symmetry at low temperatures it should be more closely analogous to zinc blende and we will outline Vredevoe's treatment of this structure. Figure 15 shows the nearest neighbor configuration of zinc blende.

Both terms in Equation (103) must be evaluated for this structure. Using Equation (109) and the values of the nearest neighbor coordinates

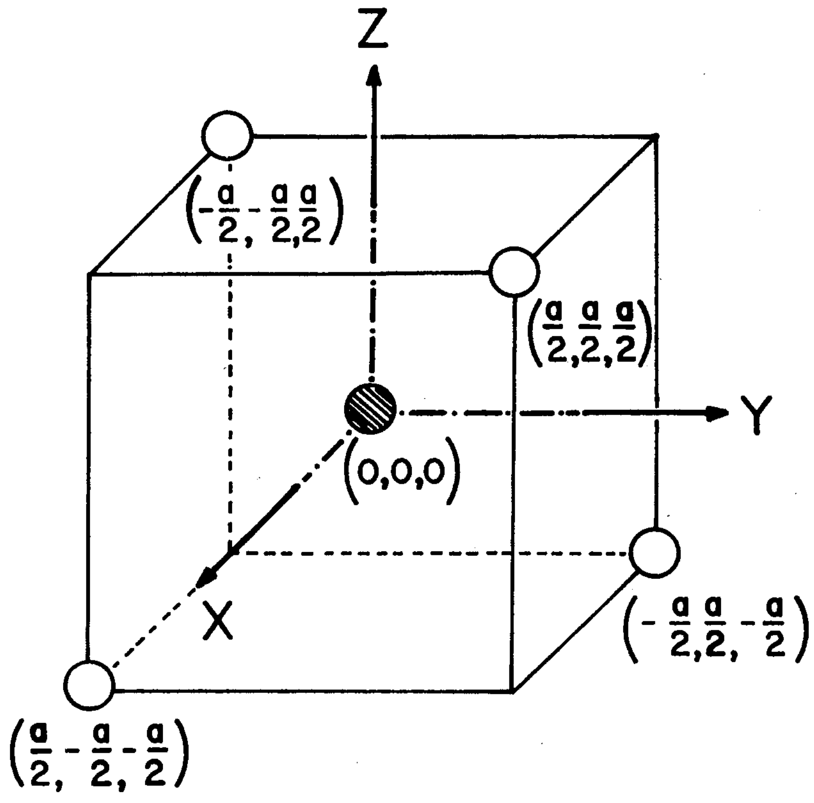
Z
$\left(-\frac{a}{2}, -\frac{a}{2}, \frac{a}{2}\right)$
$\left(\frac{a}{2}, \frac{a}{2}, \frac{a}{2}\right)$
Y
(0,0,0)
X
$\left(-\frac{a}{2}, \frac{a}{2}, -\frac{a}{2}\right)$
$\left(\frac{a}{2}, -\frac{a}{2}, -\frac{a}{2}\right)$

Figure 15. First Nearest Neighbor Atoms of Bromine in Zinc Blende. ◍:Bromine, ○:Zinc

shown in Figure 15 the summation over $\underline{R}$ can be evaluated. The first term is

$$- \sum_{\underline{R}\neq\underline{0}}^{4} \sum_{\mu} \frac{ze}{|\underline{R}|^3} R_\mu \{u_\mu(\underline{R}) - u_\mu(\underline{0})\} = - \frac{8\ ez}{3\sqrt{3}\ a^3} \sum_{\underline{R}\neq\underline{0}}^{4} (\sum_{\mu\nu} \frac{\partial u_\mu(\underline{0})}{\partial R_\nu} R_\mu R_\nu$$

$$+ \frac{1}{2} \sum\sum\sum_{\mu\nu\xi} \frac{\partial^2 u_\mu(\underline{0})}{\partial R_\nu\ \partial R_\xi} R_\mu\ R_\nu\ R_\xi)$$

$$= - \frac{8ez}{3\sqrt{3}\ a} \sum_{\mu} \varepsilon_{\mu\mu}(\underline{0}) - \frac{2ez}{3\sqrt{3}} \sum_{\mu\nu\xi}{}' \frac{\partial \varepsilon_{\mu\nu}(\underline{0})}{\partial R_\xi} . \tag{107}$$

The second term becomes

$$- \sum_{\underline{R}\neq\underline{0}}^{4} \sum_{\mu} \frac{ez}{|\underline{R}|^5} (3\ R_\mu\ \underline{R}\cdot\underline{r} - r_\mu |\underline{R}|^2) \{u_\mu(\underline{R}) - u_\mu(\underline{0})\}$$

$$= - \frac{32\ ez}{3\sqrt{3}\ a^5} \sum_{\underline{R}\neq\underline{0}}^{4} (3 \sum_{\mu} \sum_{\xi} R_\mu R_\xi r_\xi - \frac{3a^2}{4} \sum_{\mu} r_\mu)(\sum_{\nu} \frac{\partial u_\mu(\underline{0})}{\partial R_\nu} R_\nu + \tfrac{1}{2} \sum\sum_{\nu\xi} \frac{\partial^2 u_\mu(\underline{0})}{\partial R_\nu\ \partial R_\xi} R_\nu R_\xi)$$

$$= - \frac{16\ ez}{3\sqrt{3}\ a^2} \sum_{\mu\nu\xi}{}' r_\nu \varepsilon_{\mu\xi}(\underline{0}), \tag{108}$$

where Σ' implies that all summation subscripts are different.

Combining Equations (107) and (108) gives

$$H_{int}^{i-v} = - \frac{8ez}{3\sqrt{3}\ a} \sum_{\mu} \varepsilon_{\mu\mu}(\underline{0}) - \frac{2ez}{3\sqrt{3}} \sum_{\mu\nu\xi}{}' \frac{\partial \varepsilon_{\mu\nu}(\underline{0})}{\partial R_\xi} - \frac{16\ ez}{3\sqrt{3}\ a^2} \sum_{\mu\nu\xi}{}' r_\nu \varepsilon_{\mu\xi}(\underline{0}) . \tag{109}$$

The displacements can be written in terms of the phonon creation and annihilation operators using Equation (5),

$$u_\mu(\underline{q},\underline{R}) = \frac{1}{\sqrt{Nm}} (\frac{\hbar}{2\omega_q})^{\frac{1}{2}} (b_q^{\ \mu} + b_q^{\ \mu+})\ \hat{\Pi}_q^{\ \mu}\ e^{i\underline{q}\cdot\underline{R}} , \tag{110}$$

where N is the number of unit cells, each of which has mass m, and $\hat{\Pi}_q^{\mu}$ is the polarization vector. Thus,

$$H_{int}^{i-v} = -\frac{16\ ez}{3\sqrt{3}\ a^2} \left(\frac{\hbar}{2\omega_q Nm}\right)^{\frac{1}{2}} \sum_{\mu} (b_q^{\mu} + b_q^{\mu+})\, \hat{\Pi}_q^{\mu} \left[\frac{a}{2} q_{\mu} + \frac{a^2}{8} \sum_{\substack{\nu\neq\mu \\ \xi\neq\mu}}' q_{\nu} q_{\mu} + \sum_{\substack{\nu\neq\mu \\ \xi\neq\mu}}' r_{\nu} q_{\xi}\right] . \qquad (111)$$

To simplify this expression let us assume that the non-diagonal term is much more important than the two diagonal terms. The validity of this assumption will be discussed later. Also let us restrict ourselves to the limit of long wavelengths where the surfaces of constant energy are approximately spherical and $q = \omega_q/v$. Then Equation (111) becomes

$$H_{int}^{i-v} = -\frac{16\ ez}{3\sqrt{3}\ a^2} \left(\frac{\hbar\ \omega_q}{2Nmv^2}\right)^{\frac{1}{2}} \sum_{\mu} (b_q^{\mu} + b_q^{\mu+})\, \hat{\Pi}_q^{\mu} \sum_{\nu\neq\mu} r_{\nu} . \qquad (112)$$

This can be expressed as

$$H_{int}^{i-v} = D\omega_q^{\frac{1}{2}} \sum_{\nu\neq\mu} r_{\nu} \sum_{\mu} \hat{\Pi}_q^{\mu} (b_q^{\mu} + b_q^{\mu+})$$

$$= V_q \sum_{\mu} \hat{\Pi}_q^{\mu} (b_q^{\mu} + b_q^{\mu+}) \sum_{\nu\neq\mu} r_{\nu} ,$$

where

$$V_q = \omega_q^{\frac{1}{2}} D \qquad (113)$$

where D is a constant. Using this the effective phonon density of states can be written as

$$\rho(\omega) = \Sigma_q \frac{D^2}{\hbar^2\omega_q}\,\delta(\omega_o-\omega-\omega_q) = \frac{g(\omega_o-\omega)}{\omega_o-\omega} = g(\omega_q)/\omega_g), \qquad (114)$$

where $g(\omega_q)$ is the real density of phonon states of the with impurities with the approximations made above.

The phonon frequency distribution for strontium titanate can be obtained from our experimental data using Equations (98) and (114). The results are shown in Figure 16. They were obtained by multiplying the projected one-phonon vibronic sideband shown in Figure 14(c) by ω_q. The results are compared to the phonon density of states obtained by Stirling (6) from theoretically fitting his neutron scattering data. The peak positions in the two curves are in excellent agreement. The two peaks appearing in the neutron scattering data at 0.0380 eV and 0.0455 eV which are not present in the vibronic data are forbidden by symmetry selection rules as discussed in Chapter II. The theoretically predicted high energy peak at 0.0902 in the neutron scattering data does not agree well with experimental results. As seen in Figure 12 the Γ-point neutron scattering peak is observed at 0.1021 eV which agrees well with the vibronic data. The peak at 0.0154 eV is due to contributions from phonons at several different points in the Brillouin zone. Several of these are forbidden in vibronic spectra (see Table VI) which may account for the relative low intensity in the vibronic density of states. Also these phonons are not near the center of the zone so the approximation of Equation (113) may not be good in this region. The fact that good agreement exists between the densities of states obtained from neutron scattering data and vibronic spectra implies that the presence of impurities does

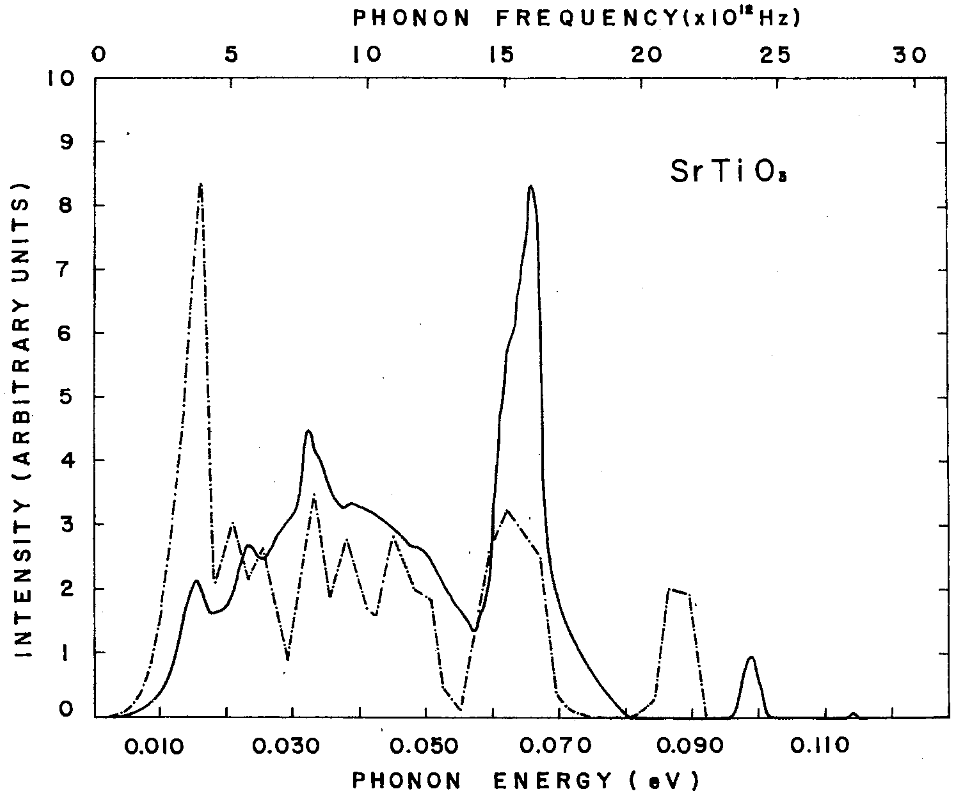

Figure 16. Density of Phonon States of the SrTiO$_3$ Calculated From Fitting a Rigid Shell Model to Neutron Scattering Data (-•-•-) and Obtained From Vibronic Spectra (———)

not greatly effect the perfect lattice phonon frequency distribution and that no significant contributions to the structure in the density of states are made by general points in the Brillouin zone. Notice that, even though better density of phonon states to the Stirling's results can be obtained by multiplying one or ω_q^{-1} to the effective one-phonon density of states, by now we couldn't find out the physical reason.

In order to check the validity of the above assumptions the expression for the transition rate can be obtained. This can be accomplished using Equation (1) and the expression Equation (112) for the ion-phonon interaction Hamiltonian. If we write the components of q explicitly instead of replacing them with ω_q/v this becomes

$$P_{ab} = \left(\frac{16\ ez}{3\sqrt{3}\ a^2}\right)^2 \left(\frac{(n_q+1)\hbar}{2\omega_q\ Nm}\right) \Bigg| \sum_{\mu,\nu,\xi}{}' \hat{\Pi}_q^{\mu} q_{\xi} \Bigg(\sum_j \frac{\langle\Psi_b^{el}|\underline{E}\circ\underline{r}|\Psi_j^{el}\rangle\langle\Psi_j^{el};n_q+1|r_\nu|\Psi_a^{el};n_q\rangle}{E_j^{el} - E_a^{el} + \hbar\omega_q}$$

$$+ \frac{\langle\Psi_b^{el};n_q+1|r_\nu|\Psi_j^{el};n_q\rangle\langle\Psi_j^{el}|\underline{E}\circ\underline{r}|\Psi_a^{el}\rangle}{E_j^{el} - E_a^{el} + \hbar\omega} \Bigg|^2 \left[\frac{e^{i(E_a-E_b)t/\hbar} - 1}{E_a - E_b}\right]^2 \qquad (115)$$

This is similar to Equation (9) except that we have now included the time dependence which was previously neglected and we have not expressed the ion-photon interaction Hamiltonian explicitly since at this point we are only interested in the phonon frequency dependence. For the low temperature region of interest here the phonon population number can be set equal to zero. The sum over the components of $\underline{q}$ and the polarization vectors can be simplified by noting that under a symmetry transformation of the crystal $\underline{\underline{S}}$

$$\hat{\Pi}^{\mu}(\underline{\underline{S}}\ \underline{q}) = \sum_{\nu} S_{\mu\nu}\ \hat{\Pi}^{\mu}(\underline{q}) \ . \qquad (116)$$

The typical terms appearing in Equation (115) can be written as

$$\hat{\Pi}_q^{\xi}\ \hat{\Pi}_q^{\mu *}\ q_\xi\ q_\nu\ .$$

The transformation matricies for the zinc blende structure predict that only terms with $\mu=\xi$ and $\xi=\nu$ are non-zero. Also in the long wavelength limit treated here $[\sum_\mu \hat{\Pi}_q^{\mu}]^2 = 1$ so $[\hat{\Pi}_q^{\mu}]^2$ can be given the approximate value of 1/3. With these approximations the transition rate is

$$P_{ab} = \left(\frac{16\ ez}{3\sqrt{3}\ a^2}\right)^2 \left(\frac{\hbar}{6\omega_q Nm}\right) \sum_{\mu,\nu,\xi}{}' q_\xi^{\ 2} \left|M_{ab}\right|^2 \left[\frac{e^{i(E_a - E_b)t/\hbar} - 1}{E_a - E_b}\right]^2 \ . \tag{117}$$

The square of the exponential can be expressed as a delta function integral over q. Performing this integration gives

$$P_{ab} = \left(\frac{16\ ez}{3\sqrt{3}\ a^2}\right)^2 \left(\frac{\hbar}{6\ Nm}\right) \sum_{\mu\nu\xi}{}' \left|M_{ab}\right|^2 \int \frac{\cos^2\phi q^2}{vq}\, \delta(E_a - E_b - \hbar\omega - \hbar\omega_q)\ d\underline{q}$$

$$= \left(\frac{16\ ez}{3\sqrt{3}\ a^2}\right)^2 \left(\frac{\hbar}{6Nmv}\right) \sum_{\mu\nu\xi}{}' \left|M_{ab}\right|^2 \int_0^{2\pi} \int_0^{\pi} \int_0^{\pi/a} q^3\, \delta[\hbar(\omega_o - \omega) - vq]\, dq \sin\theta d\theta \cos^2\phi\ d\phi$$

$$\approx \left(\frac{16\ ez}{3\sqrt{3}\ a^2}\right)^2 \left(\frac{\hbar}{6Nmv}\right) \sum_{\mu\nu\xi}{}' \left|M_{ab}\right|^2 \frac{(\omega_o - \omega)^3}{\hbar^3 v^3}\, \frac{4}{3}\, \pi$$

$$= \left(\frac{16\ ez}{3\sqrt{3}\ a^2}\right)^2 \left(\frac{4\ \pi}{18\ \hbar^2\ v^4 mN}\right) \omega_q^3 \sum_{\mu\nu\xi}{}' \left|M_{ab}\right|^2 \ . \tag{118}$$

Where ω is the photon frequency, ω_o is the frequency of the zero-phonon line and the relation $\omega_q = vq$ has been used.

This expression predicts that the vibronic spectrum should exhibit an intensity proportional to the cube of the frequency difference from the zero-phonon line in the long wavelength limit. This limit should be a good approximation near the zero-phonon line. Figure 17 shows a plot of the intensity of the vibronic sideband near the R lines of $SrTiO_3:Cr^{3+}$. This is seen to vary as

$$I = A + B\omega_q^{2.9} \tag{119}$$

which is excellent agreement with the above predictions. The additive constant may be due to the R_2 line vibronics or the effects of microscopic strains. A similar factor was found for $Al_2O_3:Cr^{3+}$ (40). The good agreement in this region indicates that the approximations made in deriving Equation (113) are not unreasonable. Specifically, it indicates that neglecting the diagonal terms in Equation (111) is justified since they predict a vibronic intensity proportional to the first power of the phonon frequency (39). Similarly, crystal structures with a center of symmetry predict an intensity of the vibronic spectrum near the zero-phonon line proportional to the fifth power of the phonon frequency (40). Finally, it should be emphasized again that the phonon density of states as obtained above from the vibronic spectrum is really a good approximation only in the long wavelength limit. A more exact treatment requires a lattice dynamics model for the frequency dependence of the phonon wave vectors at different symmetry points away from the center of the Brillouin zone. Some attempt has been made to justify the extrapolation of predictions of the long wavelength limit into the short wavelength regions (2) but the validity of this is better demonstrated by the good agreement with other results in specific systems such as the one discussed here.

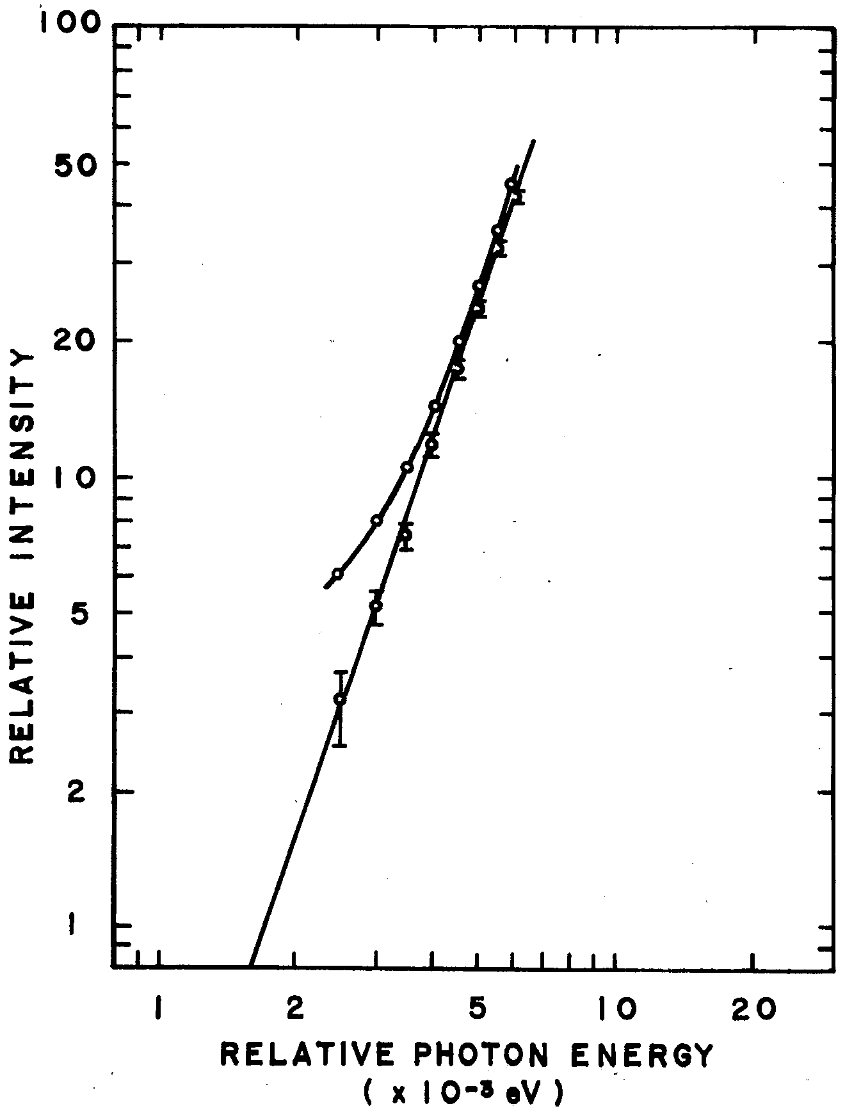

Figure 17. Intensity Change of the Vibronic Sideband Close to the Zero-Phonon Lines at 8°K. Curve shows the measured intensity and straight line is after subtracting a constant A=3.0 to fit the equation $I_s = A + B(\omega_0 - \omega)^n$, where B = 0.22 and n = 2.9.

High Energy Vibronics

The most interesting phonon modes in strontium titanate are the low frequency transverse optic soft modes responsible for the dielectric properties and the phase transition. These lie within about 0.0155 eV of the zero-phonon lines in the vibronic spectra. Although some faint structure is observed in this region in the low energy vibronic sideband of Cr^{3+} shown in Figure 11, it appears on the side of the very broad, intense band peaking near 0.0149 eV whose tail extends throughout this region. In an attempt to observe these low frequency modes more distinctly, we observed the vibronic sideband on the high energy side R lines in the fluorescence spectrum. At low temperatures the high energy vibronic transitions are less intense than the corresponding low energy transitions due to the lack of phonons available for absorption. However, the transition probability varies with temperature as

$$n(\omega_q) = \frac{1}{e^{\hbar\omega_q/kT} - 1} \tag{120}$$

and this predicts that the vibronics due to high frequency phonons will show a greater intensity decrease at low temperatures than those due to low frequency phonons.

Figure 18 shows the high energy vibronic sideband at several temperatures with a resolution of about 0.4A. The band peaking near 0.0149 eV is much less intense relative to the low frequency peaks than it was in the low energy sideband and a great amount of structure can be easily seen in this region. There are more than twenty peaks that can be seen in the spectra within 0.0155 eV of the zero-phonon lines. The positions of these peaks respect to the R_1 line at $40^{\circ}K$ are listed in Table X. As

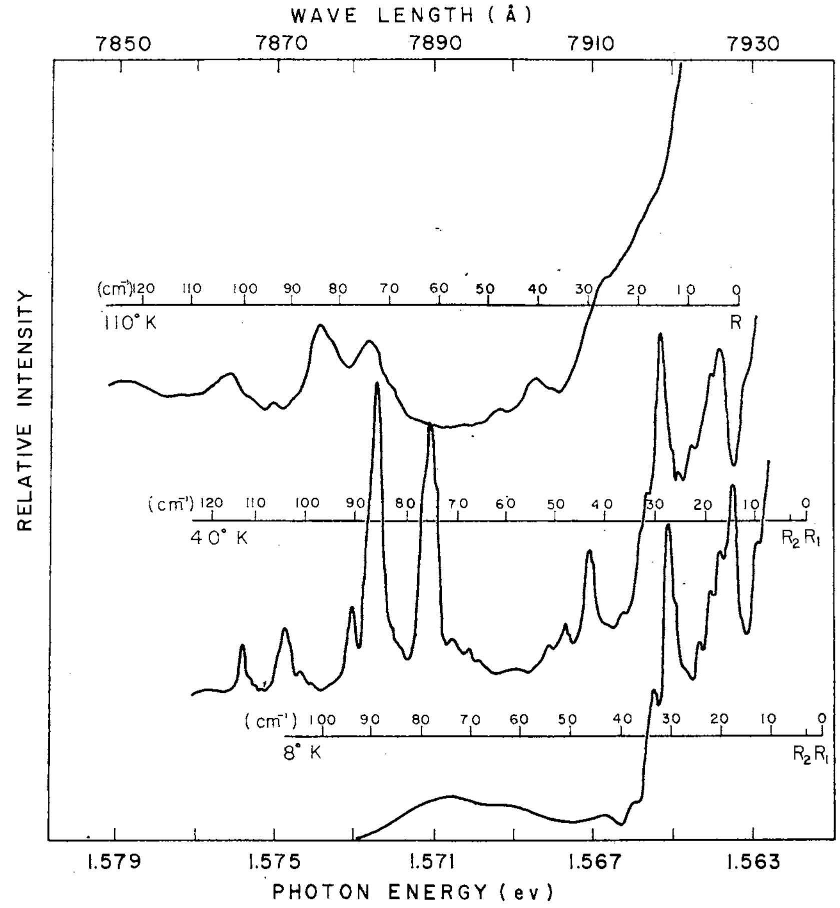

Figure 18. Low Frequency High Energy Vibronic Sidebands of $SrTiO_3:Cr^{3+}$ (0.02% wt) at 8^oK, 40^oK, and 110^oK

temperature is increased the whole spectrum, R-lines plus vibronics, shifts to higher energies. The vibronic peaks broaden and much of the structure is lost. The lowest temperature at which the most important peaks become prominent is indicated in the table.

Table X lists phonon frequencies observed by Raman scattering and neutron scattering in the same range as the vibronic peaks listed. No infrared results are listed because measurements have not been done at temperatures as low as 40°K and the only infrared active mode reported in this frequency range is the temperature dependent zero wave vector lowest transverse optic mode (8,12). Thus infrared absorption peaks reported in the literature occur at higher energies although they would be consistent with the vibronic peak at 0.0036 eV if extrapolated to low temperatures. The same statement is true for work done on the vibronic spectra of europium doped strontium titanate; data is reported at 77°K or above and the only peak seen in this frequency range is shifted to higher frequencies at these temperatures (28,29). For chromium and manganese doped samples low energy vibronic peaks have been reported (30) between 0.0124 eV and 0.0155 eV at low temperatures and the results are consistent with the three highest frequency high energy vibronic peaks listed in Table X.

It appears that all the peaks reported in Raman and neutron scattering data can also be observed in the vibronic spectra shown in Figure 18. Some differences in exact peak positions might be expected due to the effects of impurity ions in the crystal. In the octahedral phase all phonon modes are inactive in Raman scattering and observed peaks in the spectra must be due to two-phonon processes. In the tetragonal phase several first order peaks are observed. First order Raman scattering is

TABLE X

LOW FREQUENCY VIBRATIONAL MODES (eV FROM ZERO-PHONON LINES) OF STRONTIUM TITANATE

Vibronic (40^{o}K)	Raman (T^{o}K)(Ref.)	Neutron (T^{o}K)(Ref.)	Assignment
0.0015			
0.0021 (big at 8^{o}K)	0.0019 (40) (5)	0.019 (60) (6) 0.0019 (40) (7)	Γ_{25}(R), E_g (lowest TO mode)
0.0022			
0.0027			
0.0031			
0.0034			
0.0036 (big at 8^{o}K)	0.0027 (40) (5) 0.0035 (40) (13)	0.0027 (40) (7) 0.005 (90) (6)	$\Gamma_{15}(\Gamma)$, (lowest TO mode)
	0.0035 (8) (5)		Broad, Raman peak, probably second order
0.0038	0.0037 (79) (17)		Impurity induced local mode
0.0046			
0.0051			

TABLE X (Continued)

Vibronic (40°K)	Raman (T°K)(Ref.)	Neutron (T°K)(Ref.)	Assignment
0.0055 (big at 20°K)	0.0041 (78) (15) 0.0055 (77) (13) 0.0055 (40) (5) 0.0056 (20) (17) 0.0061 (4) (16) 0.0062 (125) (14)	0.0040 (60) (6) 0.0053 (40) (7)	Γ_{25}(R), A_{1g} (lowest TO mode)
0.0060			
0.0065			
0.0071			
0.0081	0.0082 (125) (14)	0.0081 (120) (7) 0.0087 (78) (6)	M_3 (lowest TA mode)
0.0084			
0.0088			
0.0093 (big at 40°K)	0.0091 (78) (15) 0.0093 (78) (16) 0.0097 (77) (13) 0.0101 (79) (17)		
0.0107 (big at 40°K)			Probably second order
0.0113 (big at 40°K)			
0.0125			

TABLE X (Continued)

Vibronic (40°K)	Raman (T°K) (Ref.)	Neutron (T°K)(Ref.)	Assignment
0.0129 (big at 40°K)		0.0130 (120) (7) 0.0134 (297) (6)	Σ_3(lowest TA mode)
		0.0133 (90) (6)	Λ_1 (lowest LA mode)
		0.0138 (297) (6)	M_3 (lowest TA mode M_2 (lowest TO mode)
		0.0143 (297) (6)	X_2 (lowest LA mode)
0.0140 (big at 40°K)	0.0145 (125) (14)	0.0145 (297) (6) (120) (7)	M_5 (lowest TO mode)
		0.0145 (297) (6)	
0.0151		0.0149 (297) (6) (120) (7)	X_5 (lowest TO mode) X_5 (lowest TA mode) M_5 (lowest LA mode) Λ_3 (lowest TA mode) Λ_1 (lowest LA mode)

limited to phonons with zero wave vector in order to conserve momentum and in the current model for the 110°K phase transition (5), the unit cell doubles causing the corner of the Brillouin zone (R-point) to become the zone center and thus permitting R-point phonons to be allowed in Raman scattering. Two of the observed first order peaks at low temperature are attributed to the $\Gamma_{25}(R)$ phonon mode whose degeneracy has been partially lifted by the lower symmetry.

The phonon frequencies listed in Table X from neutron scattering data were obtained from the zero-slope regions of the published dispersion curves.

The last column of Table X lists the suggested assignment of these lines. Most of these were determined from the dispersion curves obtained from neutron scattering. The type of branch and polarization at the center of the Brillouin zone are listed in parenthesis. Both neutron scattering (7) and Raman scattering (5) measurements have identified the splitting of the R-point Γ_{25} phonon mode at low temperatures and the symmetry designations of the two components are also listed. There are two possible second order peaks and one impurity induced local mode suggested by Raman data. The Raman peaks reported at 0.0082 eV and 0.0145 eV are probably second order processes since the M-point phonons which can appear in neutron scattering and vibronic spectra and not allowed in light scattering. Vibronic selection rules derived in Chapter II allow all of the suggested assignments. The rest of the unidentified vibronic peaks might be attributed to several sources; further symmetry splittings, impurity induced local modes or vibronics of the R_2 line. The 0.0093 eV peak which appears in both vibronic and Raman spectra but not neutron scattering may be due to a second order process.

It is interesting to note that the most prominent peaks in the vibronic spectra do not increase with temperature proportionally to the concentration of phonons given by Equation (120) as expected for high energy vibronics. Instead they increase to a maximum intensity at about 40°K and then decrease. Yamada and Shirane (7) report a similar temperature dependence of the intensity of the neutron scattering peak for the lowest TO mode with zero wave vector. They attribute this dependence to the temperature variation of the phonon frequency which appears in the denominator of the scattering cross section. A similar dependence appears in the vibronic transition probability as discussed in the previous section. The frequencies of the $\Gamma_{15}(\Gamma)$ mode and the two components of the $\Gamma_{25}(R)$ mode have also been shown to vary with temperature (6,7,5). Unfortunately, the tail of the zero-phonon line broadens and increases in intensity to the extent that the temperature dependence of the positions of the low-lying vibronic peaks can not be accurately determined.

CHAPTER V

RESULTS AND INTERPRETATION--ZERO-PHONON LINES AND THE LOCAL MODE

The interaction of lattice phonons with the transition electrons on the impurity ions gives rise to a temperature dependence of the zero-phonon lines. As temperature is raised they change in intensity, shift in position, and broaden, and the fluorescence lifetime decreases. Local vibrational modes shows a similar change in width, position and intensity with temperature due to their interaction with lattice modes. In this chapter we report the experimental data obtained for these temperature dependences in $SrTiO_3:Cr^{3+}$ and discuss possible interpretations using a Debye phonon distribution and using the effective phonon distribution obtained from the vibronic spectra as described in the previous chapter.

Temperature Dependences of the Width, Position, and Lifetime of the Zero-Phonon Lines

As mentioned in Section 3 of Chapter II the temperature dependence of the zero-phonon line comes from the quadratic coupling function $g_2(t)$ in Equation (75). In the region of the zero-phonon line in the limit of long times the linear coupling term $g_1(t)$ vanishes and using the asymptotic relation

$$\lim_{|t|\to\infty} \frac{(1-e^{ixt})}{x^2} = \pi|t|\ \delta(x) + i\ \pi \sin t\ \delta(x)$$

the quadratic term becomes

$$g_2(t) \simeq - \Gamma|t| + O(t), \tag{121}$$

where

$$\Gamma = \frac{\pi}{\hbar^2} \sum_{q_1 q_2} (V_{q_1 q_2})^2 (n_{q_1} + 1) n_{q_2} \delta(\omega_{q_1} - \omega_{q_2}). \tag{122}$$

Thus the zero-phonon spectral function is given by

$$\begin{aligned} G_o(ab;\omega) &= \int_{-\infty}^{\infty} dt\, e^{-i\omega t} e^{-(-i\omega_o t + S + i\Omega t + \Gamma|t|)} \\ &= e^{-S} \frac{2\Gamma}{(\omega_o - \omega - \Omega)^2 + \Gamma^2} . \end{aligned} \tag{123}$$

This describes a Lorentzian line centered about the frequency $\omega = \omega_o - \Omega$ and having a full width at half maximum equal to 2Γ. Both the line width and line position have a temperature dependence contained in the phonon frequencies as seen in Equations (122) and (73). The line intensity varies with temperature through the phonon occupation numbers in S as given in Equation (72).

Using the definition of the coupling coefficient in terms of the individual mode Huang-Rhys factors given in Equation (78), the temperature dependence of the line width and line position are given by

$$\Gamma = \bar{\alpha} \sum_q (\omega_q^2 s_q)^2 n_q(n_q + 1) , \tag{124}$$

$$\delta E = \Omega(T) - \Omega(T=0) = \alpha' \sum_q \omega_q^2 S_q n_q , \tag{125}$$

where $\bar{\alpha}$ and α' are coupling constants.

Let us first consider the temperature dependence of the line width. The most general expression for this can be written as the sum of contributions from three physical processes (33)

$$\begin{aligned}\Delta E(\mathrm{eV}) \;=\; & \Delta E_o + \alpha \int_0^\infty [g(\omega)]^2\, \omega^2 n(\omega)\, [n(\omega) + 1]\, d\omega \\ & + \sum_{f>i} \beta_{if}\, \omega_{if}\, n(\omega_{if})\, g(\omega_{if}) + \sum_{f<i} \beta_{if}\omega_{if} \\ & \times [n(\omega_{if}) + 1]\, g(\omega_{if}) \; . \end{aligned} \tag{126}$$

The second term is just the expression given in Equation (124) where the summation has been changed to an integral. It describes the broadening due to the continual absorption and emission of virtual phonons of different frequencies by the impurity ion (i.e., the Raman scattering of phonons). The first term represents the broadening due to the slightly different crystal field at the site of each impurity ion. It is generally considered to be independent of temperature. The last two terms are lifetime broadening contributions due to direct transitions to other electronic states through the absorption or emission of a real phonon, respectively. The temperature dependence of the width of a zero-phonon line is contained in the last three terms of Equation (126). These phonon processes predict a Lorentzian lineshape whereas the random strains described by the first term given a Gaussian shape. However, we approximate the combination of Gaussian and Lorentzian terms with a simple sum in Equation (126).

For chromium doped strontium titanate at low temperatures the R_1 line fluorescence will be broadened by direct phonon absorption transitions to the level from which the R_2 fluorescence line originates whereas the R_2 line will be broadened by the phonon emission process between these two levels. The strain broadening can be taken as the width of the R_1 line extrapolated to 0°K. The remaining question is what to take for the phonon density of states $g(\omega)$ in Equation (126). Here we consider three possibilities : a Debye distribution, the effective density of states obtained from vibronic spectra, and a delta function describing coupling to only one of the soft phonon modes.

For a Debye distribution (41,42)

$$\begin{aligned} g(\omega) &= \frac{3\,V\,\omega^2}{2\pi^2 v^3} \qquad \omega \le \omega_D \\ g(\omega) &= 0 \qquad\qquad \omega > \omega_D \end{aligned} \tag{127}$$

Using this in Equation (126) gives (33)

$$\Delta E(\mathrm{eV}) = \Delta E_o + \bar{\alpha}_D\,(T/T_D)^7 \int_o^{T_D/T} \frac{x^6\,e^x}{(e^x-1)^2}\,dx$$

$$+ \sum_{f>i} \omega_{if}^3\,\bar{\beta}_{if}^D\,n(\omega_{if}) + \sum_{f<i} \omega_{if}^3\,\bar{\beta}_{if}^D\,[n(\omega_{if}) + 1], \tag{128}$$

where

$$\bar{\alpha}_D = \frac{9h}{2\pi^3 (M/V)^2 v^{10}} \left(\frac{kT_D}{\hbar}\right)^7 \left[\sum_{j\neq i} \frac{|\langle\Psi_i^{el}|V_1|\Psi_j^{el}\rangle|^2}{E_i^{el} - E_j^{el}} + \langle\Psi_i^{el}|V_2|\Psi_i^{el}\rangle\right]^2 ,$$

and

$$\bar{\beta}_{if}^D = \frac{3h}{2\pi (M/V) v^5 \hbar}\,|\langle\Psi_f^{el}|V_1|\Psi_i^{el}\rangle|^2 \,. \tag{129}$$

This expression has been used to interpret data obtained on the temperature dependence of the linewidth of the Cr^{3+} R lines in several different hosts (41-43). T_D, $\bar{\alpha}_D$ and $\bar{\beta}^D_{if}$ are treated as adjustable parameters. The value obtained for the Debye temperature is generally not the value obtained from specific heat measurements since phonons of different frequency may contribute differently to the different types of physical processes.

For using the effective density of phonon states obtained from vibronic spectra the integral in the second term of Equation (126) can be re-written as a summation over the individual mode Huang-Rhys factors as in Equation (124)

$$g(\omega) = \omega_q G_1(\omega) = 2\pi\, e^{-S} \sum_q S_q \omega_q \delta(\omega_o - \omega - \omega_q) \; . \qquad (129)$$

$$\Delta E(eV) = \Delta E_o + \bar{\alpha}_e \sum_q (\omega_q^{\,2} S_q)^2\, n_q(n_q+1) + \sum_{f>i} \bar{\beta}^e_{if}\, n(\omega_{if})\, \omega_{if}^2 S_{if} + \sum_{f<i} \bar{\beta}^e_{if}\, [n(\omega_{if}) + 1]\, \omega_{if}^2 S_{if} \; . \qquad (130)$$

The values used for S_q are those obtained from the one-phonon contribution to the vibronic sideband through the computer iteration process described in Chapter II. $\bar{\alpha}_e$ and $\bar{\beta}^e_{if}$ are coupling constants which again are treated as adjustable parameters. The second term in this expression has been used to interpret the temperature dependence of the width of the zero-phonon line of the M-center in MgF_2 (44).

The final method of treating the Raman scattering term is to consider coupling to only one specific phonon mode. This may be important in strontium titanate where specific transverse optic phonons play such an important role in other physical properties of the material. In this case the phonon density of states can be written as a delta function

$$g(\omega) = \delta(\omega_o - \omega - \omega_s) \, , \tag{131}$$

so the linewidth contribution is given by

$$\Delta E(\mathrm{eV}) = \Delta E_o + \bar{\alpha}_s \, \omega_s{}^2 \, n(\omega_s)[n(\omega_s) + 1] \, . \tag{132}$$

This type of expression has been used to interpret the temperature dependence of the width of one of the zero-phonon lines of europium in strontium titantate (45).

Similar phonon processes cause the positions of zero-phonon lines to shift with temperature. The change in position from the extrapolated energy of the line at 0^oK is given by (33)

$$\begin{aligned} \delta E(\mathrm{eV}) = {} & \alpha' \int_o^\infty n(\omega_q) \, \omega_q g(\omega_q) \, d\omega_q \\ & + \sum_{j<i} \beta'_{ij} \int_o^\infty n(\omega_q) \, \omega_q \, g(\omega_q) \, \frac{|E_i^{el} - E_j^{el}|}{(E_i^{el} - E_j^{el})^2 - (\hbar\omega_q)^2} \, d\omega_q \\ & + \sum_{j>i} \beta'_{ij} \int_o^\infty n(\omega_q) \, \omega_q g(\omega_q) \, \frac{|E_i^{el} - E_j^{el}|}{(E_i^{el} - E_j^{el})^2 - (\hbar\omega_q)^2} \, d\omega_q \, , \end{aligned} \tag{133}$$

where α' and β'_{ij} are again treated as adjustable parameters. The first term is just Equation (125) with the summation replaced by an integral. It describes the effect of the impurity ion continually absorbing and emitting virtual phonons of the same frequency. The other two terms are for the emission or absorption of real phonons causing transitions to lower or higher electronic states, respectively.

For $SrTiO_3:Cr^{3+}$ the R_1 line is effected by phonon absorption processes and the R_2 line by phonon emission processes as described above. The density of states in the phonon scattering term can again be represented by a Debye distribution, the effective density of states obtained from the one-phonon vibronic sideband, or a delta function for coupling to a single phonon mode:

$$\delta E(\mathrm{eV}) = \alpha_D'(T/T_D)^4 \int_0^{T_D/T} \frac{x^3}{e^x-1}\,dx + \sum_{j<i} \beta_{ij}'^D (T/\Delta E_{ij})^2\, P\int_0^{T_D/T} \frac{x^3}{e^x-1}\,\frac{1}{x^2-(\frac{\Delta E_{ij}}{kT})^2}\,dx - \sum_{j>i} \beta_{ij}'^D (T/\Delta E_{ij})^2\, P\int_0^{T_D/T} \frac{x^3}{e^x-1}\,\frac{1}{x^2-(\Delta E_{ij}/kT)^2}\,dx\,, \qquad (134)$$

$$\delta E(\mathrm{eV}) = \alpha_e' \sum_q \omega_q^2 S_q n_q + \sum_{j<i} \beta_{ij}'^e \sum_q S_q \omega_q^2\, n(\omega_q) \frac{\Delta E_{ij}}{\Delta E_{ij}^2-(\hbar\omega_q)^2} - \sum_{j>i} \beta_{ij}'^e \sum_q S_q\, \omega_q^2\, n(\omega_q) \frac{\Delta E_{ij}}{\Delta E_{ij}^2-(\hbar\omega_q)^2} \qquad (135)$$

$$\delta E\ (\mathrm{eV}) = \alpha_s'\, \omega_s\, n(\omega_s)\,, \qquad (136)$$

where

$$\alpha_D' = \frac{3h}{4\pi(M/V)v^5} \left(\frac{kT_D}{\hbar}\right)^4 \left[\sum_{j\neq i} \frac{|\langle\Psi_i^{el}|V_1|\Psi_j^{el}\rangle|^2}{E_i^{el}-E_j^{el}} + \langle\Psi_i^{el}|V_2|\Psi_i^{el}\rangle\right].$$

β'^{D}_{ij} is given above and α'_e, α'_s and β'^{e}_{ij} are similar constants. P denotes the principal part of the integral.

Table XI and XII list the experimental data obtained on the widths and positions of the R lines of $SrTiO_3:Cr^{3+}$ at different temperatures and gives their changes in widths and positions from their values at 0°K. These data were obtained using the monochromator in second order to achieve a resolution of 0.4A. The estimated accuracy of these measurements is about 2% for the line widths and 0.01% for the line positions. These data are plotted in Figures 19 and 20 along with the best fits obtained from the theories discussed above. It was found that changes of 2.5% in the assumed 0°K values did not affect the theoretical fitting of the data and changed the values of the adjustable fitting parameters by less than 7.9%. Note that only a small discontinuity occurs these temperature dependences near the phase transition at 110°K. No discontinuity can be detected near 35°K.

The solid lines in Figures 19 and 20 represent the predictions of Equations (128) and (134) where the virtual phonon terms have been written in terms of the Debye distribution. The adjustable parameters used in obtaining these fits are listed in Table XIII. They have an accuracy about 4.3%. The values obtained for the coupling parameters of the virtual phonon processes are significantly less than those needed for Cr^{3+} in Al_2O_3 and those for the real phonon processes are significantly greater than in ruby (46). Also the line shift parameter α'_D is positive in this case whereas it was negative for ruby. The effective Debye temperature needed to fit the data is less than the value of 400°K obtained from specific heat measurements which implies that the lower frequency phonons make greater contributions to the broadening and shift-

TABLE XI

WIDTHS OF THE ZERO-PHONON LINES OF $SrTiO_3:Cr^{3+}$ (0.02% WEIGHT) AT VARIOUS TEMPERATURES

T(°K)	Widths		Width Changes From T = 0°K*	
	ΔE_{R_1} (eV x 10^{-4})	ΔE_{R_2} (eV x 10^{-4})	$\Delta E_{R_{10}}$ (eV x 10^{-4})	$\Delta E_{R_{20}}$ (eV x 10^{-4})
8.0	1.41588	1.17990	0.02588	0.02990
20.0	1.47798	1.27926	0.08798	0.12926
40.0	2.62062	1.67670	1.23062	0.52670
60.0	4.14828	3.15468	2.74828	2.00468
80.0	5.82498	5.82498	4.43498	4.67498
100.0	7.50168	7.50168	6.11168	6.35168
110.0	7.99848	7.99848	6.60848	6.84848
120.0	8.89272	8.89272	7.70272	7.74272
200.0	26.57880	26.57880	25.18880	25.42880

*Exploted line width at T = 0; $\Delta E_{R_{10}}$ (T=0) = 1.39000 x 10^{-4} eV; $\Delta E_{R_{20}}$ (T=0) = 1.15000 x 10^{-4} eV.

TABLE XII

POSITIONS OF THE ZERO-PHONON LINES OF $SrTiO_3;Cr^{3+}$ (0.02% WEIGHT) AT VARIOUS TEMPERATURES

T(°K)	Positions (eV)		Shifts From the Positions at T=0°K*	
	E_{R_1}	E_{R_2}	$\delta\ E_{R_1}$ (X 10^{-4} eV)	$\delta\ E_{R_2}$ (X 10^{-4} eV)
8	1.561709	1.562141	0.09	0.01
20	1.561783	1.562151	0.83	0.11
40	1.562106	1.562472	4.06	3.32
60	1.562576	1.562791	8.76	6.51
80	1.563116	1.563116	14.16	9.76
100	1.563443	1.563443	17.43	13.03
110	1.563727	1.563727	20.27	15.87
120	1.564260	1.564260	25.60	21.20
200	1.567642	1.567642	59.42	55.02

*Exploted line positions at T=0; E_{R_1} (T=0) = 1.561700 eV; E_{R_2} (T=0) = 1.562140 eV.

TABLE XIII

ADJUSTIBLE PARAMETERS FOR THE FITS OF THE ZERO-PHONON LINES WIDTHS AND LINE SHIFTS OF $SrTiO_3:Cr^{3+}$ (0.02% WEIGHT)

Parameters		R_1 Line	R_2 Line
Line Width	T_D	115°K	115°K
	$\bar{\alpha}_D$	3.3950×10^{-3} eV	4.0050×10^{-3} eV
	$\bar{\beta}_{if}^{D}$	1.7902×10^{5} $(eV)^{-2}$	4.3887×10^{4} $(eV)^{-2}$
	$\bar{\alpha}_e^{\omega}$	2.8562×10^{7} eV	2.9355×10^{7} eV
	$\bar{\beta}_{if}^{e\omega}$	2.6536×10^{2} $(eV)^{-1}$	1.5653×10^{2} $(eV)^{-1}$
	$\bar{\alpha}_e^{f}$	7.0876×10^{8} eV	7.2534×10^{8} eV
	$\bar{\beta}_{if}^{ef}$	1.9315×10^{2} $(eV)^{-1}$	8.6905×10 $(eV)^{-1}$
	$\bar{\alpha}_s$	7.8192 eV	7.8192 eV
Line Shift	T_D	115°K	115°K
	α'_D	9.7660×10^{3} eV	9.7660×10^{3} eV
	β'^{D}_{if}	1.0910×10^{-7} eV	1.0910×10^{-7} eV
	α'^{ω}_e	2.8660×10^{2} $(eV)^{3}$	2.8660×10^{2} $(eV)^{3}$
	$\beta'^{e\omega}_{if}$	1.0910×10^{-7} eV	1.0910×10^{-7} eV
	α'^{f}_e	1.0411×10^{2} eV	1.0385×10^{2} eV
	β'^{ef}_{if}	1.0910×10^{-7} eV	1.0910×10^{-7} eV
	α'_s	2.4061×10^{-1} eV	2.4061×10^{-1} eV

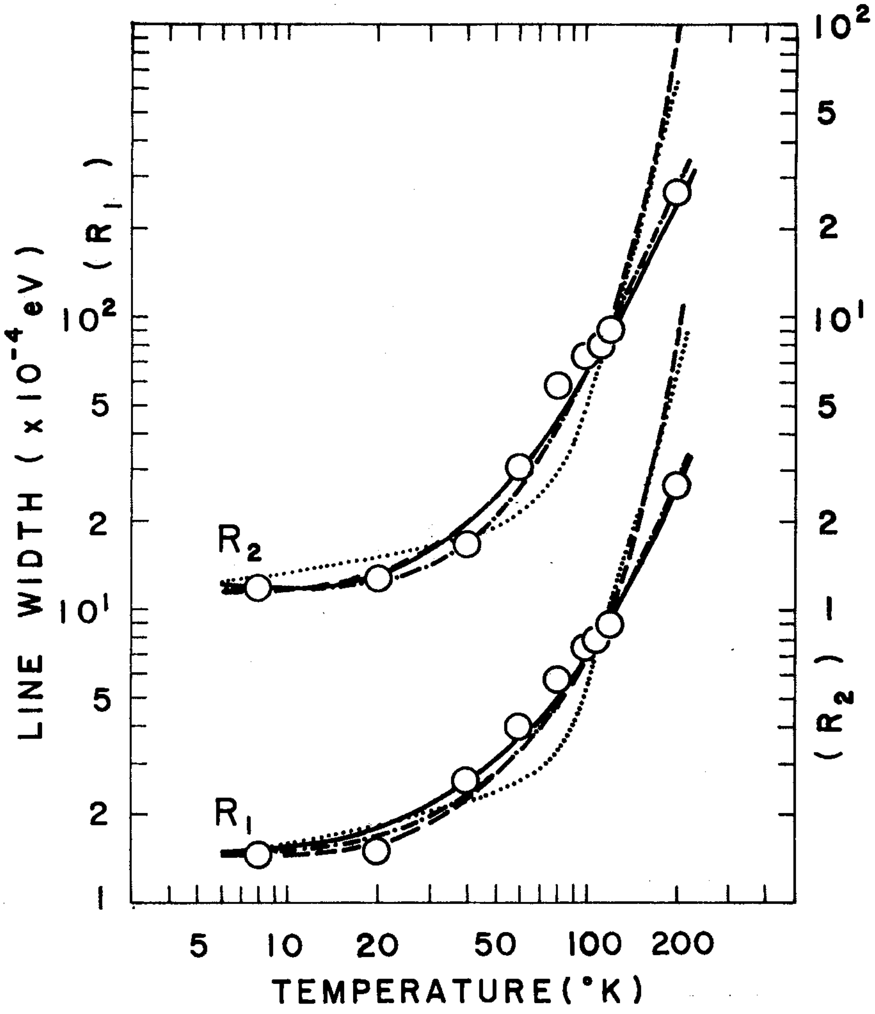

Figure 19. Line Widths of the Zero-Phonon Lines of SrTiO$_3$:Cr^{3+} (0.02% Weight). Circles are measured ones. Solid line (——) shows the best fit of Deby Approximation to the data. Dashed lines are the best fits of the theories: —·—·—; taken only the 1st peak of the computer output as its effective one-phonon density of states, ·····; whole bands as its effective one-phonon density of states and —·—; zone-center soft phonon mode only taken as its effective one phonon density of states. All constants used to fit are shown in Table XIII.

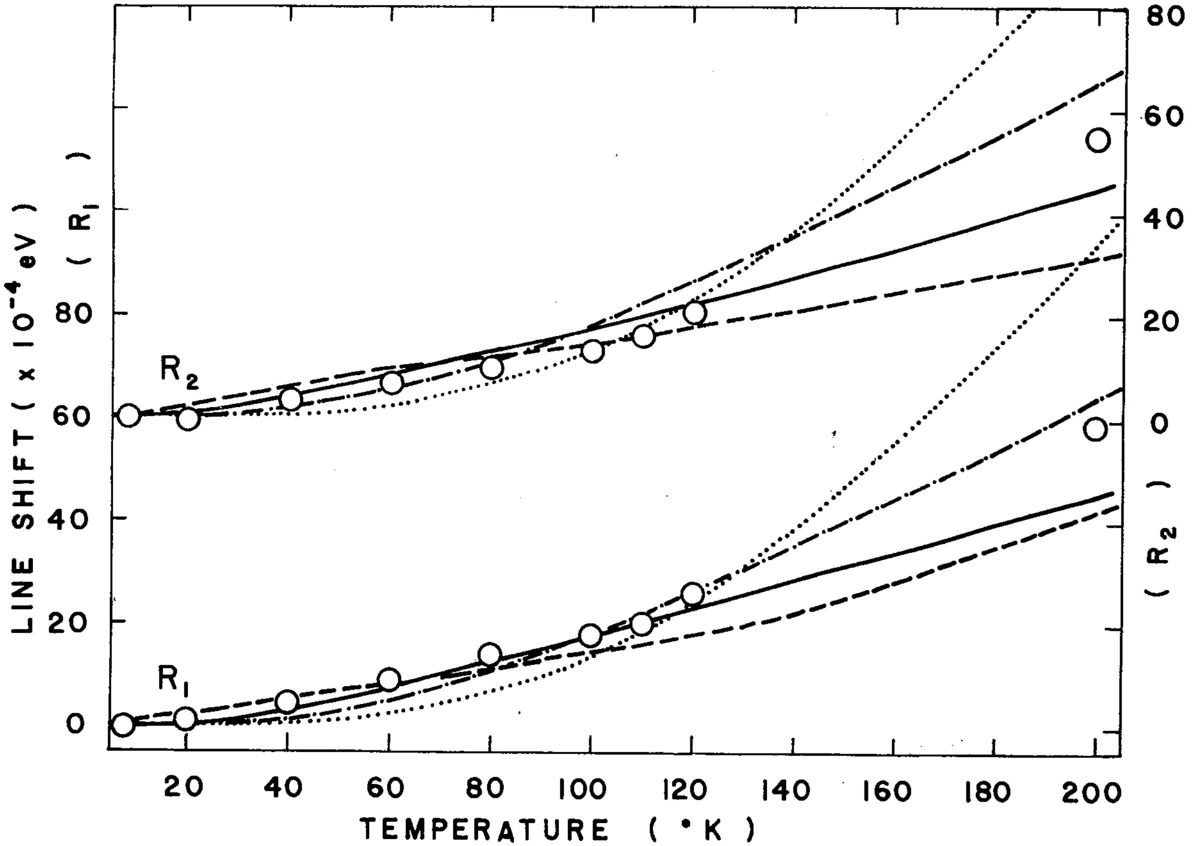

Figure 20. Line Shifts of the Zero-Phonon Lines of SrTiO$_3$:Cr^{3+} (0.02% wt). Circles show measured ones. Various densities of states were used to fit the data. Solid line shows Deby Approximation. Other lines show the best fit to the data with the first band (-·-·-), whole bands (····) of the computed effective one-phonon sideband, and zone-center soft mode (-·—-) only as their density of states. All parameters used for these fits are listed in Table XIII.

ing processes than high frequency phonons do. Note that due to the phase transition ω_{if} will not be a constant but decrease to zero at 110°K. Assuming no frequency dependence for V_1 in the Debye approximation, the direct process terms for the line broadening should vary approximately as the third power of the splitting of the R_1 and R_2 lines which is shown explicitly in Equation (128) to be reasonably correct.

If the one-phonon vibronic sideband is used as an effective density of states in Equations (130) and (135) the dotted lines in Figures 19 and 20 are obtained which do not fit the data well at high temperatures. If only the first few peaks of the sideband are considered as the effective density of states (say out to 0.0467 eV) then a good fit to the data can be obtained. The dotted-and-dashed lines in Figures 19 and 20 are obtained using the parameters listed in Table XIII and including only the first vibronic peak (out to 0.0303 eV) in the density of phonon states. This again indicates that low frequency phonons are more important than high frequency phonons in causing the broadening and shifting of zero-phonon lines with temperature.

The thermal expansion of the lattice can also contribute to the temperature dependence of the line position. The change in lattice constant is due to the anharmonicity of lattice modes which in turn leads to a change in force constants. This can cause either a positive or negative shift in frequency depending on the overlapping of wavefunctions. By analogy to hydrostatic pressure measurements on ruby, Stokowski and Schawlow (32) determined that this should cause the R line of $SrTiO_3:Cr^{3+}$ to exhibit a shift to higher energies proportional to the change in lattice constant

$$\frac{\delta\tilde{\nu}}{\nu} \propto \frac{\Delta a}{a} .$$

Using the x-ray diffraction data of Lytle (3) and the elastic compliances obtained from the results of Rupprecht and Winter (47), they conclude that the effects of this mechanism are an order of magnitude too small to explain the observed results. Calculations by Slonczewski (48) indicate that the tetragonal distortion of the crystal field makes the dominant contribution to the shift of the R lines at low temperatures. This causes a discontinuity in the slope of the lineshift versus temperature near the 110°K phase transition. Since this discontinuity also appears in the slope of the average position of the R_1 and R_2 lines it can not be attributed to the effects of direct process mechanisms. It may, however, be accounted for by a change in the coupling parameter α'_D, as the crystal field changes from tetragonal to cubic. This is reasonable since α'_D depends on the matrix element of the electron-phonon coupling constant as shown in Equation (134).

The third method of attempting to fit the data is to assume coupling to only one of the soft phonon modes. This seems like a reasonable model since the other two approaches both indicate that low frequency phonons make the dominent contribution to the thermal broadening and shifting of the zero-phonon lines. The predictions of this model for both the Γ-point and the two components of the R-point soft modes are shown as dashed lines in Figures 19 and 20. The temperature dependences of the soft mode frequencies are taken from references (6) and (7). These theoretical curves show large discontinuities in their temperature dependencies which are obviously inconsistent with the experimental data. Such discontinuities were observed in the data obtained on $SrTiO_3:Eu^{3+}$ (45).

Stokowski and Schawlow (32) also reported data on the temperature dependence of the position of the R lines in chromium doped strontium titanate and our data is consistent with theirs. They show that the line-shift is not directly proportional to the total heat of the host crystal as predicted by the first term in Equation (134). Instead the line-shift is found to be proportional to the reciprocal of the dielectric constant which in turn is proportional to the square of the soft mode frequency. They conclude that the anharmonic phonon interaction parameters must be similar to the electron-phonon coupling parameters. However, this does not predict the slight discontinuity in the line-shift near 110°K.

Figure 21 shows the variation of the fluorescence decay time as a function of temperature. These data are also listed in Table XIV. The ratio of the integrated fluorescence intensity of the R lines to that of the total spectrum is also listed in the table at different temperatures. Theoretically this ratio can be expressed as

$$I_R/I_T = W_R/(W_R + W_{VIB}) \tag{137}$$

where W_R and W_{VIB} represent the radiative and vibronic transition rates, respectively. The measured fluorescence decay time can be expressed as

$$\tau_F^{-1} = W_R + W_{VIB} + W_{NR} \tag{138}$$

where W_{NR} represents the non-radiative transition rate. If radiationless processes are not important, the intensity ratio and fluorescence lifetime are related by

$$I_R/I_T = W_R \tau_F \tag{139}$$

where the radiative transition rate is generally independent of tempera-

TABLE XIV

TEMPERATURE DEPENDENCE OF FLUORESCENCE DECAY TIME OF THE ZERO-PHONON LINE OF $SrTiO_3:Cr^{3+}$ (0.02% WEIGHT) AND RATIO OF INTEGRATED INTENSITY WITH RESPECT TO THAT OF TOTAL SIDEBAND

$T(^oK)$	Decay Time (msec)	Intensity Ratio (I_R/I_T)
8		0.38783
10	17.751	
20		0.36317
40	17.817	0.34517
60		0.33941
77		0.28861
80	16.168	
100	14.629	0.28741
110		0.28012
120	13.294	0.22340
150	11.767	0.15614
200		0.05604

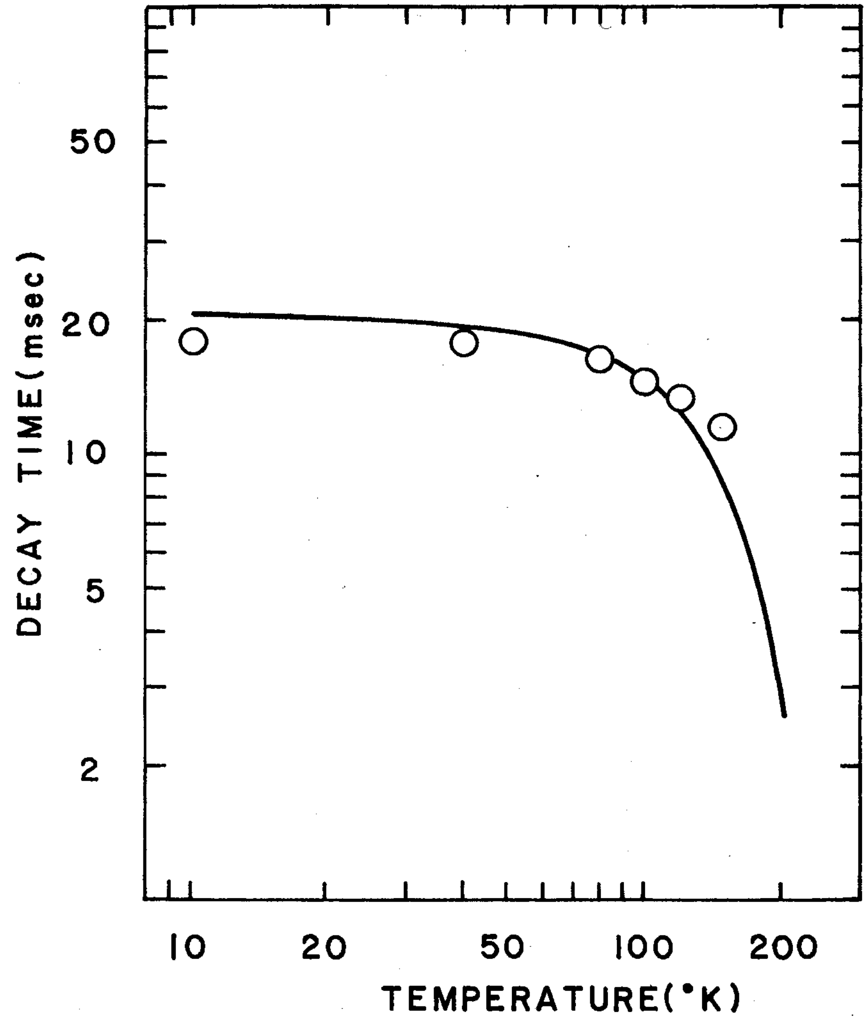

Figure 21. Temperature Dependence of the Decay Time of Cr^{3+} in $SrTiO_3$. Circles show measured decay times. Integrated intensity ratio of the zero-phonon on line to that of total sideband was compared with fitting parameter $W_R = 18.345\ sec^{-1}$.

ture. The solid line in Figure 21 is a plot of the intensity ratio adjusted to fit the decay time at low temperatures with $W_R = 18.4\ \mathrm{sec}^{-1}$. The fact that it falls below the lifetime data above 100°K indicates the increasing importance of radiationless processes in this temperature range.

Temperature Dependences of the Widths, Positions, and Intensities of the Local Mode

Impurity ions in crystals may have different vibrational characteristics than the pure lattice phonons depending on their mass and force constant differences with respect to the normal host ions. For impurities with lighter masses or smaller force constants, nonpropagating vibrational modes of the impuritiy ion and its immediate surroundings can occur at frequencies where normal lattice vibrations may not occur. These are called local modes if they are at higher frequencies than the highest frequency phonon mode, gap modes if they occur in a forbidden gap between phonon branches, and band or resonant modes if they fall within an allowed frequency band of lattice phonons. The term "local mode" is generally applied to all three cases. There has been much experimental and theoretical work done in studying local modes in alkali halides and this is reviewed in references (50) and (51). The interest in these studies has been twofold: to understand the intrinsic vibrational properties of defects in crystals and to elucidate the interactions between the local modes and the lattice phonons. Experimentally nearly all of the work has been done with infrared spectroscopy. The temperature dependences of the widths, positions, and intensities of local mode absorption in the infrared spectra have been investigated along with the appearance of structured sidebands with some of the local modes.

We have investigated the temperature dependence of the width, position, and intensity of the local mode vibronic peak induced by the presence of chromium impurities in strontium titanate. Although local modes have previously been identified in vibronic spectra, this is the first investigation of the temperature dependence of local modes using vibronic spectroscopy. The results are interpreted in terms of the anharmonic interactions between the local mode and lattice phonons and are compared with the earlier infrared work on alkali halides.

Because of size similarities, Cr^{3+} probably goes into the strontium titanate lattice substitutionally for Ti^{4+} ions. This requires some charge compensating mechanism such as an oxygen vacancy which probably takes place non-locally since room temperature electron spin resonance measurements show the chromium ion to occupy a site of cubic symmetry (52). Stokowski and Schawlow (30) were the first to study the vibronic spectrum of $SrTiO_3:Cr^{3+}$ and they attributed the peak at 0.0706 eV to a local mode induced by the chromium ion since it did not appear in the vibronic spectrum of manganese doped strontium titanate and could not be correlated with any of the known lattice phonon frequencies. Because Cr^{3+} and Mn^{4+} are both heavier than Ti^{4+} the local mode is probably induced by force constant changes. These may be associated with the charge defect which is not present in manganese doped samples. Since the normal mode phonon frequencies extend to about (6,7) 0.0943 eV the observed sharp peak in the spectrum is not a local mode in the strict definition. It lies on the high energy side of an unresolved band containing contributions from $TO_4(\Gamma)$ and $LO_3(\Lambda)$ phonons among others as shown in Figure

23 at two temperatures. It appears to be more like a gap mode at low temperatures and a band resonant mode at high temperatures. However, for simplicity's sake we will continue to use the general term of "local mode". As temperature is raised the whole spectrum shifts to higher energies and the local mode broadens and decreases in intensity. It should also be mentioned that the two-phonon emission peak for this local mode appears in the spectrum at 0.1420 eV from the R_1 line.

Figures 23-25 shows the variation of the local mode line width, position and intensity with temperature. These data are listed in Tables XV-XVII. The full width at half maximum is constant at low temperatures and increases approximately as T^2 at high temperatures. The peak position relative to the R_1 line exhibits a slightly greater than linear shift to higher energy with increasing temperature. The integrated intensity of the local mode peak is constant at low temperatures and decreases sharply at higher temperatures. The accuracy in these experimental points is estimated to be about ±10% for the line width, ±20% for the integrated intensity, and $\pm 1.24 \times 10^{-4}$ eV for the line shift. The largest source of error arises from having to separate the local mode from the nearby vibronic band (see Figure 22).

The temperature dependent characteristics of the local mode are due to its interaction with the lattice phonons which takes place through anharmonic terms in the lattice potential. The local mode is treated as an Einstein oscillator and a Debye distribution is generally assumed for the normal modes of the lattice. The temperature dependence is contained in the phonon occupation numbers given by Equation (120). The mathematical descriptions of the important multiphonon processes were originally developed to explain results of Mössbauer or zero-phonon line

TABLE XV

LINE WIDTHS OF THE LOCAL MODE IN $SrTiO_3:Cr^{3+}$ (0.02% WEIGHT) AT VARIOUS TEMPERATURES

T(^oK)	Widths (x 10^{-4} eV)			$\Delta E-\Delta E_o^*$
	Local Mode	Zero-Phonon Lines (Average)	Differences (ΔE)	
8	16.950 ± 7%	1.298	15.652	
20	17.940	1.329	16.611	0.311
40	18.670	1.849	16.823	0.523
60	21.180	3.651	17.529	1.229
80	23.370	5.825	17.545	1.245
100	25.160	7.502	17.658	1.358
110	26.970	7.998	18.972	2.672
120	30.585	8.893	21.692	5.392
170	66.690 ± 15%	26.910	39.780	23.480

*$\Delta E_o = 16.3 \times 10^{-4}$ eV.

TABLE XVI

LINE SHIFTS OF THE LOCAL MODE IN $SrTiO_3:Cr^{3+}$ (0.02% WEIGHT) AT VARIOUS TEMPERATURES

T (^oK)	Position (eV)	Shifts From the Position at T=^oK* (x 10^{-4} eV)
8	1.4913090	0.090
20	1.4913497	0.497
40	1.4913124	0.124
50	1.4914738	1.738
60	1.4916600	3.600
80	1.4915483	2.235
100	1.4915483	2.483
110	1.4914862	1.862
120	1.4916104	3.104
150	1.4920076	7.076
170	1.4918214	5.214
200	1.4922931	9.931

*δE (T=0^oK) = 1.4913000 eV.

TABLE XVII

RATIO OF THE INTEGRATED INTENSITY OF THE LOCAL MODE WITH RESPECT TO THAT OF SIDEBANDS OF $SrTiO_3:Cr^{3+}$ (0.02% WEIGHT) AT VARIOUS TEMPERATURES

$T(^oK)$	Ratio (I_L/I_T)
8.4	0.05372
20	0.05367
40	0.05081
60	0.04382
77	0.03710
100	0.03074
110	0.02915
120	0.02715
150	0.00235

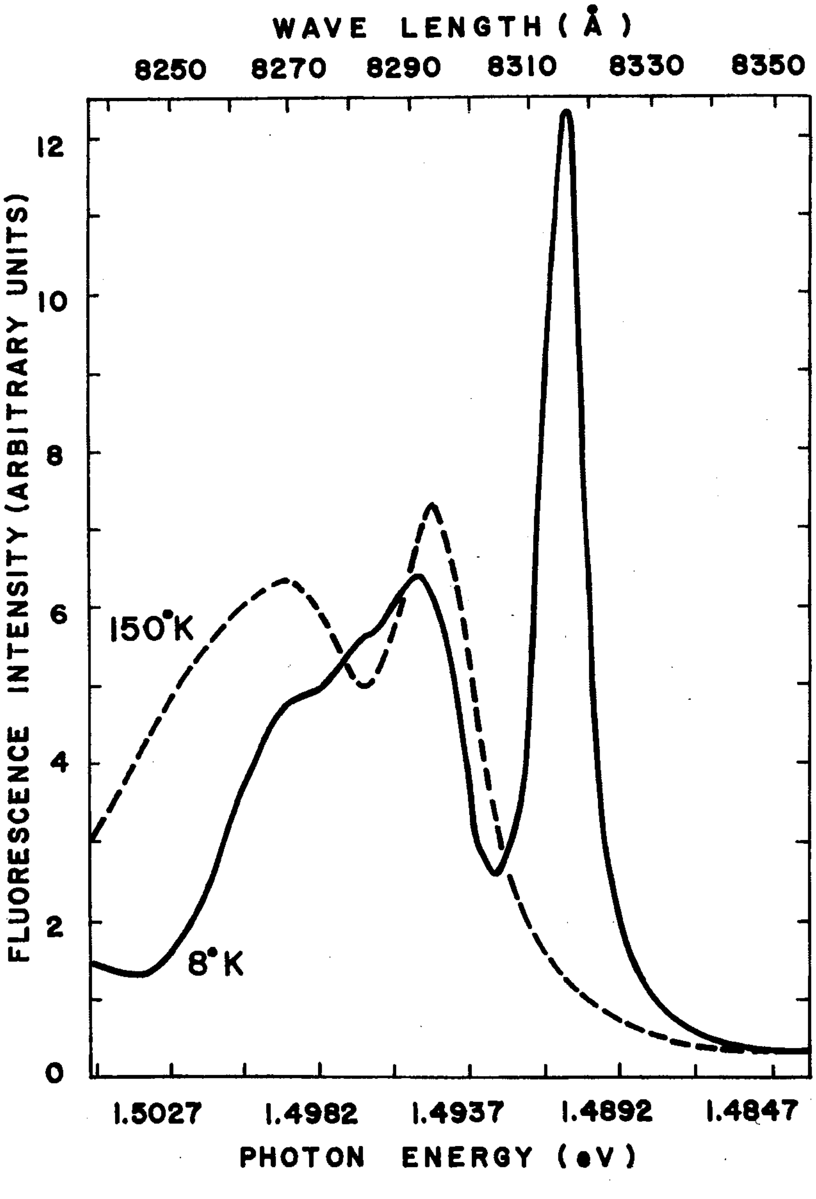

Figure 22. Vibronic Spectrum of $SrTiO_3:Cr^{3+}$ (0.02% Weight) in the Region of the Local Mode at 8 and 150°K

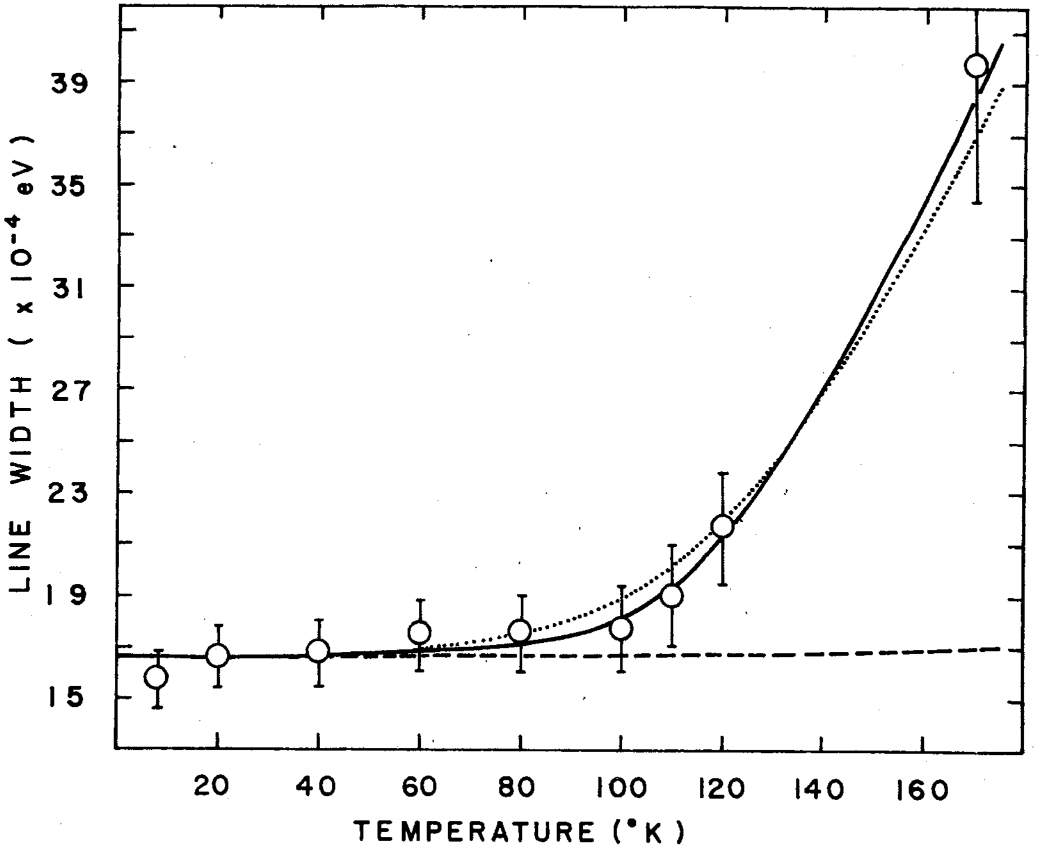

Figure 23. Temperature Dependence of the Line Width of the Local Mode Vibronic Peak in $SrTiO_3:Cr^{3+}$ (0.02% Weight). Circles show measured line width. Dashed line shows the direct term contribution to the width and solid and dotted lines show the best fit to the data using Debye Approximation and the computed effective one-phonon sideband as their phonon density of states. Fitting parameters are listed in Table XVIII.

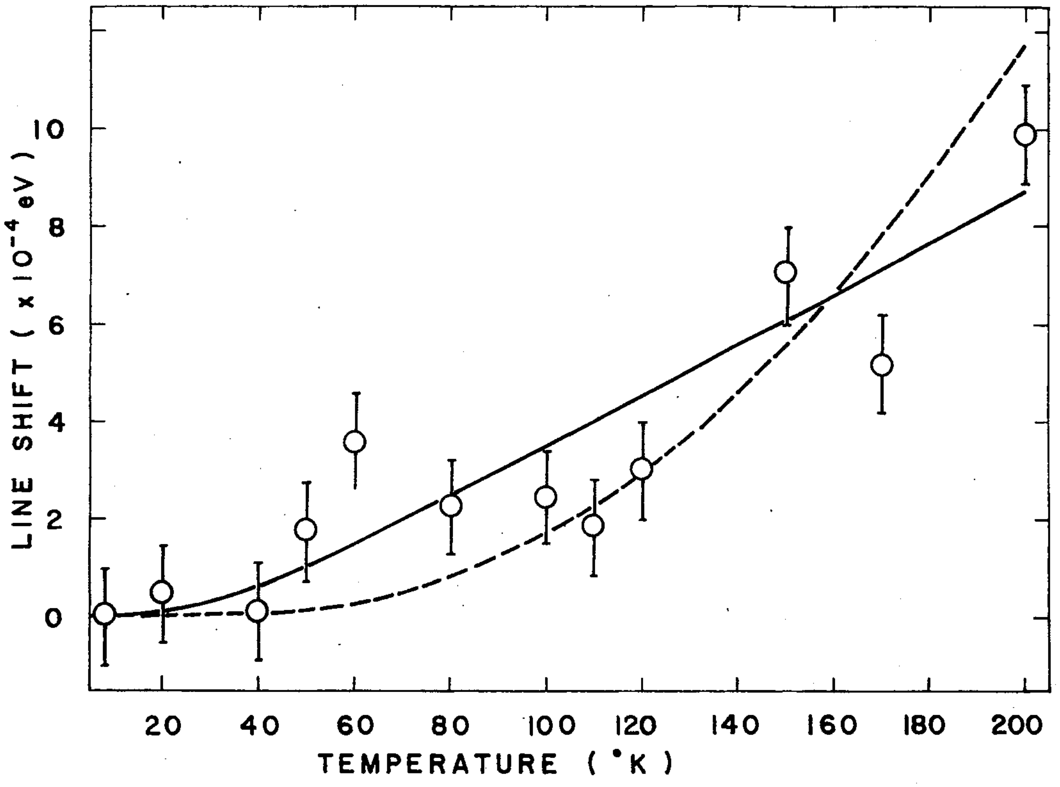

Figure 24. Temperature Dependence of the Position of the Local Mode Vibronic Peak. Circles show the line positions measured. Solid line shows Deby Approximation with $T_D = 115^oK$, $\alpha_D' = 1.9016 \times 10^{-3}$ eV and $\beta_{if}'^{D} = 0$, and the fit with computed effective one-phonon sideband is represented by dashed line. The fitting parameters are $\alpha_e' = 5.7158$ eV and $\beta_{if}'^{e\omega} = 0$.

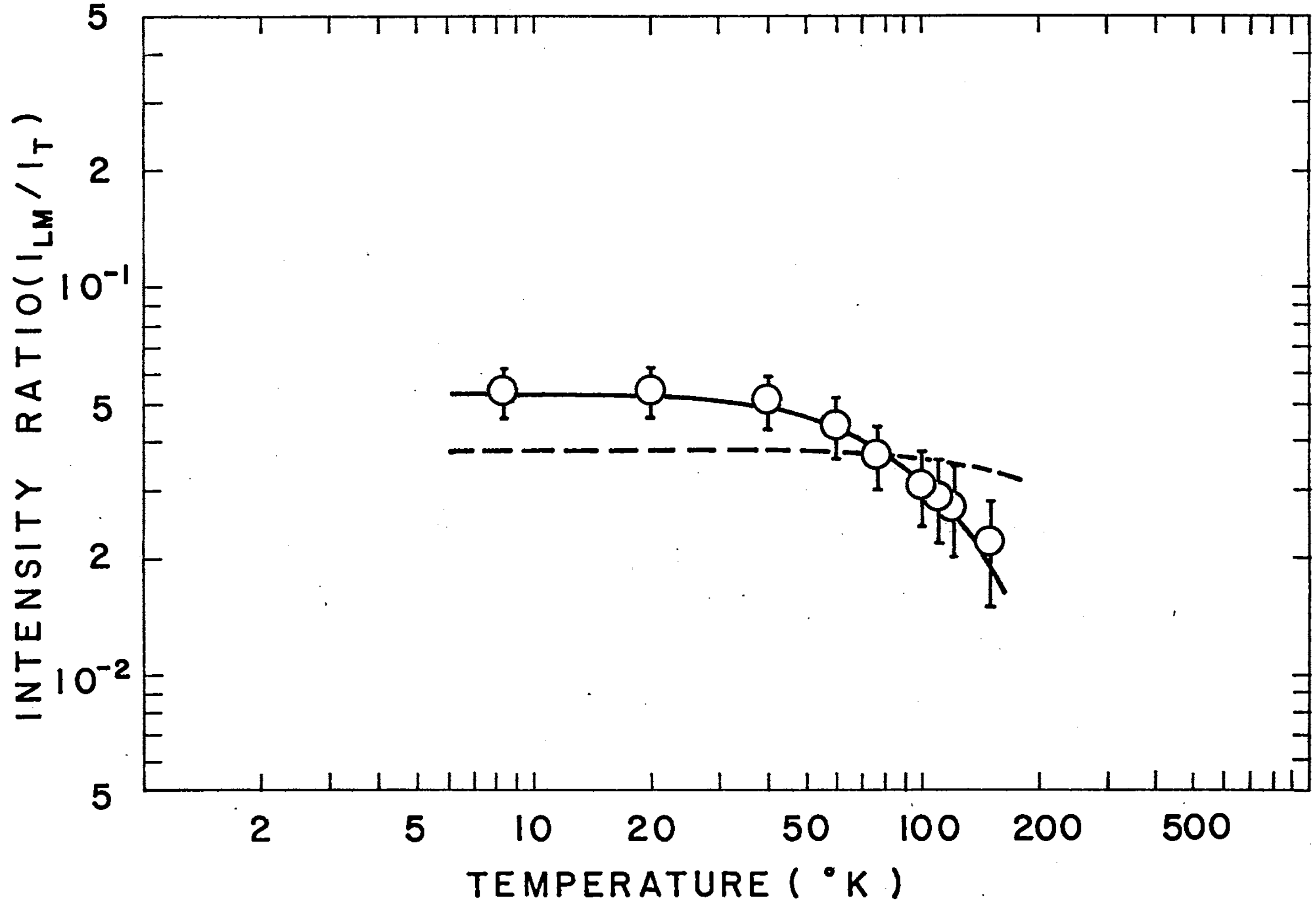

Figure 25. Temperature Dependence of the Intensity of the Local Mode Vibronic Peak. Circles show the measured ratio of the local mode to the total integrated intensity. Solid line shows the best fit to the data by the Debye Approximation with $\theta_D'' = 650^\circ$K and S = 2.946. Dashed line shows the best fit to the data by the computed effective one-phonon sidebands with $C_e = 5.1164 \times 10^{-2}$.

optical spectra (41,47,54). The local mode is treated as a zero-band phonon line. Although these theories are probably very reasonable for true local modes, their applicability to resonant band modes is questionable since they are based on the adiabatic and Born–Oppenheimer approximations which may not be valid (51). However, they appear to be the best theories currently available and we therefore make use of them in interpreting our data.

Two types of mechanisms contribute to the width of a local mode peak: decay processes and scattering processes. The first of these is simply the decomposition of the local mode into two or more lattice phonons. Since this shortens the lifetime of the local mode it broadens its energy level through the uncertainty principle. For local modes whose frequency is less than the maximum lattice vibration frequency the most probable mode of decay will involve two lattice phonons and is described by the following equation (54,55)

$$\Delta\tilde{E} = \frac{\pi}{2\hbar^2} \sum_{q_1,q_2} \frac{|V_{Q,q_1,q_2}|^2}{\omega_{q_1}\omega_{q_2}} (1+n_1+n_2)\, \delta\, (\omega_1+\omega_2-\Omega) \qquad (140)$$

where V_{Q,q_1,q_2} is the interaction potential for the local mode (wave vector $\underline{Q}$) and phonons with wave vectors $\underline{q_1}$ and $\underline{q_2}$. The delta function expresses the necessary conservation of energy. Substituting into Equation (140) for the phonon occupation numbers, the linewidth variation should have the form

$$\Delta\tilde{E}' = \bar{\beta}_D \{1 + [\exp(\hbar\omega_1/kT) - 1]^{-1} + [\exp(\hbar\omega_2/kT) - 1]^{-1}\} \qquad (141)$$

This predicts a constant value at low temperatures and a linear dependence at high temperatures.

From the phonon dispersion curves for $SrTiO_3$ in Figure 12, these data can be seen that many different combinations of phonons satisfy the conservation of energy requirement for taking part in the decomposition broadening process. However, the only pairs which make a significant contribution to the broadening in the temperature range of interest are those involving phonons of different frequencies (such as the $TO_1(\Gamma_{15})$ and $LO_3(\Gamma_{15})$ phonons with frequencies of 2.8×10^{12} sec^{-1} and 13.7×10^{12} sec^{-1}). Using Equation (140), such phonon pairs predict the temperature dependent broadening shown by the dashed line in Figure 23.

The second type of line broadening mechanism is the inelastic (or "Raman") scattering of phonons by the local mode. In the Debye approximation this is described by the second term in Equation (128) where the coupling constant will reflect local mode-phonon interactions instead of the electron-phonon interaction. The values of $\bar{\alpha}_D$ and T_D needed to fit the data are listed in Table XVIII.

The relative shift in position of the local mode to higher energies with increasing temperature can be attributed to an increase in the self-energy due to the elastic scattering of phonons as described by the first term in Equation (134) of the last section. The best fit to the data shown in Figure 24 was obtained using values for the coupling coefficient and effective Debye temperature listed in Table XVIII.

The thermal expansion of the lattice can also contribute to the temperature dependence of the local mode frequency (56). The change in lattice constant is due as described in the last section for the zero-phonon lines. As discussed there, this mechanism probably does not make a significant contribution to the thermal line shift. The effects of

TABLE XVIII

ADJUSTIBLE PARAMETERS FOR FITS OF LINE WIDTHS AND POSITIONS OF THE LOCAL MODE, AND INTEGRATED RATIO OF THE LOCAL MODE WITH RESPECT TO TOTAL SIDEBANDS IN $SrTiO_3:Cr^{3+}$ (0.02% WEIGHT)

Variables	Parameters	Values
Line Width	T_D	800°K
	$\bar{\alpha}_D$	7.2206×10^{-1} eV
	$\bar{\beta}^*_D$	3.0060×10^{-5} eV
	$\bar{\alpha}^{\omega}_{e}$	3.1664×10^{6} eV
	$\bar{\beta}^{e\omega}_{if}$	3.0060×10^{-5} eV
Line Shift	T_D	115°K
	α'_D	1.9016×10^{-3} eV
	β'^{D}_{if}	0
	α'^{ω}_{e}	5.7158 eV
	$\beta'^{e\omega}_{if}$	0
Integrated Intensity Ratio	θ''_D	650°K
	S	2.946
	C_e	5.1164×10^{-2}

---

*Two phonon energies used for calculations are:

$\Delta E_1 = 1.1579 \times 10^{-2}$ eV,

$\Delta E_2 = 5.6657 \times 10^{-2}$ eV.

the trigonal crystal field distortion found by Slonczewski (48) to contribute the zero-phonon line position might also contribute to the thermal shift of the local mode. This should cause a discontinuity in the slope of the data at 110°K which is not observed. However, due to the large error bars on the data the importance of this mechanism cannot be definitely established.

The integrated intensity of the zero-band phonon line will decrease with increasing temperature due to the increased probability of multiphonon emission (53). This leads to the growth of vibrational sidebands at the expense of the central line emission. For the local mode in the vibronic spectra of $SrTiO_3:Cr^{3+}$ it is not possible to distinguish these broad, weak sidebands due to other vibronic emission in the same spectral region. The decrease in the local mode integrated intensity I_L relative to the total emission intensity I_T can be expressed as (53)

$$I_L/I_T = \exp \{-S[1+4 (\frac{T}{\theta''_D})^2 \int_0^{\theta''_D/T} \frac{xdx}{e^x-1}]\} , \qquad (141)$$

where θ''_D is an effective Debye temperature and S is the Huang-Rhys factor. The solid line in Figure 25 is predicted by Equation (141) with the values of S and θ''_D listed in Table XVIII.

The estimated accuracy of the various adjustable fitting parameters is ±10%.

The effective Debye temperatures represent an upper limit to a Debye type distribution of phonons which take part in the mechanism being considered. Since all lattice modes do not contribute in the same degree to all of the different types of interactions there is no reason to expect the effective Debye temperatures to be the same for all processes or the same as that determined by specific heat measurements. The latter type experiments yield a value of $\theta_D \approx 400^{o}K$ (57). This result must be dominated by contributions from acoustic phonons since optic modes range up to three times this "cut-off" value (6,7). The similar effective Debye temperatures needed to fit the line width and intensity data imply similar phonon distributions active in the contributing physical processes. The value of ~800^{o}K indicates a cut-off frequency for the distribution which falls approximately in a gap in the observed phonon frequency distribution for $SrTiO_3$ (6,7). The highest density of phonon states lies below this region. The much lower effective Debye temperature obtained in analyzing the line shift data implies coupling to only acoustic and the lowest optic phonon modes. This is interesting because of the importance of "soft modes" in the lattice dynamics of strontium titanate.

The most complete temperature dependence investigations have been on the U-center in alkali halides (50,51,53,57). The decrease in the local mode intensity at high temperatures shown in Figure 25 is around an order of magnitude greater than that reported for infrared absorption on these other systems. The Huang-Rhys factors needed to fit the data obtained on U-centers in six different host crystals range from 0.05 to 0.32. The much larger value of $S = 2.9$ needed to fit our data implies a significantly stronger coupling to the lattice phonons for the local mode in $SrTiO_3:Cr^{3+}$ than for the U-centers in alkali halides. This may be due to the fact that the local mode in the former case is probably due only to force constant changes whereas in the latter case a large mass defect is present as well as any possible deviations in force constants. Also, it may be that gap or band modes can couple more strongly to the lattice phonons than true local modes that lie significantly above the normal mode frequency distribution of the crystal. The effective Debye temperatures needed to fit infrared intensity data vary 9°K for KI:Ag^{1+} up to 220°K for KCl:D^{1-} an CaF$_2$:H^{1-} which are less than the specific heat Debye temperatures (53). Thus high frequency phonons appear to contribute more to the intensity decrease of the local mode in SrTiO$_3$:Cr^{3+} than they do in the other systems investigated.

The low temperature residual line width shown in Figure 23 is significantly greater than those measured previously for local modes in infrared spectra and the broadening at higher temperatures is less (53,54,56). The decomposition mechanism dominates at low temperatures and predicts a smaller temperature dependence than the Raman scattering mechanism at high temperatures. This implies that the former mechanism is relatively more important than the latter in contributing to the broadening of the local mode in the vibronic spectrums of SrTiO$_3$:Cr^{3+} as compared to the infrared absorption data obtained previously on impurities in alkali halides and similar systems. This may be because the importance of the scattering mechanism is independent of the frequency of the local mode with respect to the phonon frequency distribution whereas the importance of the decomposition mechanism increases the closer the local mode frequency is to the phonon frequencies. For this case the local mode frequency is within the frequency distribution of lattice vibrations of strontium titanate whereas most of the local modes whose temperature dependence have been investigated in detail previously lie above the phonon cutoff frequency of the host lattice. However, the thermal broadening of the resonant band mode in NaCl:Cu^{1+} is closer to the U-center data than to the SrTiO$_3$:Cr^{3+} data (58). Thus the coupling coefficients for the different processes must be taken into account for each system as well as the relative position of the local mode frequency.

The thermal lineshift is similar in magnitude and direction to several of the previously studied alkali halide systems (53,54,56). However, in some cases such as KCl:H^{1-} the peak shift is in the opposite direction (56). This has been attributed to the effects of thermal expansion. Since the small values of the coupling coefficient and effective Debye temperature needed to fit the data shown in Figure 24 imply much smaller effects from phonon scattering than implied by the line broadening data, it may be that some negative contributions from thermal expansion are present.

Little can be said about the magnitudes of the coupling parameters α and β since their values cannot be theoretically predicted. A wide range of values covering those used here have been found when the same theories are applied to zero-phonon line optical transitions (41,49,60).

Although the comparisons discussed in the preceeding paragraphs are very qualitative, they imply that the same physical processes contribute to the thermal characteristics of both the local mode studied here with vibronic spectroscopy and those studied previously in other systems using infrared spectroscopy. The quantitative differences appear to be consistent with the different characteristics of local modes such as the mass defect, charge defect, and vibration frequency with respect to the phonon frequency distribution of the host crystal. Thus it appears that vibronic spectroscopy is a complimentary technique to infrared absorption in studying the characteristics of local modes. For the case reported here the accuracy of the data is less than that of similar infrared absorption studies but this is due to overlapping of local mode with a nearby vibronic band and is not a limitation of experimental apparatus. Which technique is better depends mainly on the specific system under investigation. Vibronic and infrared absorption transitions are subject to different selection rules. The intensity of a vibronic peak also depends on the strength of the electron-vibration interaction whereas the intensity of an infrared absorption peak depends on the local electric dipole moment. Therefore, in some cases a local mode will be more easily observed in vibronic spectra and in other cases it will be seen easier in infrared spectra.

The virtual phonon scattering contribution to the lineshift of the local mode is similar to that of the zero-phonon lines in that it involves a low Debye temperature and a small value for the coupling parameter. However, Raman scattering of phonons appears to play a more important role in broadening the local mode than it did the R lines.

The data in Figures 23-25 can also be fit using the one-phonon density of states obtained from the vibronic spectrum as shown by the dashed or dotted lines. These fits were obtained using the density of phonon states given in Equation (129) and the parameters in Table XVIII. The predict a fit to the linewidth and lineshift data which is equivalent to the prediction obtained using the Debye approximation. However, no good fit to the intensity quenching data can be obtained using the vibronic effective density of states.

CHAPTER VI

SUMMARY AND CONCLUSIONS

A spectroscopic investigation was conducted on lightly doped strontium titanate with Cr^{3+}. Continuous fluorescence measurements were made both of low frequency and high frequency vibronic bands at numerous temperatures from $8^{o}K$ up to room temperature. By assuming that all the phonon modes were coupled linearly except the local mode which was coupled quadratically, the effective one-phonon side band was computed by an iteration processes.

The effective one-phonon side band was then used to study temperature dependences of the line widths and shifts of the zero-phonon lines (R_1, R_2) and the results compared with those predicted by the Debye approximation and by coupling to only a soft transverse optic phonon mode. Measurements of the widths, positions and the integrated intensities of the local mode were also made. The results of these experiments are summarized and conclusions from those results are discussed. Several suggestions for further work are finally mentioned.

Summary of Results

The various investigations discussed in Chapter IV and V led to the following results:

1. By comparison with infrared absorption data, Raman scattering results, and the dispersion curves of the neutron scattering data the

peaks observed in the low energy vibronic sideband were identified with phonons at various points of the Brillouin zone. Restrictions from vibronic selection rules explain the absence of several peaks which appear in neutron scattering. The sharp peak at about 0.0706 eV can not be associated with any known lattice vibration and is thought to be a local mode.

2. A great deal of structure was observed in the high energy sideband near the R lines. Much of this structure has not been reported previously. By comparison with Raman scattering, infrared absorption, and the dispersion curves of the neutron scattering two peaks at 0.0021 and 0.0055 eV are attributed to the Γ_{25} (R point) soft phonon mode which has been split by the lower symmetry. The peak at 0.0036 eV is the Γ_{15} transverse optic soft mode at the center of the Brillouin zone.

The intensities of the main peaks in this region do not increase continuously with temperature as is usually seen with high energy vibronics. Instead they increase to a maximum at about 40°K and then decrease which can be accounted for by the temperature dependences of the soft mode frequencies.

3. The effective one-phonon side band was computed by an iteration processes. By convolution processes with estimated one-phonon side bands, multiphonon sidebands were generated. Quadratic coupling was included for the interaction of local mode and lattice phonons with the impurity.

4. The measured temperature dependences of the line widths and line positions of the zero-phonon lines were fitted by using the effective one-phonon density of states which was computed from the vibronic spectrum. A fit equivalent to that found using a Debye distribution could be obtained only if the high frequency part of the effective one-

phonon density of states was neglected.

5. The temperature dependence of the decay time of the zero-phonon line was measured at various temperatures from 8°K to room temperature and found to be consistent with the changes of the ratio of the integrated intensity of the zero-phonon line to the total integrated intensity of the side bands and the zero-phonon line.

6. The temperature dependence of the widths, positions, and integrated intensities of the local mode were measured at various temperatures from 8°K up to room temperature. A Debye approximation was used to fit these temperature dependences. Using the vibronic effective density of states gives an equivalent fit to the data on line widths and position but no fit to the intensity quenching data could be obtained.

Conclusions and Implications for Further Work

This investigation demonstrates the usefulness of vibronic spectroscopy in obtaining information on phonon frequency distributions. High energy vibronics were shown to be especially important in observing low frequency soft modes. The use of vibronic spectra in investigating local modes was also demonstrated.

The results obtained in this study suggest several interesting topics which may be the subject of further work:

1. A precise calculation of the selection rules in tetragonal symmetry is needed to successfully explain all the observed vibrational modes.

2. Materials should be investigated which have much lower phase transition temperatures so the soft mode frequencies can be monitored as a function of temperature without being obscured by the broadening of

the zero-phonon lines.

3. A more rigorous lattice dynamics model should be developed to treat the electron-phonon coupling.

REFERENCES

(1) Bron, W. E., Phys. Rev. 185, 1163 (1969); Bron, W. E., Phys. Rev. 140, A2005 (1965); Bron, W. E., and W. R. Heller, Phys. Rev. 136, A1433 (1964); Bron, W. E., and M. Wagner, Phys. Rev. 145, 689 (1966); Wagner, M. and W. E. Bron, Phys. Rev., 139, A223 (1965); Bron, W. E., and M. Wagner, Phys. Rev., 139, A233 (1965) and private communications.

(2) Maradudin, A. A., Solid State Physics, Vol. 18, edited by Seitz, F., and D. Turnbull (Academic, New York, 1966), p. 273.

(3) Lytle, F. W., J. Appl. Phys., 35, 2212 (1964).

(4) Axe, J. D. and G. Shirane, Phys. Today, Sept., 1973, p. 32.

(5) Werlock, J. W. and P. A. Fleury, Phys. Rev. Lett., 19, 1176 (1967); Fleury, P. A., J. F. Scott, and J. M. Worlock, Phys. Rev. Lett. 21, 16 (1968); Fleury, P. A., and J. M. Worlock, Phys. Rev., 174, 613 (1968); Scott, J. F., P. A. Fleury, and J. M. Worlock, Phys. Rev., 177, 1288 (1969).

(6) Cowley, R. A., Phys. Rev. Lett., 9, 159 (1962); Cowley, R. A., Phys. Rev., 134, A981 (1964); Cowley, R. A., W. J. L. Buyers, and G. Dolling, Solid State Comm. 7, 181 (1969); Stirling, W. G., and R. A. Cowley, J. de Physique 33 (supplement) C2-135 (1972); Stirling, W. G., J. Phys. C: Solid State Phys., 5, 2711 (1972).

(7) Shirane, G., and Y. Yamada, Phys. Rev., 177, 858 (1969); Yamada, Y., and G. Shirane, J. Phys. Soc. Japan 26, 396 (1969).

(8) Last, J. T., Phys. Rev., 105, 1740 (1957).

(9) Spitzer, W. G., R. C. Miller, D. A. Kleinman, and L. E. Howarth, Phys. Rev., 126, 1710 (1962).

(10) Barker, A. S., and M. Tinkham, Phys. Rev., 125, 1527 (1962).

(11) Barker, A. S. and J. J. Hopfield, Phys. Rev., 135, A1732 (1964).

(12) Perry, C. H., B. N. Khanna, and G. Rupprecht, Phys. Rev., 135, A408 (1964).

(13) O'Shea, D. C., R. V. Kolluri, and H. Z. Cummins, Solid State Comm., 5, 241 (1967).

(14) Rimai, L. and J. L. Parsons, Solid State Comm., 5, 387 (1967).

(15) Schaufele, R. F. and M. J. Weber, J. Chem. Phys., 46, 1859 (1967).

(16) Perry, C. H., J. H. Fertel, and T. F. McNelly, J. Chem. Phys., 47, 1619 (1967).

(17) Nilsen, W. G. and J. G. Skinner, J. Chem. Phys., 48, 2240 (1968).

(18) Cochran, W., Ad. Phys., 9, 387 (1960).

(19) Anderson, P. A., in Fizika dielektrikev, Skanavi, G. I., Ed. (Akademica Nauk SSSR Fizicheskii Inst. Lebedeva, P. N., Moscow, 1960).

(20) Rimani, L., and G. A. deMar, Phys. Rev., 127, 702 (1962); Müller, K. A., Phys. Rev. Lett., 2, 431 (1959).

(21) Unoki, H., and T. Sakudo, J. Phys. Soc. Japan 23, 546 (1967).

(22) Höchli, U. T., Solid State Comm., 13, 1369 (1973).

(23) Bell, R. O., and G. Rupprecht, Phys. Rev., 129, 90 (1963).

(24) Mitsui, T., and W. B. Westpal, Phys. Rev., 124, 1354 (1961).

(25) Steigmeier, E. F., Phys. Rev., 168, 523 (1968).

(26) Tufte, O. N., and E. L. Stelzer, Phys. Rev., 141, 675 (1966).

(27) Parsons, J. L., and L. Rimai, Solid State Comm., 5, 423 (1967).

(28) Yamamoto, H., S. Makishima, and S. Shionoya, J. Phys. Soc. Japan 23, 1321 (1967); Makishima, S., K. Hasegawa, and S. Shionoya, J. Phys. Chem. Solids 23, 749 (1962).

(29) Weber, M. J. and R. F. Schaufele, J. Chem. Phys., 43, 1702 (1965); Weber, M. J., and R. F. Schaufele, Phys. Rev., 138, A1544 (1965).

(30) Stokowski, S. E., and A. L. Schawlow, Phys. Rev., 178, 457 (1969).

(31) Grabner, L., Phys. Rev., 177, 1315 (1969).

(32) Stokowski, S. E., and A. L. Schawlow, Phys. Rev., 178, 464 (1969).

(33) Di Bartolo, B., Optical Interactions in Solids, (Wiley, New York, 1968).

(34) Merzbacher, E., Quantum Mechanics (Wiley, New York, 1970).

(35) Lax, M. J., Chem. Phys., 20, 1752 (1952).

(36) Mostoller, M., B. N. Ganguly, and R. F. Wood, Phys. Rev., 4, 2015 (1971).

(37) Barker, A. S., Phys. Rev., 145, 391 (1966).

(38) Narayanan, P. S., and K. Vedam, Z. Physik, 163, 158 (1961).

(39) Vredevoe, L. A., Phys. Rev., 147, 541 (1966).

(40) Stokowski, S. E., S. A. Johnson, and P. L. Scott, Phys. Rev., 147, 544 (1966).

(41) McCumber, D. E. and M. D. Sturge, J. Appl. Phys., 34, 1682 (1963).

(42) Imbusch, G. F., W. M. Yen, A. L. Schawlow, D. E. McCumber, and M. D. Sturge, Phys. Rev., 133, A1029 (1964).

(43) Powell, R. C., J. Appl. Phys., 39, 4517 (1968).

(44) Mostoller, M., B. Henderson, W. A. Sibley, and R. F. Wood, Phys. Rev., 4, 2667 (1971).

(45) Lüders, M., and K. F. Renk, Solid State Comm., 7, 575 (1969).

(46) Powell, R. C., B. Di Bartolo, B. Birang, and C. S. Naiman, J. Appl. Phys. 37, 4937 (1966).

(47) Rupprecht, G., and W. H. Winter, Phys. Rev. 155, 1019 (1967).

(48) Slonczewski, J., Phys. Rev., B2, 4646 (1970).

(49) McCumber, D. E., J. Math. Phys., 5, 222 (1964).

(50) Klein, M. V., in Physics of Color Centers, (edited by W. B. Fowler), p. 429, Academic Press, New York (1968).

(51) Genzel, L., in Optical Properties of Solids, (edited by S. Nudelman and S. S. Mirta), p. 453, Plenum Press, New York (1969).

(52) Müller, K. A., in Paramagnetic Resonance (edited by W. Low), Vol. 1, Academic Press, New York (1963).

(53) Silsbee, R. H. and D. B. Fitchen, Rev. Mod. Phys., 36, 432 (1964); Mitra, S. S., and R. S. Singh, Phys. Rev. Lett., 16, 694 (1966); and Takeno, S., and A. J. Seivers, Phys. Rev. Lett., 15, 1020 (1965).

(54) Elliot, R. J., W. Hayes, G. D. Jones, H. F. MacDonald, and C. T. Sennett, Proc. Roy. Soc., (London) A289, 1 (1965).

(55) Ivanov, M. A., M. A. Krivoglaz, D. N. Mirlin, and I. I. Reshina, Soviet Physics-Solid State 8, 150 (1966).

(56) Bliz, H., D. Strauch, and J. Fritz, de Phys., 27, Supp. 2, C2-3, (1966); and Fritz, B., in Localized Excitations in Solids, (edited by R. F. Wallis), p. 480, Plenum Press, New York (1968).

(57) Fritz, B., U. Gross, and D. Bauerle, Phys. Status Solidi, 11, 231 (1965).

(58) Weber, R., and P. Nette, Phys. Letters, 20, 443 (1966).

(59) Hegenbarch, E., Phys. Status Solidi 2, 1544 (1962); Lombardo, G., A. J. Sievers, and R. D. Pohl, Am. Phys. Soc., 10, 44 (1965).

(60) Di Bartolo, B., Ph.D. thesis, MIT (1964); Birang, B., B. Di Bartolo, and R. C. Powell, J. Appl. Phys., 38, 5113 (1967).

APPENDIX

The moment analysis approach can be used to approximate the higher n-phonon emission spectra at T = 0. In order to obtain a desired range of application one can include the needed nth moments in his analysis.

For a function $f(\omega)$ defined by

$$f(\omega) = \int_{-\infty}^{\infty} dt\; e^{i\omega t}\, f(t), \tag{A-1}$$

the area under $f(\omega)$ and the nth moment about the origin are given by

$$F = \int_{-\infty}^{\infty} d\omega\; f(\omega) = 2\pi f(t=0), \tag{A-2}$$

$$\langle\omega^n\rangle = F^{-1} \int_{-\infty}^{\infty} d\omega\; \omega^n f(\omega) = [[f(t)]^{-1} (i\frac{d}{dt})^n f(t)]_{t=0}. \tag{A-3}$$

Moments about the mean are defined by

$$\langle(\Delta\omega)^n\rangle = \langle(\omega - \langle\omega\rangle)^n\rangle, \tag{A-4}$$

and the mean frequency ($\langle\omega\rangle$), and the mean square width are also found as

$$\langle\omega\rangle = [i\frac{d}{dt} \ln f(t)]_{t=0}, \tag{A-5}$$

$$\langle(\Delta\omega)^2\rangle = [[f(t)]^{-1} (i\frac{d}{dt})^2 f(t)]_{t=0}. \tag{A-6}$$

In terms of the dimensionless variable x,

$$x \equiv \frac{\omega - \langle\omega\rangle}{[\langle(\Delta\omega)^2\rangle]^{\frac{1}{2}}} \tag{A-7}$$

an asymtotic expansion for f(ω) is (35)

$$f(\omega) = F[2\pi\langle(\Delta\omega)^2\rangle]^{-\frac{1}{2}}\, e^{-x^2/2}\, \{1 + \gamma_1 f_{11}(x) + \gamma_2 f_{21}(x) + \gamma_1{}^2 f_{22}(x)]$$

$$+ [\gamma_3 f_{31}(x) + \gamma_1\gamma_2 f_{32}(x) + \gamma_1{}^3 f_{33}(x)] + \cdots\cdot\}, \tag{A-8}$$

where γ_1 and γ_2 are the coefficients of skewness and excess, and γ_3 is the coefficient for the fifth moment. γ_i and f_{ij} are given (36) as follows:

$$\gamma_1 = \frac{\langle(\Delta\omega)^3\rangle}{[\langle(\Delta\omega)^2\rangle]^{3/2}}, \tag{A-10}$$

$$\gamma_2 = \frac{\{\langle(\Delta\omega)^4\rangle - 3[\langle(\Delta\omega)^2\rangle]^2\}}{[\langle(\Delta\omega)^2\rangle]^2}, \tag{A-11}$$

$$\gamma_3 = \frac{[\langle(\Delta\omega)^5\rangle - 10\,\langle(\Delta\omega)^3\rangle\langle(\Delta\omega)^2\rangle]}{[\langle(\Delta\omega)^2\rangle]^{5/2}}, \tag{A-12}$$

$$f_{11}(x) = \frac{1}{6}\, x\, (x^2 - 3), \tag{A-13}$$

$$f_{12}(x) = \frac{1}{24}\, (x^4 - 6x^2 + 3), \tag{A-14}$$

$$f_{22}(x) = \frac{1}{72}\, (x^6 - 15x^4 + 45x^2 - 15), \tag{A-15}$$

$$f_{31}(x) = \frac{1}{120}\, x\, (x^4 - 10x^2 + 15), \tag{A-16}$$

$$f_{32}(x) = \frac{1}{144}\, x\, (x^6 - 21x^4 + 105x^2 - 105), \tag{A-17}$$

$$f_{33}(x) = \frac{1}{1296}\, x\, (x^8 - 36x^6 + 378x^4 - 1260x^2 + 945). \qquad \text{(A-18)}$$

Using Equations (A-2) - (A-6), the moments of the individual n-phonon spectra at T = 0 are found as follows:

$$F = 2\pi e^{-S} \frac{S^n}{n!}. \qquad \text{(A-19)}$$

$$<\omega> = N \sum_q \omega_q S_q, \qquad \text{(A-20)}$$

where $N = \frac{n}{S}$,

$$<(\Delta\omega)^2> = N \sum_q \omega_q{}^2 S_q - <\omega>^2/n. \qquad \text{(A-21)}$$

$$\gamma_1[<(\Delta\omega)^2>]^{3/2} = N \sum_q \omega_q{}^3 S_q - \frac{3<(\Delta\omega)^2><\omega>}{n^2} - \frac{<\omega>^3}{n^2}. \qquad \text{(A-22)}$$

$$\gamma_2[<(\Delta\omega)^2>]^2 = N \sum_q \omega_q{}^4 S_q - \frac{\{4<(\Delta\omega)^3<\omega> + 3[<(\Delta\omega)^2>]^2\}}{n}$$

$$- \frac{6<(\Delta\omega)^2><\omega>^2}{n^2} - \frac{<\omega>^4}{n^3}. \qquad \text{(A-23)}$$

$$\gamma_3[<(\Delta\omega)^2>]^{5/2} = N \sum_q \omega_q{}^5 S_q - \frac{5<(\Delta\omega)^4> - 3[<(\Delta\omega)^2>]^2<\omega>}{n} - \frac{10<(\Delta\omega)^3><(\Delta\omega)^2>}{n}$$

$$- \frac{10<(\Delta\omega)^3><\omega>^3 + 15[<(\Delta\omega)^2>]^2<\omega>}{n^2} - \frac{10<(\Delta\omega)^2><\omega>^3}{n^3}$$

$$- \frac{<\omega>^5}{n^4}. \qquad \text{(A-24)}$$

VITA γ

Quiesup Kim

Candidate for the Degree of

Doctor of Philosophy

Thesis: EFFECTS OF ELECTRON-PHONON INTERACTION ON THE FLUORESCENCE SPECTRA OF $SrTiO_3:Cr^{3+}$

Major Field: Physics

Biographical:

Personal Data: Born in Kyounggi-do, Korea, September 25, 1939, the son of Backpoon and Hunsik Kim.

Education: Certificated as a Teacher of Elementary School from Seoul Teachers College, Seoul, Korea, in February, 1958; received Bachelor of Science from Seoul National University, Seoul, Korea, with major in physics in February, 1965, received Master of Science degree in physics from University of Oregon, Eugene, Oregon, in December, 1970; attended Oklahoma State University, Stillwater, Oklahoma 1970-1973; completed requirements for the Doctor of Philosophy degree in May, 1974.

Professional Experience: Teacher in the Chungge Elementary School, Seoul, Korea (1958-1961); been served in the Korean Army (1965-1967); Teacher in Natural Science in the Dongdo Technical High School, Seoul, Korea (1967-1968); Teaching Assistant in the Department of Physics of the University of Oregon, Eugene, Oregon (1968-1970); Teaching Assistant in the Department of Physics of the Oklahoma State University, Stillwater, Oklahoma (1970-1973). Research Assistant in the Department of Physics of the Oklahoma State University, Stillwater, Oklahoma (1974).